ABSTRACT

PRADEEP, SHRAVAN. Towards Designing Flow Mechanics in Dense Suspensions of Smooth and Rough Colloids. (Under the supervision of Dr. Lilian C. Hsiao).

Colloidal suspensions are ubiquitous in everyday life with applications ranging from pharmaceutical formulations to construction materials. Despite this, little is known concerning the design of suspensions from a flow perspective to avoid the problems that arise during their processing stage. Colloidal suspensions used in industrial applications are often complex in nature and are characterized by their size polydispersity, particle surface roughness, complex interactions, and inherent material softness. Furthermore, simulations and experimental studies implemented in academic settings use model particles and tend to ignore the diverse nature of industrial suspensions. In this thesis, we attempt to answer fundamental questions on how one of the complexities listed above, the constitutive particle surface roughness, affects the packing and flow behavior of dense colloidal suspensions. We seek primarily to decouple the effects of particle surface roughness on the bulk suspension behavior by probing their contact microstructure. Throughout the work we use poly(methylmethacrylate) microspheres suspended in refractive index matched solvent squalene.

In the first part of the thesis (Chapter 2), we study the quiescent suspension microstructure of smooth and rough colloids. The mechanical properties of dense suspensions are related to their ability to transmit stress through the fluid. The suspension stress at the quiescent state, evident from the non-zero linear viscoelastic modulus, is directly correlated to the transient “contacts” that are formed due to the Brownian fluctuations in the system. Using 3D confocal microscopy of the equilibrium suspensions at various concentrations, we estimate the nearest neighbors, and extrapolate them to their respective isostatic conditions at the maximum possible packing, also called the jamming point. Apart from average particle diameter, the estimated “contact”

lengthscale included other spatial parameters such as the polymer brush length, size polydispersity, and surface roughness.

The next chapter (Chapter 3) focuses on an issue common in industrial suspensions: shear thickening. Shear thickening occurs when there is an increase in viscosity with increasing applied stress and the phenomena is responsible for issues such as pipe clogs and mixer blade damage during high shear industrial processing of dense colloidal suspensions. Steady shear rheological experiments show that the rate at which suspensions shear thicken is a direct function of the suspension concentration and its respective jamming point. We combine the two parameters into a single parameter called the jamming distance, which is defined as the scaled spatial difference of each suspension with respect to its respective jamming point. Using the contact microstructural analysis of these suspensions using an in-house built confocal rheometer, we determine that the available free volume for suspensions containing particles of different roughness is related to the deficiency from the maximum nearest neighbors at a given stress.

The results from Chapter 2 and 3 have two key takeaways: (a) the microstructures between suspensions of smooth and rough particles, in both quiescent and flow state, are dependent on the constitutive colloidal particle roughness and (b) the rheological properties between suspensions of various colloidal types can be described using the jamming distance. The work in Chapter 4 explores the linear viscoelastic behavior i.e., rheological behavior in near-equilibrium conditions, of dense suspensions containing smooth and rough colloids as a function of their scaled jamming distance. We found that the elastic modulus of rough colloidal suspensions is 103 times more than that of smooth colloidal suspensions at the same concentration. The drastic increase in the modulus is attributed to the reduced dynamics of suspensions containing rough particles due to the additional geometric frustration induced by the restricted rotational degrees of freedom in individual rough particles.

Through results in Chapter 2, 3, and 4, we provide an engineering framework to design colloidal suspensions for desired applications.

Towards designing flow mechanics in dense suspensions of smooth and rough colloids

by
Shravan Pradeep

A dissertation submitted to the Graduate Faculty of
North Carolina State University
in partial fulfillment of the
requirements for the degree of
Doctor of Philosophy

Chemical Engineering

Raleigh, North Carolina
2021

APPROVED BY:

Dr. Lilian C Hsiao
Committee Chair

Dr. Orlin D. Velev

Dr. Jan Genzer

Dr. Joseph B. Tracy

DEDICATION

Dedicated to my parents for their unconditional love, support, and sacrifices throughout my life.

BIOGRAPHY

Shravan Pradeep was born in Thrissur, Kerala. Early in his school years, he found a basic interest in STEM subjects, especially chemistry and computer science. Upon completion of secondary schooling, he decided to pursue an undergraduate degree in Chemical Engineering at Amrita Vishwa Vidyapeetham University. He was a recipient of the Prime Minister’s Scholarship during all four years of his undergraduate studies. Shravan graduated *First Class with Distinction* and secured the 3rd rank in the chemical engineering program.

After graduating, Shravan joined Mangalore Chemicals and Fertilizers Ltd. as a Production Engineering Trainee. He worked in the ammonia and urea plant as shift engineer for a year before deciding to pursue a master's degree. Shravan enrolled in the M.E. Chemical Engineering program in one of the premier institutes in India, Birla Institute of Technology and Science (BITS) Pilani. At BITS, he worked under the supervision of Dr. Sonal Mazumder. His focus was on synthesizing quantum dots for two different applications: (a) bioimaging and (b) organic dye degradation. His master’s thesis focused on how capping agents can be used to tune quantum dots for various applications. After graduating from BITS, Shravan worked as research assistant for a year with Prof. Shalini Gupta, alumnus of the NC State’s Chemical Engineering Ph.D. program, at Indian Institute of Technology (IIT) Delhi. He worked on designing millifluidic devices to capture pathogens using an immunomagnetic capture technique pioneered by the lab. While there, he developed an interest in colloidal and soft materials engineering and decided to pursue doctoral studies in this field.

In 2016, Shravan chose to pursue a Ph.D. in Chemical Engineering at NC State University under the supervision of Dr. Lilian Hsiao. For the past five years he has been working in the Hsiao Lab focusing on colloidal synthesis, suspension rheology, and confocal microscopy experiments.

Apart from research-related activities, Shravan was heavily involved in the intradepartmental activities with his roles in organizing the graduate admission recruitment event, “Future Leaders in Chemical Engineering”, and as the Vice President for the Graduate Student Association. He was also involved in the American Physical Society as their Student Affairs Committee member in the Division of Soft Matter (DSOFT).

After completing his Ph.D., Shravan will be joining the University of Pennsylvania as a Postdoctoral Research Associate. He will work with professors Douglas Jerolmack, Paulo Arratia, and Daniella Bassett on a joint research project probing the yield and fluidization behavior of wet granular materials.

ACKNOWLEDGEMENTS

My graduate school experience can be well described using the opening lines from the Charles Dickens novel “The Tale of Two Cities” - *It was best of the times, it was worse of the times, it was age of wisdom, it was age of foolishness*. Being fully independent for the first time, both in a professional and personal context, I made mistakes and learnt lessons the hard way. But along the way there were important moments when I was proud of my academic achievements. None of this would have been possible without the help and encouragement of colleagues, friends, and family.

First, I was fortunate to work with my advisor, Dr. Lilian Hsiao, who has all the traits you want in a research advisor. She taught me how to write, present, and communicate my research. I have always found Lilian’s way to approach science quite refreshing. She always encouraged us to think about research problems, forge collaborations, and mentor undergraduate students. Above all, Lilian has taught me to how be a good scientist. Even if given an option today, I will not trade anyone else for my research advisor. Thanks for being a wonderful human and looking out for me.

I would also like to thank my doctoral committee members: Jan Genzer, Orlin Velev, and Joe Tracy. Dr. Genzer, I really appreciate your willingness and generosity in finding time to talk whenever I needed to. I thank Dr. Velev for designing one of the best courses for soft matter fundamentals (I learnt a lot in those lectures) and the constant research support during my grad school. Thanks to Dr. Tracy, who provided valuable suggestions during the preliminary exam which helped me better navigate my work. Special thanks to Dr. Saad Khan, who made sure that I got an advisor who fits my research interests, allowed me to participate in the graduate application evaluation process, and over the years looked out to make sure that I never fell out of the GSSP.

Professionally, I have had the opportunity to work with extraordinary people during my doctoral studies. I am grateful to my peers in the Hsiao Soft Matter at Research Triangle (SMART) group. Dr. Alan Jacob, Dr. Yunhu Peng, Daniel Cardenas, and I were the first group of cohorts to join the lab. We had interesting experiences building the lab from scratch and learnt lots of painful lessons along the way. I would like to thank Alan, who generously taught me valuable experimental skills and shared his prior scientific knowledge concerning suspension rheology. I am so happy to see the position you have reached today. I would like to thank Mike Mantini for help with the initial laboratory set up and for being an extra hand in assembling our confocal rheometer. I was also fortunate enough to learn from Dr. Karen Daniels. Her introductory course on granular physics helped me understand the field better and her comments on my manuscripts were extremely helpful.

I next thank Dr. Safa Jamali and Nabi Mohamad, our collaborators at Northeastern University, for helping with the simulations in the colloidal shear thickening project. I learnt a lot working with you guys, especially on the theoretical aspects of shear thickening mechanisms. Special thanks to Chuck Mooney (Analytical Instrumentation Facility) on helping me with training on electron microcopy instruments. I would like to express my acknowledgement to Dr. Jennifer Sun and Dr. Petr Novotny who helped me with the NMR training and sample analysis, respectively. Special thanks to Rakshit Jain, who helped me with VMD simulation data at short notice. Additional thanks to Prof. Corey O'Hern (Yale University) and Dr. Arman Boromand (Facebook Reality Labs) for discussions on jamming literature.

Good undergraduates are hard to come by, but I was lucky I got to work with a few of you, namely, Alex Kramer, Colin Donaldson, Sara Wozniak, Christine Dang, and Alan Wessel. Special thanks to Alan who helped me with the story in the fourth chapter of this dissertation. To Alex, Colin, and Alan: I have seen you develop into individual thinkers over the years, and I am quite proud of where you guys have landed after graduation. Throughout my stay in the department, the staff were of immense help. Specifically, I would like to thank Sandra Bailey for being the nicest administrator I have ever known. Special thanks to Michelle Bunce, Joan O'Sullivan, Paola Cavaliere, Angela Efimenko, and Nancy Dear for making the CBE department environment an approachable workplace. I have included project-specific acknowledgements towards the end of each chapter.

I would also like to thank my amazing roommates, Ryan and Robbie. I could not ask for any other souls to share our "PET" townhouse with. The movie nights, pre-gaming, Halloween costume hunts, and the "Super Smash Bros." evenings were just a few good memorable moments from the past four years. I am going to miss that place when I leave Raleigh. I would also like to thank Camden for making me feel welcome to a new country and culture during my first year. I enjoyed our group homework sessions, driving lessons, lunchtime political discussions, and TV show binges. Special thanks to Leah for being a good listener and assisting with MSE homework. My good friend, Arnab: I cherish our weekend hikes, midnight philosophy chats, and keeping me on tracks. Thanks for being there!

I would like to acknowledge the remaining members in the Hsiao Lab, Chris and Kristine. Chris, thank you for all the wisdom you have imparted even when I was not interested in listening to it. Also, thanks for proofreading the documents I sent you at short notice. To Kristine, thanks for being there as one of my best cheerleaders. I am excited to meet you in Philly in less than six months! I wanted to acknowledge few in others who made my life in Raleigh better - Hen, Wardo, and Alex. You guys made my life in grad school more palatable than I wish to admit. To Zijian and Jiaqi, thanks for all the hotpot dinners. I enjoyed collaborating with you guys on a personal and professional level. To Sneha, thanks for all the desi food you have served me. You are an amazing cook and an amazing friend. To Sahand, Tommy, Danny, Javier (and Ryan): I have cherished our summer trips to Charleston, Portland, and Asheville. I hope we can keep the tradition alive.

Lastly, I would like to thank the most important people in my life: my family. My parents: Baby Pradeep and Pradeep Nair, I have no words to express for the love, support, and countless sacrifices you have given. My brother, Sidhu, and sister-in-law, Hamna: you guys were constant pillars of support throughout my graduate school life.

TABLE OF CONTENTS

LIST OF TABLES

LIST OF FIGURES

CHAPTER 1

Introduction: Experimental synthesis and characterization of rough particles for colloidal and granular rheology[†]

[†]Lilian C. Hsiao and Shravan Pradeep, *Curr. Opin. Colloid Interface Sci*, 43, 94-112 (2019)

Department of Chemical and Biomolecular Engineering, North Carolina State University,
Raleigh, NC – 27695, United States.

This chapter aims to provide necessary background information for understanding the experimental synthesis of smooth and rough particles, characterization of surface roughness, quantification of the pairwise and bulk friction coefficients, and their effect on the rheology of wet particulate flows. Even in the absence of interparticle attraction or cohesion, such types of flows are broadly ubiquitous, spanning enormous length scales ranging from consumer and food products to earth movements. The increasing availability of model frictional particles is useful to advancing new understanding of particulate rheology. Although hard-sphere particles remain the most widely studied system due to their simplicity, their rigid and frictionless nature cannot predict many of the complex flow phenomena in colloidal and granular suspensions. Besides a myriad of interparticle forces, the presence of tangential interparticle friction arising from either hydrodynamics or solid contacts of asperities is now thought to be responsible for commonalities in shear thickening and jamming phenomena at high volume fractions and shear stresses. The overall richness of the suspension mechanics landscape points to the reunification of colloidal and granular physics where one may apply a universal set of physical frameworks to understand the flows of model rough particles across multiple spatiotemporal scales. This can only be accomplished by properly distinguishing between microscopic and bulk friction and by decoupling hydrodynamics and contact contributions within the context of experimental observations.

1.1 Rheological significance of particle roughness

The flow of particulate suspensions plays an important role in a broad variety of geophysical phenomena and engineering applications. These suspensions typically consist of rough or faceted microparticles packed in a continuum fluid in the absence of attractive interactions where the particle type may span colloids, grains, bubbles, and emulsions. Collective mesoscale rearrangements of the particles under applied stresses often cause enormous rheological changes in the bulk material, ranging from the sudden clogging of pipes [1,2], liquefaction and landscape evolution [3-5], to creative applications such as robotic grippers [6] and liquid body armor [7]. Despite the importance of suspension rheology and its investigation since Reynolds and Einstein [8,9], there is still a persistent gap between the behavior of industrially relevant particulate systems and the results obtained from academic model systems. Flows are especially challenging to predict for dense suspensions (volume fraction $\phi > 0.40$) of colloidal (typically with particle diameters $2a \leq 2$ μm) and granular (typically $2a > 2$ μm) particles. This is because textbook treatments for low Reynolds number suspension flows are traditionally developed through three simplifications [10]: (1) particles are perfectly spherical in shape; (2) interparticle collisions are frictionless and overdamped in the case of colloids or inelastic in the case of larger particles; (3) solvent molecules are much smaller than the particle size, such that continuum approximations can be used to model fluid drag between idealized spherical particles.

These assumptions have made theoretical developments from the Navier-Stokes equations tractable and reduced computational demands but have also resulted in a major discrepancy between experimental observations and predictions. A notable example is found in many recent investigations of discontinuous thickening and shear jamming suspensions [11-19], in which rough particles generated jumps in energy dissipation at reduced values of ϕ and shear stresses σ when compared to smooth, spherical particles [12,14,20,21]. The prevailing thought is that contact mechanics become important as lubrication films break down at large σ [22-24], although there is a severe lack of in situ experimental evidence to directly support this statement.

The rheology of particulate suspensions was historically investigated by a combination of fluid mechanics experts and granular physicists [25-27]. Although the two fields diverged in the

1950s, they are now beginning to reconvene due to the need to consider both solid and fluid mechanics in dense suspension flows. The convergence of these two fields is found in a number of reviews on granular physics and suspension mechanics [28-31]. In addition, we recommend a comprehensive review by Morris [32] on the computer simulations of lubricated-to-frictional shear thickening as parallel reading material, which will prove useful as we discuss the experimental results here in light of theoretical findings.

This chapter summarizes recent experimental methods that are used to break new ground in suspension rheology. First, we list a number of academic and industrial particulate materials in which the surface roughness can be controlled and quantified. Second, we describe experimental parameters used to characterize the frictional properties of various particulates based on their surface morphologies. Finally, we describe the effects of surface anisotropy on macroscopic rheological properties as seen in dense suspensions of rough or frictional particles, with an emphasis on how interparticle friction impacts their microstructure and mechanics. The conclusion provides an outlook on the field of dense suspension rheology based on past work, present observations, and future strategies.

1.2 Synthesis of smooth spherical particles

A hard-sphere particle is assumed to be non-deformable and impenetrable and interacts with other particles solely through contact. In experimental systems, particles possess a finite elastic modulus and can become deformed by strong flows [33]. The collisions between particles are inelastic in the case of wet and dry granular materials where inertia dominates because of large particle sizes [34] or are overdamped in the case of colloidal suspensions where viscous dissipation by the solvent is significant [35]. Perfectly smooth hard spheres have represented the ideal model system for many years, allowing researchers to validate simulations and theories of suspension phase behavior and rheology [36-41]. They also provide a benchmarking tool for experimental studies involving rough particles of similar sizes made from the same material. It is worth remembering that many interparticle forces (electrostatics, solvophilicity, van der Waals, depletion, hydrogen bonding, and so forth) are in play during the shear flow of particulate suspensions [42] and that variations in synthesis techniques can produce similar looking particles with various types of pairwise interactions that generate completely different rheological phenomena.

Currently, two common ways to generate such particles are through microfluidics and wet chemistry synthesis. Reviews of microfluidic and lithographic tools used to synthesize particles are found elsewhere [43]. While these methods are capable of producing particles from ~10^1 - 10^2 μm with intricate surface anisotropy and nearly zero size polydispersity, they are challenging to scale up to the sheer number of particles required for bulk rheology measurements. As a point for comparison, it takes ~10^{10} hard-sphere particles ($2a$ = 2 μm) to completely fill a small parallel plate rheometer geometry (diameter = 20 mm, gap height = 500 μm), with a suspension of ϕ = 0.50. Bulk chemical synthesis is therefore a much more viable method for producing the large number of particles used in the investigation of dense suspension rheology. Owing to their well characterized and highly tunable interaction potentials, sterically stabilized silica, polystyrene (PS), and poly(methyl methacrylate) (PMMA) colloids remain three of the most popular systems used in academic studies of suspension rheology. Each system poses unique advantages and disadvantages. All three types of particles can be chemically or physically tagged with conjugated fluorescent dyes for microscopy imaging.

1.2.1 Silica colloidal spheres

Monodisperse silica colloids are synthesized using the Stober process [44,45] in which the precursor, typically tetraethyl orthosilicate, is hydrolyzed in alcohols and grown into colloidal particles through a one-step sol-gel process. An octadecyl aliphatic chain is then grafted to the bare surface of the silica particles through high temperature silanol esterification [46,47]. This method readily produces hard-sphere particles with diameters between 20 nm [48] and 1000 nm [49]. If larger particles are desired, additional layers of silica or other materials such as PS can be grown as shells on seed cores, in a method known as seeded growth polymerization [50]. Depending on the solvent quality, the octadecyl-grafted chains may undergo a lower critical solution temperature crystalline transition that leads to thermoreversible flocculation from a hard-sphere suspension. This tendency to flocculate at reduced temperatures leads to the term "adhesive hard spheres" for octadecyl-grafted silica colloids, which are used in multiple gelation and self-assembly studies. Small-angle neutron scattering is typically used to obtain the Baxter temperature, which quantifies the attraction strength through a square well potential [51-54]. A key benefit of silica colloids is that they do not swell or plasticize in most solvents, which can impact measurements of ϕ, as well as hard-sphere properties. The refractive index mismatch of silica (n = 1.459) with common solvents (n = 1.33 for water, n = 1.429 for tetradecane) is not too large, which does not significantly hinder their imaging resolution in confocal microscopy or introduce significant van der Waals forces. However, since silica colloids have a high density (ρ_p = 1.7-2.0 g/ml) compared with that of most polar and nonpolar solvents (ρ_f = 1 g/ml for water, ρ_f = 0.76 g/ml for tetradecane), the density mismatch poses issues due to sedimentation and detachment from rheometer geometries. This issue is somewhat mitigated if the sedimentation velocities are reduced by decreasing the particle size or increasing the solvent viscosity.

1.2.2 PMMA and PS spheres

Polymeric hard spheres form another class of model systems in studies of suspension rheology, with benefits and drawbacks that are almost completely opposite to those of silica colloids. PS and PMMA colloids are generally prepared by emulsion polymerization [55], in which conjugated polymer brushes such as poly(vinyl pyrrolidone) [56], poly(dimethyl siloxane) [57,58], fluorinated copolymer blends [59], or poly(12-hydroxystearic acid) (PHSA) [60-64] are covalently attached to sterically stabilize a particle. Other stabilizers include electrostatic groups that become charged in specific pH conditions, such as poly(acrylic acid) and aliphatic amines on PS microspheres. The brushes can be grafted through a one-pot synthesis as in free radical polymerization, with or without the addition of reversible addition fragmentation chain transfer agents [65], or they can be grafted after synthesis through atom radical transfer polymerization. Given the suspending fluid, proper choice of the polymer brush is key as a fully solvated brush provides the largest range of steric repulsion compared with a collapsed brush. PHSA grafted PMMA colloids in nonpolar solvents are widely considered to be the model of hard-sphere systems and have been extensively used since the pioneering studies of Pusey and van Megen [36,66,67]. Direct and indirect measures of the hard-sphere properties of PHSA-PMMA colloids are widely available in the literature. The standard PHSA brush length on these PMMA colloids is estimated to bez10 nm, although longer chain lengths of up to 22.4 nm are possible by varying the polycondensation time. The commonly-cited brush length of 10 nm was measured using a surface force apparatus to obtain the interaction energy as a function of the surface separation for two flat mica surfaces grafted with PHSA brushes [68]. Because this study was conducted in dry conditions, the solvated PHSA brush length may be different with varying solvent quality.

The basic principle of emulsion polymerization reactions in the formation of polymer lattices is as follows: a monomer, such as styrene or methyl methacrylate, is dissolved in a solvent mixture in which it is barely soluble. Heat-activated initiators such as potassium persulfate and azobisisobutyronitrile, or ultraviolet light-activated photoinitiators such as hydroxymethylpropiophenone (Darocur), are triggered to release free radicals that initiate and propagate the polymerization reaction. When the oligomers grow to a certain size, they become insoluble in the solvent and phase separate out of the solution as nuclei for further colloidal growth. A thorough review of the mechanisms involved in emulsion polymerization is given by Thickett and Gilbert [55]. The major benefits of using most polymeric colloids are that benign solvents can be used for complete density and refractive index matching and that the stabilizer brushes could potentially be functionalized to introduce stimuli-responsiveness into particles [69]. Some disadvantages include problematic charge screening in nonpolar solvents [70], particle plasticization and swelling in organic solvents [71], and the added complexity that comes with the synthesis of conjugated comb copolymer brushes such as PHSA-g-PMMA.

1.2.3 Other colloidal particles

A few other materials are used in the formation of spherical particles. Poly(N-isopropylacrylamide) (PNIPAM) microgels have highly tunable Young's moduli depending on the concentration of the added cross-linker (10^2 Pa $\leq E \leq 10^4$ Pa) and can be synthesized by one-pot emulsion polymerization. They are used to understand the flow and self-assembly physics of soft, deformable particles above the random closed packing volume fraction of hard spheres ($\phi_{\mathrm{rcp}} = 0.64$) because they expand at temperatures below the lower critical solution temperature [72-74]. The applications of PNIPAM are especially promising in biomedical engineering. Owing to their softness, microgels with binding motifs have been used as platelet-like particles to induce blood clotting rapidly under physiological flow conditions [75], and composite nanostructures have been added to PNIPAM to generate stimuli-responsive hydrogels that are highly stretchable [76]. Another highly versatile colloidal system is trimethoxysilyl propyl methacrylate (TPM), which has been used to create polyhedral clusters [77], light-activated colloidal surfers [78], colloidal alloys [79], and lock-and-key particles [80]. Non-polymeric materials such as fatty acid-coated superparamagnetic iron oxide colloids are prepared by alkali-mediated precipitation and used in magnetic field-driven assembly studies [81-83].

Because of the bottoms-up nature of these synthesis methods, in reality, even so-called smooth particles are never completely smooth at length scales close to that of the homopolymer constituents. Smith et al. [84] found that PHSA-PMMA colloids are slightly porous, with the density of the PMMA cores being slightly lower than that of the homopolymers. Silica and PS colloids are also subject to fluctuations in the particle porosity. This may shift the phase behavior of hard-sphere suspensions, which is a function of the osmotic pressure of the solvent. It could also affect the attraction potential in specific colloidal gel investigations where the interactions are generated by excluded volumes of small depletant molecules.

1.3. Synthesis of rough particles

Rough particles were traditionally considered to be unsuitable as model systems due to their nonuniform surfaces and challenges in simulating such morphologies. They are widely found in industrial formulations due to the use of milling as a common technique to grind up solids, for example in foods, paints, and coatings [85,86]. Fortunately, recent developments in chemical and physical methods to synthesize bulk quantities of rough or bumpy particles have made it possible to investigate the effects of roughness on suspension rheology (Figure 1.1). We provide an overview of industrial and academic methods used to create geometrically symmetric, yet surface anisotropic, particles spanning the colloidal to granular length scales. An in-depth review of the synthesis of porous polymeric particles is given by Gokmen and Du Prez [87] and will not be discussed here. Although there is a nontrivial relationship between roughness and friction [88,89], in general, surface roughness increases the interparticle friction coefficient.

In this section, we discuss various physical and chemical routes to the formation of rough particles in quantities large enough for bulk rheological characterization. The physical methods include milling and grinding processes, self-assembly of smaller particles on larger ones through interparticle forces, in situ templating methods, and external application of mechanical stresses. The chemical methods include the seeded growth of small particles on larger cores, acid or base etching, linker chemistry and charge compensation, and the addition of cross-linkers during emulsion polymerization. The advent of 3D printing has also made it possible to create granular particles with highly complex geometries.

1.3.1 Grinding and milling

A mill applies kinetic energy to solid materials to break them up via friction and attrition. Grains formed by milling are typically very polydisperse in their size distributions (>10%) and may contain sharp and irregular facets. In fact, it is not unusual to obtain polydispersity values ranging from 100% to 300%. A few articles on the effect of breakage mechanisms on particulate sizes are available [90,91], but ultimately, it is an engineering process in which the large number of process parameters makes predictive capabilities difficult. Nevertheless, because a mill is easy to use and can handle large quantities of wet or dry material, milling remains one of the most common manufacturing techniques to grind materials such as organic crystals in pharmaceuticals [92], calcite powders [93], nanocrystalline metals [86], pigments [85], and various other particulates down to the desired size range. Cornstarch, a popular particulate used to study the physics of shear thickening [94,95], is formed by the wet milling of corn kernels and is therefore highly subject to size polydispersity and shape irregularities.

1.3.2 Surface heterocoagulation and seeded growth polymerization

Electrostatic forces are commonly leveraged to decorate large core particles with smaller, oppositely charged particles, forming composite raspberry-like particles with a bumpy exterior. This so-called heterocoagulation mechanism was first used by Ottewill et al. [96] in which negatively charged PS particles are coated with smaller, positively charged poly(butyl methacrylate) (PBMA) particles at reaction temperatures greater than the glass transition temperature of the PBMA. The authors proposed a simple theory to explain this process by considering the interfacial energy of the two polymers. The most important parameter is the ratio of interfacial energies, as found in the Young-Dupre equation, which should be kept at an intermediate value to avoid complete wetting or dewetting. A mass balance can be used to deduce the proper ratio of particle radii and particle numbers for hexagonal close packing of the PS particles on the PBMA cores. Various electrostatic stabilization and energy minimization methods were used successfully by a number of research groups to fabricate a dizzying array of Pickering emulsions and colloidosomes [97], surface-modified PS particles [98,99], and raspberry like silica particles [2,100]. Other types of particle interactions, such as hydrogen bonding and π-π bonding, can also result in the same type of raspberry like morphology [2,100]. Removal of the bumps by chemical etching is also possible if golf ball-like morphologies are desired [101].

A variant of heterocoagulation coupled with seeded growth polymerization can be used to synthesize larger raspberry-like particles, in which a core polymeric particle is coated with a solid shell [102-106]. A secondary coating step is used to grow the shell covalently on top of the composite bumpy particle. This step is thought to provide improved mechanical stability to the asperities during shear such that they do not detach easily [107]. Although the particle morphology obtained with heterocoagulation methods is desirable due to their ease of reproducibility in simulation studies, a major issue is that each chemical synthesis and cleaning step reduces the overall yield of particles.

1.3.3 Confinement templating

Raspberry-like particles with multiple bump functionalities are also obtainable through a microstructural confinement templating method, in which a small number of large particles are dispersed in a concentrated bath of smaller particles. This method was used by Gaulding et al. [108] to deposit functionalized PNIPAM microparticles onto PS spheres, where the surface bumpiness could be precisely tuned. However, this method suffers from two drawbacks, in that the yield of the composite particles is limited and that the unused PNIPAM microparticles would go to waste if not recycled. A similar method was used to confine TPM droplets by co-sedimentation with a dense suspension of PS spheres. The deformed TPM droplets are then polymerized by heat into polyhedral shapes [109]. The yield of particles obtained through templating is likely to be much lower than that obtained through other types of bulk synthesis methods.

1.3.4 In-situ mechanical stresses

Other researchers leveraged methods to generate internal mechanical stresses within particles to create macroporous microstructures. Peterson et al. describe an internal templating method in which the precipitation of low-melting-point salts together with silica nanoparticles using high-temperature aerosol spraying generated various types of macroporous silica colloids [110]. Degassing of PS and PMMA spheres in a polyelectrolyte solvent was also used to create nanometer scale roughness on their surfaces due to changes in the charge density on the polymer surface [111]. A similar gas-producing mechanism was used to create raspberry-like protrusions on silica particles as they passed through a flow-focusing microfluidic channel [112]. The surface morphology is thought to result from the addition of hydrochloric acid and sodium bicarbonate, which participate in the Stober sol-gel process and produce carbon dioxide gas at the silica-water interfacial subphase. Finally, PS dimers and triangles were made by swelling of PS seed particles in the presence of a crosslinker [113]. The concentration gradient of the crosslinker is proposed to mechanically control the directionality of the phase separations during the seeded growth polymerization step. These methods are more likely able to produce the quantities of particles needed for rheological testing, although the maximum roughness achievable may be limited to the nanometer or submicron range.

1.3.5 Crosslinker-aided polymerization

The addition of cross-linking monomers during the early nucleation step of emulsion polymerization can be used to generate surface morphologies that range from slight dimpling to that reminiscent of crumpled paper and golf balls [114]. By increasing the concentration of the crosslinker (ethylene glycol methacrylate) up to 2 wt% of the monomer, our group has fabricated sterically stabilized PHSA-PMMA colloids that have root-mean squared (RMS) roughness values up to 20% of the mean particle radius. Increasing the cross-linker concentration further tends to result in gelation of the entire polymer network, causing a failed synthesis. This wet chemistry method is likely to be applicable for any polymeric materials, such as PS and PNIPAM particles, that are formed by one-pot free radical polymerization reactions. The size and polydispersity of the particles can be tuned somewhat independently of the roughness, although care should be taken such that the elastic modulus of the particles does not increase significantly due to the addition of the cross-linker [115]. The thermodynamic mechanism for the formation of the rough features is currently unknown, primarily due to the innate complexity of emulsion polymerization. We speculate that changes to the oligomer solubility and nuclei shape during microphase separation could be the possible reasons for the formation of rough particles. One of the biggest benefits of this method is that the entire particle is made out of the same material, which simplifies the linking of particle interactions and elasticity to bulk suspension mechanics.

1.3.6 Other wet chemistries

If metallic oxide particles with high surface areas are desired, one-pot and template-free hydrothermal synthesis can be used to prepare copper oxide colloids coated with a layer of cerium oxide. The particle morphology resembles the type created by internal mechanical stresses, and the available surface area for catalysis can be dramatically increased by up to five times by this technique [116]. Hydrolytic polycondensation of poly(methyl silsesquioxane) with inorganic calcium carbonate particles produced composite and roughened colloids with increased hydrophobicity [117]. Photoresponsive raspberry-like colloids were synthesized by covalently attaching iron oxide nanoparticles to silica cores using cucurbituril and azobenzene linkers, which generated reversible changes in particle morphology from rough to smooth upon illumination with ultraviolet light [118]. The authors show that the particle shape can be controlled to switch between shear thinning and shear thickening behavior. These examples illustrate the large variety of wet chemistries that can be used to tailor particle shapes in an equally large variety of particulate materials.

1.3.7 Etching and 3D printing

Chemical etching is a simple method to generate rough surfaces on almost all types of material, whether they are inorganic or organic in nature. By immersing particles in a strong acid or base for a sufficiently long period of time, the solvent will etch away parts of the surface, leaving behind a slightly roughened exterior. Silica and soda-lime glass beads can be etched using concentrated sodium hydroxide and salt derivatives of hydrofluoric acid [119,120]. The RMS roughness can be tuned by controlling the immersion time of the particles [119], although the roughness achievable may be limited to the nanometer range. On the other hand, it is possible for metallic particles with high purity to become smoother after etching.

Finally, 3D printing has emerged as a powerful way to fabricate reusable granular building blocks with highly complex geometries. Engineering software programs such as AutoCAD are typically used to design the particle shape. Many types of 3D shapes, such as polyhedral and stars, can be generated with polymer resins that have different elastic moduli values [121,122]. Acrylic, nylon, ceramics, and hydrogel particles can all be printed this way. The particle size and shape details are limited by the resolution of current 3D printers (~100 μm). A disadvantage with 3D printing is that particles with very thin, interlocking features may break easily during packing or shear due to the low fracture strength of commercial resins.

1.4 Quantifying roughness and friction

The relationships between surface roughness, interparticle friction, and macroscopic suspension mechanics are nonlinear. In the field of tribology, it is understood that surface roughness can completely change the frictional dissipation between two surfaces in near contact. The friction between two surfaces is dictated by the contact area, material elasticity, shearing velocities, and the presence of lubricant fluid between the surfaces [91,135]. Friction may arise from either solid-solid contact or from hydrodynamic drag of the lubricant at higher sliding speeds. The generic friction coefficient, μ, is an adjustable parameter used in many particulate simulations and theories. Because of its importance, a significant amount of effort has been dedicated to measuring μ for various types of particles. No matter how smooth a particle might appear, a non-zero static friction coefficient is always present in experimental observations [32]. Here, we review the methods used to obtain surface roughness parameters, as well as the interparticle friction coefficient (μ_p) and bulk stress ratio (μ_b) in particulate systems. Table 1.1 is a list of μ_p measured using different methods for various types of particulate materials in the literature, although the list is by no means exhaustive. Roughness parameters and particle sizes are provided where available. This table is meant to provide a general reference to the values of μ, which can differ greatly between static and sliding conditions and when additives are present in wet systems.

Table 1.1 | List of particulate materials with various roughness and friction coefficients.

Material	**Method**	**Ref.**	$2a_{eff}$	μ_p	R_q
Acrylic	Angle of repose	[123]	0.3 cm	0.88	0.7±0.3 µm
	Angle of repose	[123]	0.3 cm	0.96	2.6±0.1 µm
Alumina (hydrated)	Lateral force	[124]	6 and 60 µm	0.03-0.07	189 nm

Table 1.1 (continued).

Aluminium	Angle of repose	[123]	0.3 cm	0.62	0.32±0.14 μm
Cellulose	Lateral force	[125]	16 μm	0.22-0.64	13 nm
	Lateral force	[126]	25 μm	0.35	-
Cornstarch	Lateral force	[127]	8 μm	0.02	14 nm
Glass	Lateral force	[15]	9.78 μm	0.9	12.4 nm
	Lateral force	[15]	9.78 μm	0.02	12.4 nm
	Lateral force	[124]	6 and 35 μm	0.18-0.60	12-19 nm
	Sliding	[128]	70-110 μm	0.25-0.65	-
	Angle of repose	[119]	140-240 μm	0.42-0.52	-
	Angle of repose	[129]	3.5 mm	0.20	-
	Angle of repose	[130]	0.5-10 mm	0-1	-
	Sliding	[131]	6 mm	0.13	-
Limestone	Lateral force	[124]	4 μm	0.67	102 nm
Ottawa sand	Cyclic shear	[132]	0.35 mm	0.40	-
Pea gravel	Cyclic shear	[132]	9 mm	0.42	-
PMMA	Simulations	[12]	1.6-2.3 μm	0	20 nm
	AFM	[12]	1.9-2.8 μm	0.30-1.00	50-110 nm
Polystyrene	Angle of repose	[133]	520 nm	0-0.12	-
PTFE	Angle of repose	[123]	0.3 cm	0.54	1.1±0.6 μm
PVC	Lateral force	[127]	1 μm	0.45	2.2 nm
Salmeterol	Angle of repose	[134]	15-36 μm	0.25-0.87	-

Table 1.1 (continued).

Silica	Lateral force	[14]	550-700 nm	0.13	0.53
	Lateral force	[135]	3.4-4.0 µm	0.34-1.04	-
	Lateral force	[136]	5 µm	0.08	-
	Lateral force	[136]	5 µm	0.39	-
	Lateral force	[14]	678 nm	0.03	-
Steel	Angle of repose	[123]	0.3 cm	0.66	0.10±0.02 µm
Titanium	Lateral force	[124]	0.2 µm	0.04-1.50	131-147 nm
Zeolite	Lateral force	[124]	2 µm	0.69	148 nm

1.4.1 Atomic force microscopy and roughness parameters

Atomic force microscopy (AFM) is the leading experimental technique to measure surface roughness at nanometer resolutions. It involves the use of a cantilever and tip with known spring constants to directly probe the topography of a surface in wet or dry conditions. As an extension to the surface force apparatus [68,137], AFM can also be used to obtain the pairwise interactions of surfaces and particles through approach-retraction measurements [138,139]. In this section, we focus on the use of AFM for topographical characterization of surface roughness. Contact mode involves moving the AFM tip up and down as the instrument scans the surface but is typically avoided because the presence of liquids and adhesive interactions between the tip and the surface may erroneously influence topography measurements. A more convenient way to avoid the pitfalls encountered in contact mode is to use tapping mode, which involves oscillating the tip up and down at its resonance frequency using piezoelectric elements in the cantilever holder. To obtain 3D surface topography measurements for particles, the particles must be fixed such that the AFM tip does not move them around during imaging. This is accomplished by partially embedding particles in special epoxies that soften when heated [2] or by spin coating dilute suspensions onto a layer of polymer media adhered to a flat substrate [12]. The surface topography measurements are limited to a relatively small field of view at the top-most part of a particle because imaging artifacts arise from dragging the AFM tip close to the vertical sides of micron-sized or larger particles. Ensemble averaging of the topography across multiple particles is required to generate enough statistics for quantification, especially in the case of highly anisotropic particles. In addition to AFM, other optical methods such as white light scanning interferometry [119] are reported to generate 3D topography data of particles. Confocal laser scanning microscopy is also a possible method, but the difference in resolution in the horizontal and vertical planes should be accounted for.

Before roughness parameters can be extracted, the curved surface profiles of spherical particles must be flattened and compared to a reference surface. This is best done by first fitting an ideal sphere to the 3D topography data, centering the sphere location based on available height information and minimizing the deviation between the two surfaces (Figure 2) [140]. This procedure effectively flattens the curved surface for further analysis. The diameter of the fitted sphere, $2a_{eff}$, should be close to the values obtained from independent measurements of the particle size, such as from scanning electron microscopy. Experimental measures of the roughness can then be obtained through the discretized form of the two-dimensional surface roughness autocorrelation function [141-144]:

$$R_{x,y} \approx \frac{1}{N_x N_y} \sum_{j=-L_y}^{L_y} \sum_{i=-L_x}^{L_x} z(x_i, y_j) z(x_i + \Delta x, y_j + \Delta y) \tag{1.1}$$

where N_x and N_y are the number of AFM data points in the x and y directions, L_x and L_y are the lengths of the x and y directions, Δx and Δy are the pixel sizes, and $z(x_i, y_i)$ is the deviatory surface height at a position (x_i, y_i). It is also possible to compute a 1D form of the function in each direction and simply average them if $N_x = N_y$. From this function, a variety of surface statistical parameters such as the spatial distribution of heights, the mean surface gradient, and the RMS roughness can be obtained. All these parameters are known to affect μ_p, with the RMS roughness $R_q = (R^2)^{1/2}$ being a popular parameter used in the engineering literature [145]. To account for different particle sizes, the value of R_q can be normalized by the particle radius. We emphasize that even nominally smooth particles will have some level of roughness at the nanoscale. For example, R_q was found to be 0.01% for smooth silica colloids [21] and 2.6% for smooth PMMA colloids [12].

1.4.2 Lateral force microscopy

Lateral force microscopy (LFM) is a specialized operating mode of AFM, in which the AFM tip is dragged horizontally across a substrate at a fixed normal force (F_N) and at finite sliding speeds [15,126,135,136,146,147]. The horizontal deflection of the cantilever is used to generate the frictional shear force (F_S) according to Hooke's law. The attachment of a colloidal particle onto the AFM tip is termed colloidal probe microscopy. Many researchers have used LFM with colloidal particles to either measure the value of μ_p for a particle sliding on a surface (which may or may not be coated with particles) or to obtain μ_p for two nonrotational particles. Again, we emphasize that even though LFM provides a measure of the frictional dissipation between two particles, it is not representative of the multibody and multiscale physics found in flowing particulate suspensions.

1.4.3 Angle of repose

Consider building a sand pile on a beach: continue to pour dry sand in one spot and a pile of sand with a constant angle of repose, θ, forms. Adding water to the interstitial spaces reduces θ, whereas the use of coarser grains might increase θ. The angle of repose for a particulate material is defined as the steepest angle to which the granular pile can be built without failure. Two types of experimental setups are used to obtain the angle of repose: The first involves a quasi-2D rotating drum, which spins at a fixed speed and provides the dynamic angle of repose for a particulate material [31,148,149], and the second involves a funnel setup where grains are continuously built into a pile [123,133,134]. The stress ratio can be estimated from the angle of repose through Coulomb's criterion, $\mu_b = F_S / F_N = \tan\theta$, for a solid block sliding down an inclined plane. This ratio is commonly understood as the macroscopic friction coefficient of a material [130]. More sophisticated theoretical treatments of the angle of repose involve using a granular temperature to explain the local rearrangement events of grains [150,151]. This so-called shear transformation zone theory uses statistical mechanics principles [152], reminiscent of the type found in soft glassy rheology [153,154], and was able to explain experimental measurements and computational simulations of specific granular flows down an inclined plane [155,156].

1.4.4 Rheometry and cyclic shear cells

A rotational rheometer is a standard experimental tool used to quantify the relationship between the bulk deformation and bulk stresses of particulate suspensions. When the normal force is fixed and the shear force is measured, a measure of the bulk friction coefficient μ_b can be obtained with various sliding speeds and lubricating solvents. The constant-volume cyclic shear cells used in granular and soil mechanics testing are simply a larger version of the rheometer, capable of plane shearing a packed bed of grains that have diameters on the order of millimeters [4,131,132,157]. These instruments belong to a general class of rheometry techniques that provide bulk material properties that are useful in modeling industrial and geophysical rheological phenomena. Simple shear and oscillatory shear are two operating modes that are widely used in the understanding of suspension rheology. They simulate the type of flows encountered in realistic scenarios and provide useful dynamical information about the bulk material through macroscopic parameters such as the yield stress, shear strength, viscoelastic moduli, and relaxation spectra. Most instruments are either strain rate-controlled or shear stress-controlled, with the cone-and-plate, parallel plate, and annular Couette cells being some of the most common geometries. Recently, Boyer et al. [158] designed a specialized porous annular cell to maintain a constant particle pressure P^p for dense granular suspensions.

1.4.5 In-situ force visualization

The methods described in previous sections provide measures of μ_b and μ_p, but these two parameters may not be representative of the multibody interparticle friction coefficient when a dense suspension is undergoing deformation. Currently, the best-known method to directly visualize grain-scale forces *in situ* is through the use of photoelastic disks made out of commercially available birefringent polymers. A detailed review of photoelastic force measurements in granular packings is provided by Daniels et al. [159]. Briefly, this technique was pioneered by the Behringer group to display contact force networks created by dense packing of 2D disks in a biaxial shear cell [160,161]. Noncircular shapes are also possible. When each photoelastic disk is subjected to external normal stresses from its neighbors, local regions of the material rotates the polarization of light in accordance with the stress–optic coefficient of the polymer. This change in the polarization angle is observable as bright and dark fringe patterns when viewed with a circular polarizer. Photoelastic force measurements were used to characterize both the spatial and temporal distributions of the microscopic force network for various 2D granular packings under linear and nonlinear impact [162]. The photoelastic quantification of force chains in 3D packings has yet not been accomplished due to challenges in analyzing the polarization angle and in fully solving the photoelasticity problem for 3D structures.

1.5 Rheological phenomena

A reason for the recent surge of interest in synthesizing and characterizing rough particles is the attribution of shear thickening and jamming to interparticle friction. These flow scenarios are associated with large increases in the dissipative energy of a dense suspension under applied shear stresses [163-165]. In dense suspensions of colloidal and non-Brownian hard spheres, when ϕ and σ are both sufficiently large, there is a gradual transition from Newtonian flow to mild continuous shear thickening or to discontinuous shear thickening (DST) where s jumps discontinuously as a function of the shear rate $\dot{\gamma}$ [166-168]. Both experiments and simulations found that the suspension viscosity for hard spheres diverges as $\eta_s = (\phi - \phi_{\max})^{-\alpha}$ where $\phi_{\max} \approx$ 0.58-0.60 and $\alpha \approx$ 2.2-2.6 for colloidal glasses [169-171] and $\phi_{\max} \approx$ 0.59-0.64 and $\alpha \approx$ 2.0 for athermal suspensions [158,172]. Other particle shapes such as fibrous rods and ellipsoids with high aspect ratios are known to decrease the value of fmax even further [173,174].

Colloidal suspensions behave in an overdamped fashion due to viscous dissipation from the solvent while inertia becomes important for granular flows involving very large particles. A few dimensionless numbers are useful in conceptualizing the relative importance of inertial and viscous forces, with subtle differences between each number. The Stokes number

$St = \rho_p a_{eff}{}^2 \dot{\gamma} / \eta_f$ provides a measure of the inertial and viscous forces experienced by a particle while the Reynolds number $\mathrm{Re}_p = \rho_f a_{eff}{}^2 \dot{\gamma} / \eta_f$ describes the competing forces experienced by the fluid around the particle. These two dimensionless numbers are different from the conventional Reynolds number for a continuum fluid in a parallel-plate rheometer geometry, $\mathrm{Re}_f = \rho_f (2\pi RH) \dot{\gamma} / \eta_f$, where H is the gap height and R is the radius of the geometry. It is well known in the fluid mechanics community that pure fluids and dilute suspensions undergo inertial or turbulent flows when $\mathrm{Re}_f > 1$. These types of inertial flows exhibit a shear stress to shear rate scaling of $\sigma \sim \dot{\gamma}^{3/2}$ and should be differentiated from the Bagnoldian scaling ($\sigma \sim \dot{\gamma}^2$) in dense granular flows, which is observed even at low Re_p values depending on ϕ [175].

1.5.1 Onset of shear thickening and dilatancy

At extremely large values of ϕ and σ, both colloidal and granular suspensions may experience an expansion in volume and dilate against its confining boundaries [175] or even stop flowing altogether [176,177]. Although dilatancy is thought to be related to shear thickening [178,179], recent data on silica and PMMA colloids show that their onset stresses and volume fractions do not always coincide [180]. Further investigation is necessary to comprehensively probe the role of surface roughness on the onset conditions of dilatancy and shear thickening.

The critical stress of thickening, σ^*, scales inversely as the particle radius squared ($\sigma^* a_{eff}{}^2 \sim 1$) for spherical PHSA-PMMA and silica colloids with or without electrostatic repulsion [181,182]. This scaling can be interpreted as a force balance between two particles at “contact” where the hydrodynamic force acting on a particle pair is equivalent to the derivative of the interparticle potential that prevents them from overlapping. If other types of interparticle forces are present, then the onset stress may scale in a different way or even become obscured by a yield stress in the case of attractive interactions. Stokesian Dynamics (SD) [183] and dissipative particle dynamics simulations, in tandem with rheo-visualization experiments [184-186], showed that short-range lubrication forces are important in generating compact microstructures in flows [187]. Brownian motion introduces a time scale into the onset of thickening [188,189]. The conundrum was that squeeze flow for perfectly spherical particles could not explain the large viscosity increases in DST or the observations that dense suspensions generate a positive macroscopic normal force due to dilatancy [190]. We note that experimentalists should exercise care in reading out normal stress differences directly from a standard rheometer because the instrument assumes that surface tension effects are negligible on the boundaries of the fluid-air interface. Dilation cause particles to protrude at the interface [191], leading to a large decrease in the first normal stress difference, N_1.

The axial force, F_z, exerted on the rheometer geometry by the suspension is a more appropriate way of understanding dilation going forward. If surface tension terms are negligible then,

$$F_z = -\pi R^2 \left[\left(\frac{\sigma_{\theta\theta} - \sigma_{\phi\phi}}{2} \right) + \sigma_{rr} + P_{atm} \right] = -\frac{1}{2}\pi R^2 N_1 \qquad (1.2)$$

where R is the radius of the geometry; $\sigma_{\theta\theta}$, $\sigma_{\phi\phi}$, and σ_{rr} are the normal stresses of the fluid in the θ, ϕ, and r directions; and P_{atm} is the atmospheric pressure that holds the fluid boundaries in place. For the conventional N_1 relation in Eq.(1.1) to apply, the instrument software assumes that σ_{rr} is balanced by $P_{atm} - P_{surf}$, where $P_{surf} \sim \gamma/R_{curv}$ is negligible due to the large radius of curvature (R_{curv}) of the interface. Here, γ is the surface tension of the liquid. When particles protrude from the interface due to dilatancy, then $P_{surf} \sim \gamma/a_{eff}$ generates a significant contribution to σ_{rr}, making it difficult to define the first normal stress difference N_1 as read out by the rheometer. Particle imaging experiments have shown that it takes a finite amount of time for the particles to protrude from the surface of the suspension and to generate a large negative N_1 value. These considerations suggest that it is more appropriate to use F_z instead of N_1 to characterize a dilating suspension and that confinement from boundaries plays an important role in measuring dilation.

1.5.2 Hydrodynamics and granular friction

The term "hydrodynamics" in suspension rheology refers to the stresses borne by the fluid phase in which particles are suspended, which are strong functions of the particle concentration ϕ. Einstein famously derived the relation between the viscosity of a dilute suspension and its volume fraction, $\frac{\eta}{\eta_s} = 1 + 2.5\phi$, by considering the mechanical work done on a continuum fluid by the presence of a rigid sphere. This was accomplished through a surface integral for the expanding spheres. The Stokes-Einstein-Sutherland relations for dilute suspensions (translational diffusivity $D_T = k_B T / 6\pi\eta a$, rotational diffusivity $D_R = k_B T / 8\pi\eta a$) were obtained by considering the Stokes drag around a sphere, the osmotic pressure exerted by a particle, and Fick's first law of diffusion. As the volume fraction increases beyond $\phi > 0.05$, the Einstein relation for viscosity no longer holds because multibody interactions cause the fluid stresses to become a function of the sheared microstructure of the particles [192]. After Einstein, it took nearly 70 years before an analytical form of the relative viscosity that includes higher order terms of ϕ^2 was obtained [193], but the Batchelor-Green relation is still unable to predict the viscosity when $\phi > 0.20$. In fact, most experimental studies of smooth hard-sphere suspensions still rely on empirical correlations and benchmarking against previous studies to verify the validity of their measured suspension viscosities at $\phi \geq 0.50$.

SD simulations developed by Brady and Bossis in the late 1980s created a major inroad into suspension rheology by incorporating multibody short-range and long-range lubrication hydrodynamic forces (represented by the grand resistance tensors) to predict the structure and dynamics of a sheared suspension up to $\phi \approx 0.50$ [194,195]. Lubrication hydrodynamics lead to negative N_1 values in dense suspensions of hard spheres (up to $\phi \approx 0.60$) due to anisotropies in the shear-induced microstructure and the formation of hydroclusters [196]. Although surface roughness was explored using lubrication hydrodynamics models in the early 2000s, at that time, simulation results did not match that of experiments in terms of the large increase in suspension stresses that characterize DST and dilatancy [197-200]. Promisingly, the inclusion of surface roughness or adaptation of a roughness-corrected tangential lubrication force below a cutoff distance in SD simulations appears to generate results that agree well with experimental observations even at high ϕ.

An alternative mechanism is proposed by researchers working in granular physics, who have considered the concept that solid friction is responsible for the flow behavior of dry granular matter [201]. Specifically, it is known that dense granular flows exhibit an intermediate fluid regime where particles interact by inelastic collisions and contact friction [202-204], which are quantified by the restitution coefficient and the friction coefficient. They also undergo flow-arrest (jamming) transitions, as illustrated in a series of state diagrams by Liu and Nagel [205] and O'Hern et al. [206]. Although this problem may appear simple at a glance, difficulties arise from the lack of constitutive relations for granular flows. The reasons for these challenges are twofold: (1) the continuum approximation for small solvent molecules, as in complex fluids and colloidal suspensions, cannot be applied to discretized granular particles [207] and (2) there must be a macroscopic friction coefficient imposed on the suspension [31]. Because there are no internal stress scales in perfectly frictionless and rigid spheres, the lack of a macroscopic frictional criterion means that they would not be able to form any solid-like structures such as a granular pile.

The introduction of this macroscopic friction coefficient (μ_b) is the origin of the growing interest in bridging suspension and granular mechanics. Cates et al. [208] first proposed shearing concentrated colloids as a specific example of inducing fragility in soft matter, in which force chains are formed to support compressive load without plastic rearrangement. This concept was further developed to explain S-shaped flow curves [209] and to derive local constitutive relations, in which granular ideas such as jamming and friction were introduced into shear thickening [210].When incorporated into simulations, a frictional criterion generally does well in predicting the long-range velocity correlations and force networks displayed by granular flows [211,212]. In particular, the relationship between the bulk stress ratio and the viscous number above the material yield stress, or so-called μ(I) rheology, is used to generate predictive models for the nonlocal rheology of granular flows [213-215].

Currently, most researchers agree that both hydrodynamic and contact forces are important in sheared suspensions, with a joint effort directed at decoupling the fluid and solid contact contributions to the overall dissipation [216-218].

1.5.3 Bridging rheology at macroscale

Recent efforts at bridging colloidal suspensions with granular matter have suggested bulk μ(I) rheology as a possible unifying framework. At the macroscopic level, dimensional analysis on frictional granular flows generates the Bagnoldian relations in which the shear stress scales as $\sigma = \rho_p a^2 f_1(\phi)\dot{\gamma}^2$ and the normal stress scales as $\sigma = \rho_p a^2 f_2(\phi)\dot{\gamma}^2$, where f_1 and f_2 are functions of packing density [219]. The stresses for a flowing colloidal suspension without frictional interactions scale as $\sigma \sim P \sim \eta_s \dot{\gamma}$, with thermal motion generating a dynamic yield stress at low $\dot{\gamma}$. Boyer et al. used a constant pressure shear cell to develop a general constitutive framework for millimeter-sized PS and PMMA granules, in which the suspension viscosity (η_s) and μ_b are measured as a function of the viscous number $I_v = \eta_s \dot{\gamma} / P$, where $\dot{\gamma}$ is the applied shear rate and η_s is the solvent viscosity (Figure 12a). The measured rheology of the granular suspensions obeys the frictional framework of granular matter and the viscous framework of colloidal suspensions. Confined pressure Brownian Dynamics simulations of hard-sphere colloidal suspensions by Wang and Brady [220] showed a similar μ(I) scaling, although the yield point is slightly lower than experimental measurements (Figure 1.2b). Because hydrodynamic and frictional interactions were not imposed in the simulations, the authors showed that excluded volume alone in colloidal suspensions can generate similar types of bulk rheological behavior as the kind seen with frictional granular flows.

1.5.4 Bridging rheology at the microscale

The pairwise friction coefficient μ_p offers a more intuitive way of thinking about frictional effects on dense suspension rheology. Simulation studies explicitly impose Coulomb's friction criterion for the particle tangential and normal contact forces, by applying the relation $F_{S,p} = \mu_p F_{N,p}$ when neighboring particles make contact or overlap with one another [221]. This contact load model was developed as an attempt to overcome the breakdown in continuum approximations as particles approach within nanometers of one another in strongly sheared flows. Its success in capturing the viscosity increases in DST, and a positive first normal stress difference representative of dilatancy, led to a subsequent influx of granular concepts into suspension rheology, including theoretical predictions of S-shaped flow curves based on a phenomenological relation between the jamming volume fraction ϕ_J and the fraction of broken lubrication films f [23]: $\phi_J(f) = \phi_\mu f + \phi_{RCP}(1-f)$. Constitutive models are beginning to become available [253]. The jamming volume fraction refers to the value of ϕ at which η_r diverges, in which $\phi = \phi_{rcp} = 0.64$ is related to the isostatic criterion of frictionless hard spheres ($\mu_p \approx 0$) and $\phi_\mu = 0.54$ is the random close packing of frictional particles ($\mu_p \approx 1$) [222-225]. The lubrication-to-friction relation spawned a flurry of other investigations, including a shear reversal study in which the authors claimed to have measured contact force contributions to the suspension viscosity in continuous shear thickening [217] in contradiction with previous studies. The idea is that contact forces go to zero immediately upon shear reversal, whereas hydrodynamic forces stay constant. While the experimental data were in good agreement with contact load model simulations, it is important not to overanalyze raw rheometric data below an initial time of 0.5 s even with modern stress-controlled rheometers. Our laboratory calibration data show that inertia of the motor combined with the suspension may cause artifacts in stress measurements across all shear rates tested. To truly validate the presence of solid contact friction in dense suspensions, in situ 3D measurements of particle-level forces, similar to that of the photoelastic disks are necessary.

Unfortunately, there is currently no experimental way to measure the value of μ_p as a 3D suspension is undergoing flow. Furthermore, the friction between two surfaces should not be quantified using an ensemble-averaged value. This is because of evidence that shows the tendency for DST and dense granular flows to be locally and dynamically inhomogeneous, punctuated by shear bands with jammed and shear thinning regions that change over time [226,227]. Because the friction coefficient varies nonlinearly as a function of the roughness, sliding speed, and separation gap between two surfaces [228-230], simply substituting a singular value of μ_p into models will not capture the relevant micromechanics. An excellent simulation study by Fernandez et al.

correctly accounted for the Stribeck behavior between two particles, which captured the transition from Newtonian to shear thickening flows. Experimental measurements of polymer-adsorbed quartz microparticles supported the simulation data, although nanotribology friction tests were performed using flat surfaces in this study [15].

Recently, rheological studies quantified the shear thickening and dilatant properties of colloids with different roughness parameters or frictional interactions [231-233] (Figure 4). Although the Isa group used laterial force microscopy to obtain μ_p for bumpy silica colloids and our group used the match between simulations and experimental rheology to back-calculate μ_p, the take-home message from both studies are similar: frictional dissipation is enhanced by the presence of submicron-sized surface roughness on particles, possibly due to particle interlocking mechanisms that slow down the stress relaxation of the hydroclusters or force networks that persist in shear thickening [234-236].

1.6 Conclusion

The richness of the suspension mechanics landscape points to the reunification of colloidal and granular physics in the near future [237]. In this version of the future, we envision that it would be acceptable to apply a universal set of frictional and hydrodynamic frameworks to understand the flows of colloids and soils across multiple spatiotemporal scales and in which rough particles will be considered model systems for frictional flows. However, care must be taken to ensure that proposed models are truly representative of the physics of flowing suspensions in different regimes. A look at introductory tribology textbooks immediately illustrates that a friction coefficient may arise from either hydrodynamic or contact origins and that the friction between two sliding surfaces depends nontrivially on lubricant properties and sliding speeds. Furthermore, a force chain of fixed length can bear the same amount of load regardless of whether the particles are held together by lubrication forces, electrostatic repulsion, or attractive interactions. The current pool of evidence suggests that particle micromechanics contribute in a seemingly nonunique way to the bulk rheological phenomena. Therefore, physicists and engineers must continue to work together within the broader framework of experimental observations if we are to truly understand and design the contributions of interparticle forces and friction in the complex flows of dense suspensions.

1.7 Dissertation outline

This dissertation provides a guiding framework to design dense colloidal suspensions that contain smooth and rough colloids for linear and nonlinear rheological applications. In Chapter 2, we define a "contact" lengthscale in suspensions of smooth and rough colloids using arguments from jamming granular literature. Since the suspensions exhibit a shear modulus at the equilibrium states the lengthscale provides an estimate for average nearest neighbors that are involved in stress-transmission through these suspensions, even in a non-flowing state. In Chapter 3, we observe a universal correlation between the shear thickening strength and the jamming distance in all types of colloidal suspensions with particles maintaining spherical symmetry. Characterizing the microstructure in dynamic states in these suspensions enabled us to visualize contact networks, similar to that observed in sheared photoelastic granular materials. In Chapter 4, we probe the linear viscoelastic region in dense suspensions of smooth and rough particles and observed that rough colloidal suspension moduli values are thousand times higher than that of suspensions with smooth colloids. Using time-concentration superposition, we explained the difference in cage dynamics between the two types of suspensions in the vicinity of glass transition. In Chapter 5, we describe the summarizing remarks and outline future prospects in this research field.

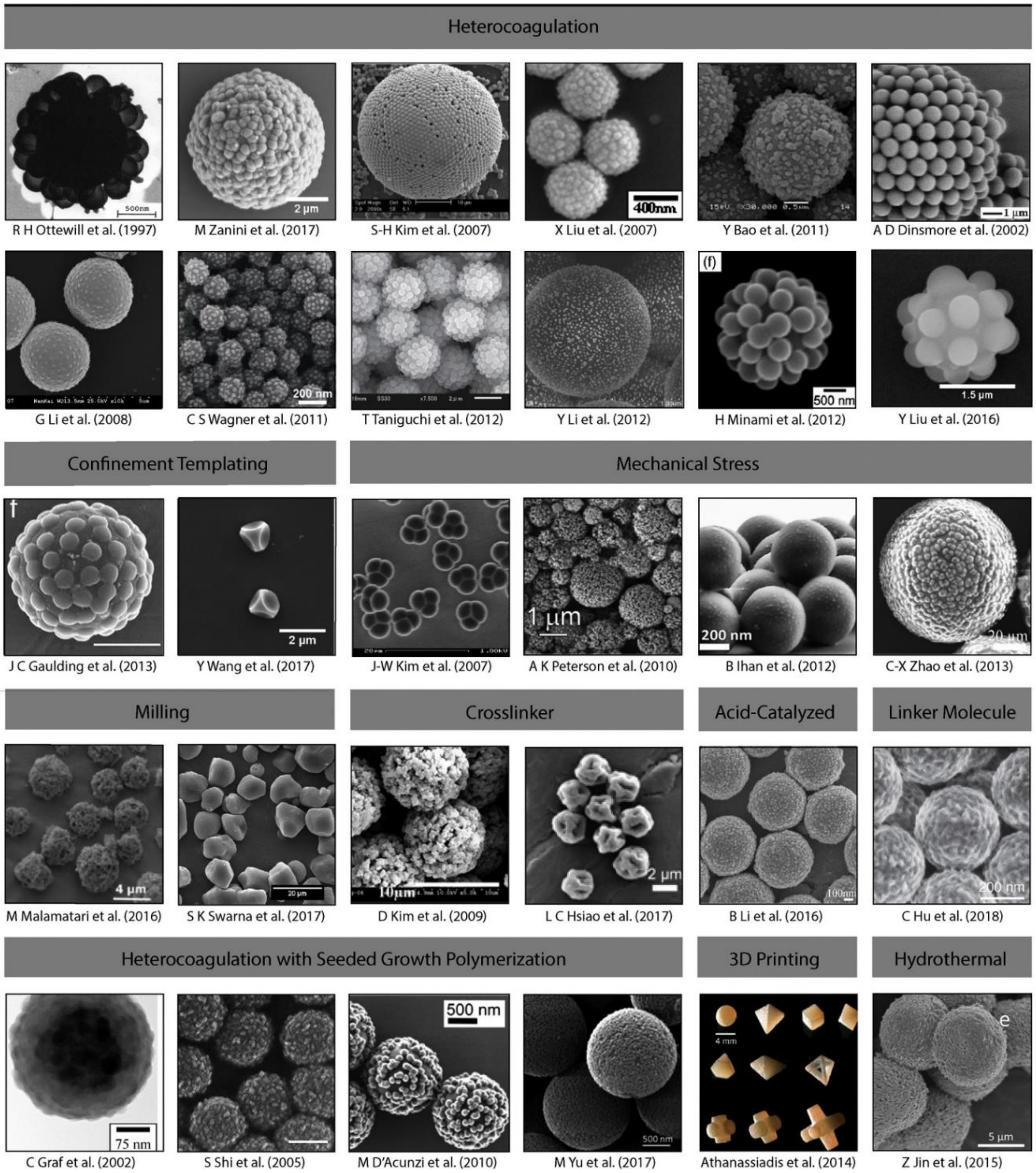

Figure 1.1 | Surface morphologies accessible for symmetric rough particles and their synthesis methods. Most of these micron-sized colloidal particles are synthesized by wet chemistry methods, although 3D printing is also able to fabricate large quantities of granular particles with arbitrary shapes.

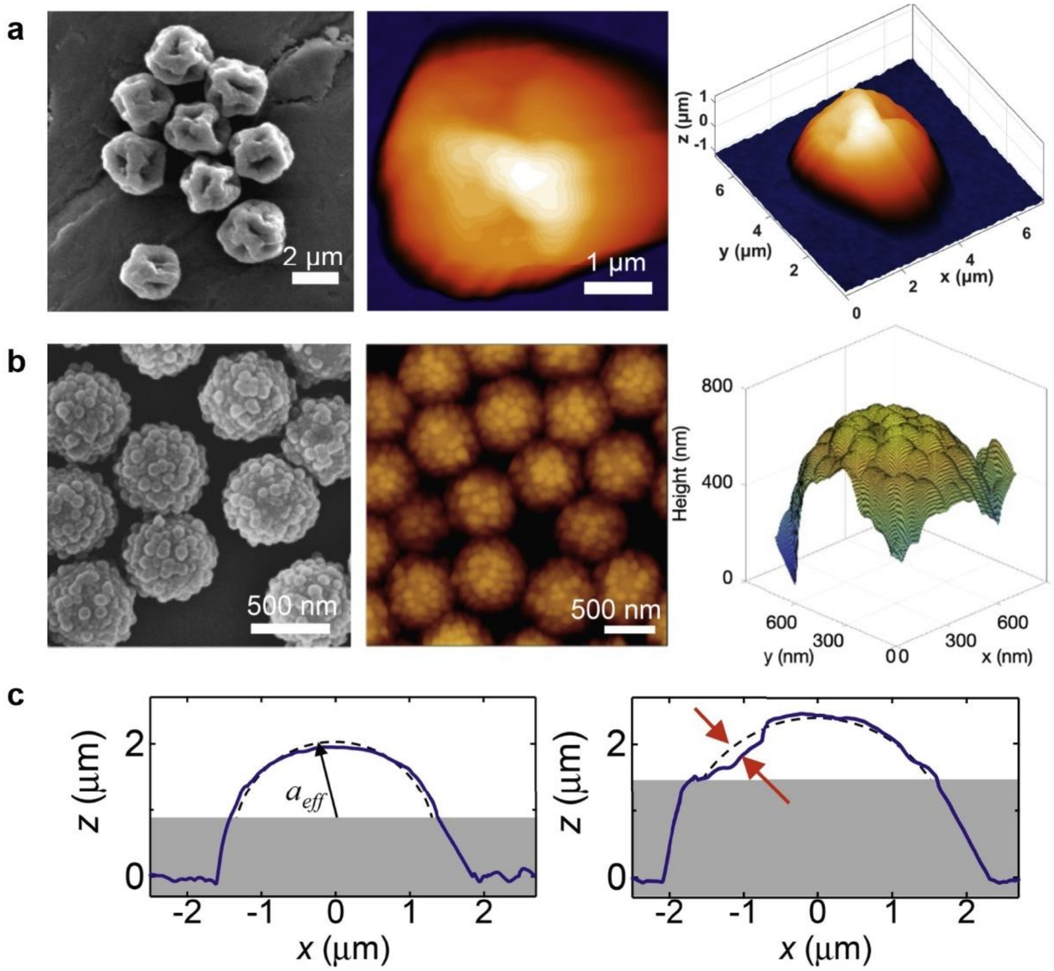

Figure 1.2 | Measurements and quantification of surface roughness for particles. Atomic force microscopy (AFM) is one of the most viable methods of probing surface roughness, as long as the particles are fixed on a flat substrate. The surface morphology of (a) sterically stabilized PMMA colloids and (b) raspberry-like silica colloids has been successfully quantified using AFM. (c) The root-mean-squared roughness values for smooth (left) and rough (right) PMMA colloids are calculated by fitting an effective sphere of radius a_{eff} to the raw data, then minimizing the deviation (red arrows) between the measured profiles and the fitted sphere. Because the AFM tip is likely to produce imaging artifacts near the edge of the particles, regions below a certain height z (indicated by gray areas) should not be considered for analysis.

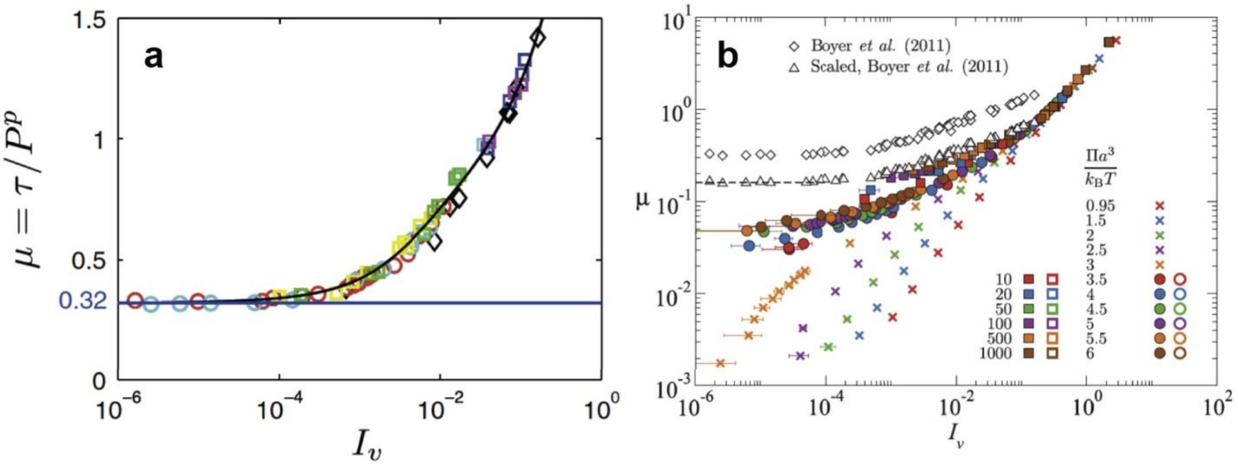

Figure 1.3 | Macroscopic *μ*(I) rheology show commonalities in dense granular and colloidal suspensions. (a) Experiments by Boyer et al. in a pressure controlled Couette shear cell showed that the bulk stress ratio plotted against the viscous number for a dense suspension of millimeter-sized beads ($\phi = 0.565$) collapse on a master curve. The solvent is a Newtonian fluid. (b) Brownian Dynamics simulations by Wang and Brady using a pressure-controlled simulation box, enabled by a compressible solvent, showed that hard-sphere colloidal suspensions without friction or lubrication hydrodynamics exhibit qualitatively similar rheology.

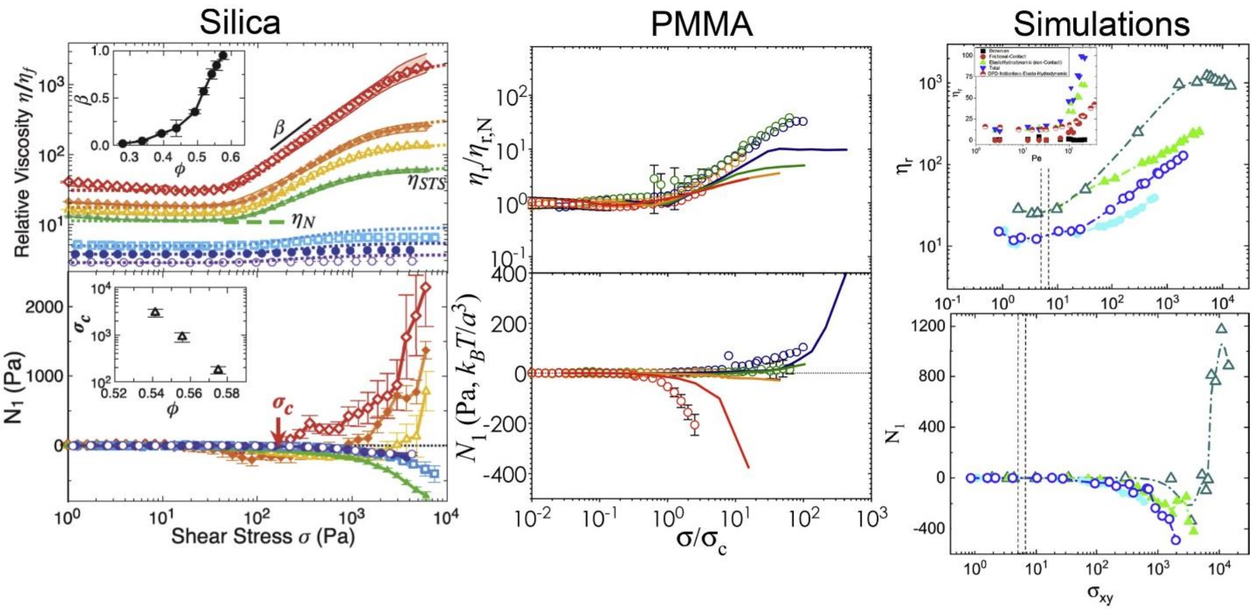

Figure 1.4 | Experiments and simulations of shear thickening suspensions agree when interparticle tangential friction is considered along with lubrication hydrodynamics. Dense suspensions of silica and poly(methyl methacrylate) (PMMA) colloids exhibited larger increases in the measured viscosities as ϕ and σ increase, representing a transition from weak to strong shear thickening. The first normal stress differences transitioned from negative to positive signs, reminiscent of granular dilatancy in which particles push against their confining boundaries to maintain flowing states. Surface roughness shifts these transition points to lower values of ϕ and σ. When interparticle friction was explicitly entered into the equations of motion in dissipative particle dynamics simulations, they captured a qualitatively similar trend as the experiments.

References

[1] C. Ness, R. Mari, and M. E. Cates, Science Advances **4**, eaar3296 (2018).

[2] M. Zanini, C. Marschelke, S. E. Anachkov, E. Marini, A. Synytska, and L. Isa, Nature Communications **8**, 15701 (2017).

[3] M. Houssais, C. P. Ortiz, D. J. Durian, and D. J. Jerolmack, Nature Communications **6**, 6527 (2015).

[4] A. Athanasopoulos-Zekkos and R. B. Seed, Journal of Geotechnical and Geoenvironmental Engineering **139**, 1911 (2013).

[5] B. Ferdowsi, C. P. Ortiz, and D. J. Jerolmack, Proceedings of the National Academy of Sciences **115**, 4827 (2018).

[6] E. Brown, N. Rodenberg, J. Amend, A. Mozeika, E. Steltz, M. R. Zakin, H. Lipson, and H. M. Jaeger, Proceedings of the National Academy of Sciences (2010).

[7] Y. S. Lee and N. Wagner, Rheologica Acta **42**, 199 (2003).

[8] A. Einstein, Annalen der Physik **324**, 371 (1906).

[9] O. Reynolds, The London, Edinburgh, and Dublin Philosophical Magazine and Journal of Science **20**, 469 (1885).

[10] J. Mewis and N. J. Wagner, *Colloidal Suspension Rheology* (Cambridge University Press, Cambridge, 2011), Cambridge Series in Chemical Engineering.

[11] N. J. Wagner and J. F. Brady, Physics Today **62**, 27 (2009).

[12] L. C. Hsiao, S. Jamali, E. Glynos, P. F. Green, R. G. Larson, and M. J. Solomon, Physical Review Letters **119**, 158001 (2017).

[13] E. Brown and H. M. Jaeger, Reports on Progress in Physics **77**, 046602 (2014).

[14] C.-P. Hsu, S. N. Ramakrishna, M. Zanini, N. D. Spencer, and L. Isa, Proceedings of the National Academy of Sciences **115**, 5117 (2018).

[15] N. Fernandez *et al.*, Physical Review Letters **111**, 108301 (2013).

[16] Y. Madraki, S. Hormozi, G. Ovarlez, É. Guazzelli, and O. Pouliquen, Physical Review Fluids **2**, 033301 (2017).

[17] D. Bi, J. Zhang, B. Chakraborty, and R. P. Behringer, Nature **480**, 355 (2011).

[18] N. M. James, E. Han, R. A. L. de la Cruz, J. Jureller, and H. M. Jaeger, Nature Materials **17**, 965 (2018).

[19] D. Lootens, H. Van Damme, and P. Hébraud, Physical Review Letters **90**, 178301 (2003).

[20] S. Gallier, E. Lemaire, F. Peters, and L. Lobry, Journal of Fluid Mechanics **757**, 514 (2014).

[21] D. Lootens, H. van Damme, Y. Hémar, and P. Hébraud, Physical Review Letters **95**, 268302 (2005).

[22] R. Seto, R. Mari, J. F. Morris, and M. M. Denn, Physical Review Letters **111**, 218301 (2013).

[23] M. Wyart and M. E. Cates, Physical Review Letters **112**, 098302 (2014).

[24] R. C. Ball and J. R. Melrose, Advances in Colloid and Interface Science **59**, 19 (1995).

[25] P. W. Rowe and G. I. Taylor, Proceedings of the Royal Society of London. Series A. Mathematical and Physical Sciences **269**, 500 (1962).

[26] M. von Smoluchowski, Annalen der Physik **326**, 756 (1906).

[27] G. I. Taylor, Proceedings of the Royal Society of London. Series A, Containing Papers of a Mathematical and Physical Character **138**, 41 (1932).

[28] J. J. Stickel and R. L. Powell, Annual Review of Fluid Mechanics **37**, 129 (2005).

[29] J. Mewis and N. J. Wagner, Journal of Non-Newtonian Fluid Mechanics **157**, 147 (2009).

[30] J. F. Morris, Rheologica Acta **48**, 909 (2009).

[31] Y. Forterre and O. Pouliquen, Annual Review of Fluid Mechanics **40**, 1 (2008).

[32] J. F. Morris, Physical Review Fluids **3**, 110508 (2018).

[33] S. Jamali, A. Boromand, N. Wagner, and J. Maia, Journal of Rheology **59**, 1377 (2015).

[34] J. T. Jenkins and S. B. Savage, Journal of Fluid Mechanics **130**, 187 (1983).

[35] B. Kaffashi, V. T. O'Brien, M. E. Mackay, and S. M. Underwood, Journal of Colloid and Interface Science **187**, 22 (1997).

[36] P. N. Pusey and W. van Megen, Nature **320**, 340 (1986).

[37] G. K. Batchelor, Journal of Fluid Mechanics **83**, 97 (1977).

[38] R. A. Lionberger and W. B. Russel, Journal of Rheology **38**, 1885 (1994).

[39] S.-E. Phan, W. B. Russel, Z. Cheng, J. Zhu, P. M. Chaikin, J. H. Dunsmuir, and R. H. Ottewill, Physical Review E **54**, 6633 (1996).

[40] L. E. Silbert, J. R. Melrose, and R. C. Ball, Journal of Rheology **43**, 673 (1999).

[41] W. Schaertl and H. Sillescu, Journal of Statistical Physics **77**, 1007 (1994).

[42] W. B. Russel, D. A. Saville, and W. R. Schowalter, *Colloidal Dispersions* (Cambridge University Press, Cambridge, 1989), Cambridge Monographs on Mechanics.

[43] D. Dendukuri and P. S. Doyle, Advanced Materials **21**, 4071 (2009).

[44] W. Stöber, A. Fink, and E. Bohn, Journal of Colloid and Interface Science **26**, 62 (1968).

[45] Y. J. Wong, L. Zhu, W. S. Teo, Y. W. Tan, Y. Yang, C. Wang, and H. Chen, Journal of the American Chemical Society **133**, 11422 (2011).

[46] A. K. Van Helden, J. W. Jansen, and A. Vrij, Journal of Colloid and Interface Science **81**, 354 (1981).

[47] A. T. J. M. Woutersen, R. P. May, and C. G. de Kruif, Journal of Colloid and Interface Science **151**, 410 (1992).

[48] A. P. R. Eberle, R. Castañeda-Priego, J. M. Kim, and N. J. Wagner, Langmuir **28**, 1866 (2012).

[49] P. Varadan and M. J. Solomon, Journal of Rheology **47**, 943 (2003).

[50] K. A. Whitaker and E. M. Furst, Langmuir **30**, 584 (2014).

[51] A. P. R. Eberle, N. J. Wagner, and R. Castañeda-Priego, Physical Review Letters **106**, 105704 (2011).

[52] J. M. Kim, J. Fang, A. P. R. Eberle, R. Castañeda-Priego, and N. J. Wagner, Physical Review Letters **110**, 208302 (2013).

[53] M. Chen and W. B. Russel, Journal of Colloid and Interface Science **141**, 564 (1991).

[54] M. A. Miller and D. Frenkel, The Journal of Chemical Physics **121**, 535 (2004).

[55] S. C. Thickett and R. G. Gilbert, Polymer **48**, 6965 (2007).

[56] H. Pertoft, T. C. Laurent, T. Låås, and L. Kågedal, Analytical Biochemistry **88**, 271 (1978).

[57] L. C. Hsiao, R. S. Newman, S. C. Glotzer, and M. J. Solomon, Proceedings of the National Academy of Sciences **109**, 16029 (2012).

[58] H. Tsurusawa, J. Russo, M. Leocmach, and H. Tanaka, Nature Materials **16**, 1022 (2017).

[59] T. E. Kodger, R. E. Guerra, and J. Sprakel, Scientific Reports **5**, 14635 (2015).

[60] L. Antl, J. W. Goodwin, R. D. Hill, R. H. Ottewill, S. M. Owens, S. Papworth, and J. A. Waters, Colloids and Surfaces **17**, 67 (1986).

[61] G. Bryant, S. R. Williams, L. Qian, I. K. Snook, E. Perez, and F. Pincet, Physical Review E **66**, 060501 (2002).

[62] M. T. Elsesser and A. D. Hollingsworth, Langmuir **26**, 17989 (2010).

[63] G. Bosma, C. Pathmamanoharan, E. H. A. de Hoog, W. K. Kegel, A. van Blaaderen, and H. N. W. Lekkerkerker, Journal of Colloid and Interface Science **245**, 292 (2002).

[64] L. Palangetic, K. Feldman, R. Schaller, R. Kalt, W. R. Caseri, and J. Vermant, Faraday Discussions **191**, 325 (2016).

[65] U. Capasso Palmiero, A. Agostini, E. Lattuada, S. Gatti, J. Singh, C. T. Canova, S. Buzzaccaro, and D. Moscatelli, Soft Matter **13**, 6439 (2017).

[66] S. Auer, W. C. K. Poon, and D. Frenkel, Physical Review E **67**, 020401 (2003).

[67] B. M. Guy, M. Hermes, and W. C. K. Poon, Physical Review Letters **115**, 088304 (2015).

[68] B. A. L. Costello, P. F. Luckham, and T. F. Tadros, Langmuir **8**, 464 (1992).

[69] M. J. Solomon, Langmuir **34**, 11205 (2018).

[70] N. Park and J. C. Conrad, Soft Matter **13**, 2781 (2017).

[71] W. C. K. Poon, E. R. Weeks, and C. P. Royall, Soft Matter **8**, 21 (2012).

[72] G. M. Conley, P. Aebischer, S. Nöjd, P. Schurtenberger, and F. Scheffold, Science Advances **3**, e1700969 (2017).

[73] L. Mohan, R. T. Bonnecaze, and M. Cloitre, Physical Review Letters **111**, 268301 (2013).

[74] Y. Peng, F. Wang, Z. Wang, A. M. Alsayed, Z. Zhang, A. G. Yodh, and Y. Han, Nature Materials **14**, 101 (2015).

[75] A. C. Brown *et al.*, Nature Materials **13**, 1108 (2014).

[76] L.-W. Xia, R. Xie, X.-J. Ju, W. Wang, Q. Chen, and L.-Y. Chu, Nature Communications **4**, 2226 (2013).

[77] K. V. Edmond, M. T. Elsesser, G. L. Hunter, D. J. Pine, and E. R. Weeks, Proceedings of the National Academy of Sciences **109**, 17891 (2012).

[78] J. Palacci, S. Sacanna, A. P. Steinberg, D. J. Pine, and P. M. Chaikin, Science **339**, 936 (2013).

[79] É. Ducrot, M. He, G.-R. Yi, and D. J. Pine, Nature Materials **16**, 652 (2017).

[80] S. Sacanna, W. T. M. Irvine, P. M. Chaikin, and D. J. Pine, Nature **464**, 575 (2010).

[81] D. K. Kim, Y. Zhang, W. Voit, K. V. Rao, and M. Muhammed, Journal of Magnetism and Magnetic Materials **225**, 30 (2001).

[82] B. Bharti, A.-L. Fameau, M. Rubinstein, and O. D. Velev, Nature Materials **14**, 1104 (2015).

[83] J. W. Swan, J. L. Bauer, Y. Liu, and E. M. Furst, Soft Matter **10**, 1102 (2014).

[84] G. N. Smith *et al.*, Journal of Colloid and Interface Science **479**, 234 (2016).

[85] E. Bilgili, R. Hamey, and B. Scarlett, Chemical Engineering Science **61**, 149 (2006).

[86] H. J. Fecht, E. Hellstern, Z. Fu, and W. L. Johnson, Metallurgical Transactions A **21**, 2333 (1990).

[87] M. T. Gokmen and F. E. Du Prez, Progress in Polymer Science **37**, 365 (2012).

[88] G. E. Yakubov, T. E. Branfield, J. H. H. Bongaerts, and J. R. Stokes, Biotribology **3**, 1 (2015).

[89] in *Engineering Tribology (Fourth Edition)*, edited by G. W. Stachowiak, and A. W. Batchelor (Butterworth-Heinemann, Boston, 2014), pp. 105.

[90] Y. Altintaş and E. Budak, CIRP Annals **44**, 357 (1995).

[91] D. Montgomery and Y. Altintas, Journal of Engineering for Industry **113**, 160 (1991).

[92] S. P. Chamarthy and R. Pinal, Colloids and Surfaces A: Physicochemical and Engineering Aspects **331**, 68 (2008).

[93] E. Yoğurtcuoğlu and M. Uçurum, Powder Technology **214**, 47 (2011).

[94] A. Fall, N. Huang, F. Bertrand, G. Ovarlez, and D. Bonn, Physical Review Letters **100**, 018301 (2008).

[95] B. Saint-Michel, T. Gibaud, and S. Manneville, Physical Review X **8**, 031006 (2018).

[96] R. H. Ottewill, A. B. Schofield, J. A. Waters, and N. S. J. Williams, Colloid and Polymer Science **275**, 274 (1997).

[97] A. D. Dinsmore, M. F. Hsu, M. G. Nikolaides, M. Marquez, A. R. Bausch, and D. A. Weitz, Science **298**, 1006 (2002).

[98] T. Taniguchi, S. Obi, Y. Kamata, T. Kashiwakura, M. Kasuya, T. Ogawa, M. Kohri, and T. Nakahira, Journal of Colloid and Interface Science **368**, 107 (2012).

[99] G. Li, X. Yang, F. Bai, and W. Huang, Journal of Colloid and Interface Science **297**, 705 (2006).

[100] M. Zanini, C.-P. Hsu, T. Magrini, E. Marini, and L. Isa, Colloids and Surfaces A: Physicochemical and Engineering Aspects **532**, 116 (2017).

[101] D. Kim, D. Y. Lee, K. Lee, and S. Choe, Macromolecular Research **17**, 250 (2009).

[102] M. Yu, Q. Wang, M. Zhang, Q. Deng, and D. Chen, RSC Advances **7**, 39471 (2017).

[103] G. Li, X. Yang, and J. Wang, Colloids and Surfaces A: Physicochemical and Engineering Aspects **322**, 192 (2008).

[104] Y. Liu, K. V. Edmond, A. Curran, C. Bryant, B. Peng, D. G. A. L. Aarts, S. Sacanna, and R. P. A. Dullens, Advanced Materials **28**, 8001 (2016).

[105] S. Shi, S. Kuroda, K. Hosoi, and H. Kubota, Polymer **46**, 3567 (2005).

[106] C. Graf, D. L. J. Vossen, A. Imhof, and A. van Blaaderen, Langmuir **19**, 6693 (2003).

[107] M. D'Acunzi, L. Mammen, M. Singh, X. Deng, M. Roth, G. K. Auernhammer, H.-J. Butt, and D. Vollmer, Faraday Discussions **146**, 35 (2010).

[108] J. C. Gaulding, S. Saxena, D. E. Montanari, and L. A. Lyon, ACS Macro Letters **2**, 337 (2013).

[109] Y. Wang, J. T. McGinley, and J. C. Crocker, Langmuir **33**, 3080 (2017).

[110] A. K. Peterson, D. G. Morgan, and S. E. Skrabalak, Langmuir **26**, 8804 (2010).

[111] B. İlhan, C. Annink, D. V. Nguyen, F. Mugele, I. Siretanu, and M. H. G. Duits, Colloids and Surfaces A: Physicochemical and Engineering Aspects **560**, 50 (2019).

[112] C.-X. Zhao and A. P. J. Middelberg, RSC Advances **3**, 21227 (2013).

[113] J.-W. Kim, R. J. Larsen, and D. A. Weitz, Advanced Materials **19**, 2005 (2007).

[114] R. Rice, R. Roth, and C. P. Royall, Soft Matter **8**, 1163 (2012).

[115] K. Tamareselvy and F. A. Rueggeberg, Dental Materials **10**, 290 (1994).

[116] Z. Jin, J. Li, L. Shi, Y. Ji, Z. Zhong, and F. Su, Applied Surface Science **359**, 120 (2015).

[117] B. Li, X. Gao, J. Zhang, Y. Sun, and Z. Liu, Powder Technology **292**, 80 (2016).

[118] C. Hu, J. Liu, Y. Wu, K. R. West, and O. A. Scherman, Small **14**, 1703352 (2018).

[119] S. Utermann, P. Aurin, M. Benderoth, C. Fischer, and M. Schröter, Physical Review E **84**, 031306 (2011).

[120] F. Tapia, O. Pouliquen, and É. Guazzelli, Physical Review Fluids **4**, 104302 (2019).

[121] J. Zhao, M. Jiang, K. Soga, and S. Luding, Granular Matter **18**, 59 (2016).

[122] A. G. Athanassiadis *et al.*, Soft Matter **10**, 48 (2014).

[123] G. R. Farrell, K. M. Martini, and N. Menon, Soft Matter **6**, 2925 (2010).

[124] R. Jones, H. M. Pollock, D. Geldart, and A. Verlinden-Luts, Ultramicroscopy **100**, 59 (2004).

[125] A. A. Feiler, J. Stiernstedt, K. Theander, P. Jenkins, and M. W. Rutland, Langmuir **23**, 517 (2007).

[126] S. Zauscher and D. J. Klingenberg, Colloids and Surfaces A: Physicochemical and Engineering Aspects **178**, 213 (2001).

[127] J. Comtet, G. Chatté, A. Niguès, L. Bocquet, A. Siria, and A. Colin, Nature Communications **8**, 15633 (2017).

[128] S. Nasuno, A. Kudrolli, A. Bak, and J. P. Gollub, Physical Review E **58**, 2161 (1998).

[129] D. M. Mueth, H. M. Jaeger, and S. R. Nagel, Physical Review E **57**, 3164 (1998).

[130] Y. C. Zhou, B. H. Xu, A. B. Yu, and P. Zulli, Powder Technology **125**, 45 (2002).

[131] J. Härtl and J. Y. Ooi, Granular Matter **10**, 263 (2008).

[132] J. F. Hubler, A. Athanasopoulos-Zekkos, and D. Zekkos, Journal of Geotechnical and Geoenvironmental Engineering **143**, 04017043 (2017).

[133] C. P. Ortiz, R. Riehn, and K. E. Daniels, Soft Matter **9**, 543 (2013).

[134] F. Podczeck, J. M. Newton, and M. B. James, Journal of Materials Science **31**, 2213 (1996).

[135] X. Ling, H.-J. Butt, and M. Kappl, Langmuir **23**, 8392 (2007).

[136] S. Ecke and H.-J. Butt, Journal of Colloid and Interface Science **244**, 432 (2001).

[137] J. N. Israelachvili and D. Tabor, Proceedings of the Royal Society of London. A. Mathematical and Physical Sciences **331**, 19 (1972).

[138] S. Biggs, Langmuir **11**, 156 (1995).

[139] L.-O. Heim, J. Blum, M. Preuss, and H.-J. Butt, Physical Review Letters **83**, 3328 (1999).

[140] J. M. Bennett, Appl. Opt. **15**, 2705 (1976).

[141] B. N. J. Persson, O. Albohr, U. Tartaglino, A. I. Volokitin, and E. Tosatti, Journal of Physics: Condensed Matter **17**, R1 (2004).

[142] R. S. Sayles and T. R. Thomas, Nature **271**, 431 (1978).

[143] J. A. Greenwood and K. L. Johnson, Proceedings of the Royal Society of London. A. Mathematical and Physical Sciences **393**, 133 (1984).

[144] E. Sidick, *Power spectral density specification and analysis of large optical surfaces* (SPIE, 2009), Vol. 7390, SPIE Europe Optical Metrology, p.^pp. EOM.

[145] A. J. McGhee *et al.*, Tribology Letters **65**, 157 (2017).

[146] S. Ecke, R. Raiteri, E. Bonaccurso, C. Reiner, H.-J. Deiseroth, and H.-J. Butt, Review of Scientific Instruments **72**, 4164 (2001).

[147] H.-J. Butt, B. Cappella, and M. Kappl, Surface Science Reports **59**, 1 (2005).

[148] S. C. d. Pont, P. Gondret, B. Perrin, and M. Rabaud, Europhysics Letters (EPL) **61**, 492 (2003).

[149] N. A. Pohlman, B. L. Severson, J. M. Ottino, and R. M. Lueptow, Physical Review E **73**, 031304 (2006).

[150] A. Lemaître, Physical Review Letters **89**, 195503 (2002).

[151] O. R. Walton and R. L. Braun, Journal of Rheology **30**, 949 (1986).

[152] D. Fenistein, J. W. van de Meent, and M. van Hecke, Physical Review Letters **92**, 094301 (2004).

[153] P. Sollich, F. Lequeux, P. Hébraud, and M. E. Cates, Physical Review Letters **78**, 2020 (1997).

[154] G. Ovarlez, Q. Barral, and P. Coussot, Nature Materials **9**, 115 (2010).

[155] L. E. Silbert, D. Ertaş, G. S. Grest, T. C. Halsey, D. Levine, and S. J. Plimpton, Physical Review E **64**, 051302 (2001).

[156] O. Pouliquen, Physics of Fluids **11**, 542 (1999).

[157] K. H. Zehtab, S. Gokyer, A. Apostolov, W. A. Marr, and S. K. Werden, in *Geotechnical Earthquake Engineering and Soil Dynamics V*2018), pp. 257.

[158] F. Boyer, É. Guazzelli, and O. Pouliquen, Physical Review Letters **107**, 188301 (2011).

[159] K. E. Daniels, J. E. Kollmer, and J. G. Puckett, Review of Scientific Instruments **88**, 051808 (2017).

[160] D. S. Bassett, E. T. Owens, M. A. Porter, M. L. Manning, and K. E. Daniels, Soft Matter **11**, 2731 (2015).

[161] T. S. Majmudar and R. P. Behringer, Nature **435**, 1079 (2005).

[162] L. Papadopoulos, M. A. Porter, K. E. Daniels, and D. S. Bassett, Journal of Complex Networks **6**, 485 (2018).

[163] J. Bender and N. J. Wagner, Journal of Rheology **40**, 899 (1996).

[164] C. D. Cwalina and N. J. Wagner, Journal of Rheology **58**, 949 (2014).

[165] L.-N. Krishnamurthy, N. J. Wagner, and J. Mewis, Journal of Rheology **49**, 1347 (2005).

[166] R. Mari, R. Seto, J. F. Morris, and M. M. Denn, Journal of Rheology **58**, 1693 (2014).

[167] R. Mari, R. Seto, J. F. Morris, and M. M. Denn, Physical Review E **91**, 052302 (2015).

[168] Y. Madraki, G. Ovarlez, and S. Hormozi, Physical Review Letters **121**, 108001 (2018).

[169] W. B. Russel, N. J. Wagner, and J. Mewis, Journal of Rheology **57**, 1555 (2013).

[170] A. Ikeda, L. Berthier, and P. Sollich, Physical Review Letters **109**, 018301 (2012).

[171] G. Brambilla, D. El Masri, M. Pierno, L. Berthier, L. Cipelletti, G. Petekidis, and A. B. Schofield, Physical Review Letters **102**, 085703 (2009).

[172] A. Ikeda, L. Berthier, and P. Sollich, Soft Matter **9**, 7669 (2013).

[173] R. G. Egres, F. Nettesheim, and N. J. Wagner, Journal of Rheology **50**, 685 (2006).

[174] E. Brown, N. A. Forman, C. S. Orellana, H. Zhang, B. W. Maynor, D. E. Betts, J. M. DeSimone, and H. M. Jaeger, Nature Materials **9**, 220 (2010).

[175] E. Brown and H. M. Jaeger, Journal of Rheology **56**, 875 (2012).

[176] I. R. Peters, S. Majumdar, and H. M. Jaeger, Nature **532**, 214 (2016).

[177] S. R. Waitukaitis and H. M. Jaeger, Nature **487**, 205 (2012).

[178] H. M. Laun, Journal of Non-Newtonian Fluid Mechanics **54**, 87 (1994).

[179] A. B. Metzner and M. Whitlock, Transactions of the Society of Rheology **2**, 239 (1958).

[180] J. R. Royer, D. L. Blair, and S. D. Hudson, Physical Review Letters **116**, 188301 (2016).

[181] B. J. Maranzano and N. J. Wagner, The Journal of Chemical Physics **114**, 10514 (2001).

[182] R. Mari, R. Seto, J. F. Morris, and M. M. Denn, Proceedings of the National Academy of Sciences **112**, 15326 (2015).

[183] J F Brady and G. Bossis, Annual Review of Fluid Mechanics **20**, 111 (1988).

[184] D. P. Kalman and N. J. Wagner, Rheologica Acta **48**, 897 (2009).

[185] A. K. Gurnon and N. J. Wagner, Journal of Fluid Mechanics **769**, 242 (2015).

[186] X. Cheng, J. H. McCoy, J. N. Israelachvili, and I. Cohen, Science **333**, 1276 (2011).

[187] J. R. Melrose and R. C. Ball, Journal of Rheology **48**, 937 (2004).

[188] D. R. Foss and J. F. Brady, Journal of Fluid Mechanics **407**, 167 (2000).

[189] J. F. Brady, The Journal of Chemical Physics **98**, 3335 (1993).

[190] A. Sierou and J. F. Brady, Journal of Rheology **46**, 1031 (2002).

[191] M. E. Cates, M. D. Haw, and C. B. Holmes, Journal of Physics: Condensed Matter **17**, S2517 (2005).

[192] F. Gadala-Maria and A. Acrivos, Journal of Rheology **24**, 799 (1980).

[193] G. K. Batchelor and J. T. Green, Journal of Fluid Mechanics **56**, 375 (1972).

[194] J. F. Brady, R. J. Phillips, J. C. Lester, and G. Bossis, Journal of Fluid Mechanics **195**, 257 (1988).

[195] J. F. Brady, Journal of Fluid Mechanics **272**, 109 (1994).

[196] J. Bergenholtz, J. F. Brady, and M. Vicic, Journal of Fluid Mechanics **456**, 239 (2002).

[197] R. T. Bonnecaze, G. J. Rodin, R. H. Davis, Y. Zhao, K. P. Galvin, and H. J. Wilson, Philosophical Transactions of the Royal Society of London. Series A: Mathematical, Physical and Engineering Sciences **361**, 871 (2003).

[198] H. J. Wilson and R. H. Davis, Journal of Fluid Mechanics **452**, 425 (2002).

[199] J. R. Smart, S. Beimfohr, and D. T. L. Jr., Physics of Fluids A: Fluid Dynamics **5**, 13 (1993).

[200] F. R. Da Cunha and E. J. Hinch, Journal of Fluid Mechanics **309**, 211 (1996).

[201] R. P. Behringer and B. Chakraborty, Reports on Progress in Physics **82**, 012601 (2018).

[202] O. Pouliquen and F. Chevoir, Comptes Rendus Physique **3**, 163 (2002).

[203] C. K. K. Lun and S. B. Savage, Journal of Applied Mechanics **54**, 47 (1987).

[204] G. D. R. MiDi, The European Physical Journal E **14**, 341 (2004).

[205] A. J. Liu and S. R. Nagel, Nature **396**, 21 (1998).

[206] C. S. O’Hern, L. E. Silbert, A. J. Liu, and S. R. Nagel, Physical Review E **68**, 011306 (2003).

[207] B. Luan and M. O. Robbins, Nature **435**, 929 (2005).

[208] M. E. Cates, J. P. Wittmer, J. P. Bouchaud, and P. Claudin, Physical Review Letters **81**, 1841 (1998).

[209] Z. Pan, H. de Cagny, B. Weber, and D. Bonn, Physical Review E **92**, 032202 (2015).

[210] H. d. Cagny, A. Fall, M. M. Denn, and D. Bonn, Journal of Rheology **59**, 957 (2015).

[211] J. E. Thomas, K. Ramola, A. Singh, R. Mari, J. F. Morris, and B. Chakraborty, Physical Review Letters **121**, 128002 (2018)..

[212] H. A. Vinutha and S. Sastry, Nature Physics **12**, 578 (2016).

[213] K. Kamrin and G. Koval, Physical Review Letters **108**, 178301 (2012).

[214] M. Bouzid, M. Trulsson, P. Claudin, E. Clément, and B. Andreotti, Physical Review Letters **111**, 238301 (2013).

[215] Z. Tang, T. A. Brzinski, M. Shearer, and K. E. Daniels, Soft Matter **14**, 3040 (2018).

[216] A. Boromand, S. Jamali, B. Grove, and J. M. Maia, Journal of Rheology **62**, 905 (2018).

[217] N. Y. C. Lin, B. M. Guy, M. Hermes, C. Ness, J. Sun, W. C. K. Poon, and I. Cohen, Physical Review Letters **115**, 228304 (2015).

[218] C. Clavaud, A. Bérut, B. Metzger, and Y. Forterre, Proceedings of the National Academy of Sciences **114**, 5147 (2017).

[219] R. A. Bagnold, Proceedings of the Royal Society of London. Series A. Mathematical and Physical Sciences **225**, 49 (1954).

[220] M. Wang and J. F. Brady, Physical Review Letters **115**, 158301 (2015).

[221] T. Kawasaki, D. Coslovich, A. Ikeda, and L. Berthier, Physical Review E **91**, 012203 (2015).

[222] M. van Hecke, Journal of Physics: Condensed Matter **22**, 033101 (2009).

[223] S. Papanikolaou, C. S. O'Hern, and M. D. Shattuck, Physical Review Letters **110**, 198002 (2013).

[224] L. E. Silbert, Soft Matter **6**, 2918 (2010).

[225] M. P. Ciamarra, R. Pastore, M. Nicodemi, and A. Coniglio, Physical Review E **84**, 041308 (2011).

[226] A. Fall, G. Ovarlez, D. Hautemayou, C. Mézière, J.-N. Roux, and F. Chevoir, Journal of Rheology **59**, 1065 (2015).

[227] R. N. Chacko, R. Mari, M. E. Cates, and S. M. Fielding, Physical Review Letters **121**, 108003 (2018).

[228] G. He, M. H. Müser, and M. O. Robbins, Science **284**, 1650 (1999).

[229] C. Marone, Annual Review of Earth and Planetary Sciences **26**, 643 (1998).

[230] A. Fall, B. Weber, M. Pakpour, N. Lenoir, N. Shahidzadeh, J. Fiscina, C. Wagner, and D. Bonn, Physical Review Letters **112**, 175502 (2014).

[231] R. I. Tanner and S. Dai, Journal of Rheology **60**, 809 (2016).

[232] J. E. Thomas, K. Ramola, A. Singh, R. Mari, J. F. Morris, and B. Chakraborty, Physical Review Letters **121**, 128002 (2018).

[233] Z. Pan, H. de Cagny, M. Habibi, and D. Bonn, Soft Matter **13**, 3734 (2017).

[234] F. Ianni, D. Lasne, R. Sarcia, and P. Hébraud, Physical Review E **74**, 011401 (2006).

[235] L. C. Hsiao, I. Saha-Dalal, R. G. Larson, and M. J. Solomon, Soft Matter **13**, 9229 (2017).

[236] B. M. Guy, J. A. Richards, D. J. M. Hodgson, E. Blanco, and W. C. K. Poon, Physical Review Letters **121**, 128001 (2018).

[237] E. DeGiuli, G. Düring, E. Lerner, and M. Wyart, Physical Review E **91**, 062206 (2015).

CHAPTER 2

Contact criterion for suspensions of smooth and rough colloids[†]

[†]Shravan Pradeep and Lilian C. Hsiao, *Soft Matter*, 16, 4980-4989 (2020)

Department of Chemical and Biomolecular Engineering, North Carolina State University,

Raleigh, NC 27695, USA

Abstract

We report a procedure to obtain the search distance used to determine particle contact in dense suspensions of smooth and rough colloids. This method works by summing physically relevant length scales in an uncertainty analysis and does not require detailed quantification of the surface roughness. We suspend sterically stabilized, fluorescent poly(methyl methacrylate) colloids suspended in a refractive index-matched solvent, squalene, in order to ensure hard sphere-like behavior. High speed centrifugation is used to pack smooth and rough colloids to their respective jamming points, ϕ_J. The jammed suspensions are subsequently diluted with known volumes of solvent to $\phi < \phi_J$. Structural parameters obtained from confocal laser scanning micrographs of the diluted colloidal suspensions are extrapolated to ϕ_J determine the mean contact number at jamming, $<z>_J$. Contact below jamming refers to a length scale below which the effects of hydrodynamic or geometric friction come into play. Sensitivity analyses show that a deviation of the search distance by 1% of the particle diameter results in $<z>$ changing by up to 10%, with the error in contact number distribution being magnified in dense suspensions ($\phi > 0.50$) due to an increased number of nearest neighbors in the first coordination shell.

2.1 Introduction

Grains, colloids, foams, and emulsions belong to a class of particulate suspensions found in many scientific and technological applications, ranging from geophysical phenomena to consumer goods. The mechanical load-bearing properties of these materials become significant when the constituent particles are densely packed together in the absence of attractive interactions. As more and more particles are added to the suspension, each particle experiences a caging effect from its nearest neighbors, along with hydrodynamic effects from the suspending fluid. The entire material jams when the particle volume fraction ϕ increases to a point near random close packing (RCP): it transitions from a free-flowing state to a rigid state with an effectively infinite zero-shear viscosity [1,2]. The nature of this transition depends on a number of material parameters such as thermal fluctuations, particle deformability, the softness of the interaction potential, and the shape and morphology of the particles. Jamming is widely observed in biological and engineered systems: diseased cells tend to jam more readily than their healthy counterparts[3], flocks of sheep jam when herded through gates[4], and grains discharging from silos may become "stuck" [5].

Seminal work by Liu and Nagel [6], as well as by O'Hern and coworkers[7], established a jamming state diagram for particulate matter based on temperature, load, and density. The mean contact number $<z>$, the average number of contacting neighbors for a particle, was identified as a crucial microscopic parameter that is intimately coupled to the jamming point of athermal suspensions in which hydrodynamic contributions from the continuum are small. The rationale is that contacts between particles generate force chains that sum up to the overall stress in a material [8-12]. When the force chains become space-spanning and zero floppy modes of deformation remain, the particulate material becomes mechanically rigid at the isostatic condition, where the contact number is $z_{iso} = 6$ for frictionless spheres [2]. Follow-on experiments and simulations have since confirmed the strong connection between $<z>$ and the bulk modulus of various materials with and without interparticle attraction. The viscoelasticity of attractive colloidal gels is attributed to the contact number distribution within strands that contain particles at volume fractions ϕ near random close packing (ϕ_{RCP}), which in turn affects their structural and dynamical evolution [13-18]. Simulations of soft repulsive spheres interacting through Hertzian contacts and an interparticle friction μ_{p} show that the shear modulus scaled with bulk modulus or material stiffness exhibits a linear power-law scaling with respect to the excess contact number, $\Delta z = <z> - z_{\mathrm{iso}}$ [19-22]. When prolate and oblate spheroids of different aspect ratios are used, ϕ_{RCP} increases, with a corresponding increase in $<z>$ at RCP [23,24]. More recently, the deformable particle model enables arbitrary particle shapes to be described by an energy function that captures the onset of jamming for 2D deformable polygons [25]. Experimental approaches have utilized granocentric models to capture the jammed microstructure of polydisperse emulsion packings [26,27]. Importantly, the correlation between mechanics and contact microstructure scales as the distance to jamming $<z> - z_{\mathrm{J}}$ and $\phi - \phi_{\mathrm{J}}$, where the subscript *J* refers to the jamming point. This correlation uses the excess parameters instead of the absolute value of ϕ or $<z>$, because z_{J} and ϕ_{J} change depending on particle properties and how the packing is generated. As an example, the scaling behavior of properties such as elastic modulus, external osmotic pressure, and low-frequency modulus had been correlated with the distance from the RCP structure in compressed emulsions [28,29]. The idea of scaling with the distance to jamming is widely accepted in the granular matter literature but has not yet been experimentally validated in the field of colloidal suspensions.

The key difference between the two types of particulates is that colloidal suspensions exhibit thermal fluctuations over experimental time scales, while granular media are athermal in nature. The diffusive motion of the colloids generates a hydrodynamic resistance that contributes to the suspension stress in dilute conditions [30]. As ϕ increases beyond ≈ 0.50, calculations of suspension stress based solely on near- and far-field hydrodynamics begin to perform poorly [31,32], likely because the contact stresses between particles become more granular-like [33]. However, unlike the case of athermal grains where a pile will not support any stress unless it is at $\phi \geq \phi_{\mathrm{RLP}}$, where RLP is the random loose packing state,[34] stochastic Brownian fluctuations in colloidal suspensions give rise to transient clusters that support a finite viscoelasticity below ϕ_{RCP}. The viscoelasticity and rheology of the hard-sphere colloidal suspensions close to RCP is very well established [35-37]. Experimentally, a connection between colloidal and granular shear thickening was made using hard sphere particles of moderate sizes ($1\ \mu\mathrm{m} \leq 2a \leq 50\ \mu\mathrm{m}$) [38]. Additionally, particles with surface asperities possess greater interparticle friction than their smooth counterparts [39,40] and this results in flow with greater hydrodynamic and contact resistance under applied stress, especially at higher ϕ [33,41]. Soft particles, such as microgels [42-44] and colloidal star polymers [45], do not jam unless packed to much higher volume fractions ($\phi_J \rightarrow 1$) because of their ability to deform or interpenetrate. Just as in the case of hard spheres, their dynamical arrest and rheological properties are highly dependent on the distance of ϕ from ϕ_J.

A number of experimental challenges persist in obtaining a physically accurate value of $<z>$ even with hard sphere-like colloids. Conventionally, the contact distance is approximated as the primary minimum in the radial distribution function, $g(r)$ [46]. This is done to account for uncertainties in the average particle-to-particle separation distance, which come from a few sources: (a) sterically-stabilized particles tend to have surface-grafted polymer brushes, which can adopt different conformations depending on the grafting density and the polymer-solvent interactions [47] (Figure 2.1), (b) incomplete screening of the electrostatic repulsion gives rise to a finite Debye screening length, and (c) most particles are polydisperse in size and surface roughness. The effect of the contact distance in characterizing load-bearing colloidal packings has been previously discussed in literature [48,49]. Due to the importance of contact microstructure in particulate micromechanics, setting a contact criterion to establish an accurate value of $<z>$ near jamming is critical. Some of the earlier works to establish a contact criterion in experimental systems include the use of black japan paint marks for packing of ball bearings [50] and interfacial fluorescent dyes in an emulsion system [51]. These methods tend to be time consuming and possess challenging surface chemistry modification in the case of experimental hard sphere colloids, which are used as model systems for studying colloidal phase behavior and rheology.

We report a method to extract the contact criterion from microscopy images of hard sphere-like smooth and rough colloids suspended in a refractive index-matched solvent at $\phi > 0.10$. The poly(methyl methacrylate) (PMMA) colloids are fluorescent and sterically stabilized with a grafted layer of poly(12-hydroxystearic acid) (PHSA).[52,53] They are packed to a jammed state, $\phi_{J,}$ by high speed centrifugation, then diluted subsequently and imaged with a confocal laser scanning microscope (CLSM). The resultant suspension microstructures are compared to liquid state theory. Finally, we obtain the contact search distance by considering the physical length scales between two neighboring particles and comparing our results with the simulation data of Silbert for particles with varying pairwise friction coefficient, μ_p [54].

2.2 Materials and Methods

2.2.1 Synthesis and characterization of PHSA comb copolymer as the steric stabilizer

All chemicals were purchased from Sigma-Aldrich and used without further purification unless specified. Smooth and rough colloids were synthesized *via* free-radical dispersion polymerization using the PHSA comb copolymer stabilizer synthesized in our lab. The PHSA stabilizer was synthesized using a standard three-step synthesis process [52] (Figure 2.2a): first, the polycondensation of 12-hydroxystearic acid (12-HSA, 80% purity from TCI Chemicals) into PHSA in the solvent toluene, using the catalyst p-toluenesulfonic acid at temperature of 150°C over a period of 20-22 hours; second, the synthesis of PHSA-glycidyl methacrylate (PHSA-GMA) brushes in toluene at 150°C for 7 hours; finally, the free-radical polymerization of PHSA-GMA using the heat-activated initiator 2-azobisisobutyronitrile (AIBN) and the monomer methyl methacrylate (MMA) in a 2:1 wt % mixture of ethyl acetate and butyl acetate at 110°C for 9.5 hours to produce PHS-GMA-MMA block copolymer brushes. Both GMA and MMA were used after removing the trace amount of stabilizing inhibitors by passing them through an inhibitor removal column, purchased from Sigma-Aldrich. The average number of monomer per chain of the PHSA-GMA brushes was characterized using nuclear magnetic resonance (NMR) spectroscopy (Bruker NEO 400 MHz). Deuterated chloroform ($CDCl_3$) was used as the solvent for the NMR measurements.

The length of the brush chain on the particles is linearly related to the number of monomer units per chain (*n*) in the PHSA-GMA intermediate from PHSA stabilizer synthesis. Here, we utilized two methods to characterize the value of *n*. First, we performed ^{1}H-NMR on the monomer 12-HSA and the intermediate product PHSA-GMA. The intensity spectra was normalized by the background solvent intensity ($CDCl_3$). This method utilizes the change in peak signals for corresponding chemical shifts (δ) of the respective proton. In our case, these are hydrogen atoms in the unreacted carbon atom (δ ~ 3.6 ppm) and the newly formed ester (δ ~ 4.8 ppm) in the 12-HSA and PHSA-GMA. As the polycondensation reaction proceeds, the former peak decreases while the later peak increases, as shown in Figure 2.2b**.** The average number of monomer units per chain ($\overline{x_n}$) was computed by integration of the peaks corresponding to the ester and alcohol groups using the formula [53]:

$$\overline{x}_n = \frac{1}{\frac{n_{OH}}{n_{ester}} + \frac{1}{r} - 1} + 1 \tag{2.1}$$

Here, n_{OH} and n_{ester} correspond to the number of alcohol and ester groups present in the PHSA-GMA adduct. We obtained the ratio n_{ester}/n_{OH} = 10.73 by integrating the intensities at their peaks, and estimated the initial monomer purity, *r*, as 0.8975. Value of *r* for 80% pure 12-HSA used in our synthesis was linearly interpolated from *r*-monomer purity data reported in Palangetic et al. Substituting n_{ester}/n_{OH} and *r* into equation (1) shows that $\overline{x_n}$ = 5.586. To independently verify the number of monomer units per PHSA copolymer chain, we estimated the number of acid groups by titrating the PHSA adduct against 0.01 M potassium hydroxide (KOH) solution, and found that the average number average molecular weight was $\overline{M_n}$ = 1668 g/mol and $\overline{x_n}$ = 5.551. Previous studies reported that a length of 5-6 monomer units in PHSA is equivalent to a stabilizer brush length of 10-15 nm [55]. Unlike the previous work (95% purity)[53], we showed that PHSA stabilizer can be synthesized from a lower grade (80% purity) 12-HSA monomer.

2.2.2 Synthesis and characterization of smooth and rough colloids

PMMA colloids were synthesized using the PHSA comb copolymer as the steric stabilizer (Figure 2.2c). For smooth colloids, 1.8 g of PHSA stabilizer was added into a 250 ml three-necked reaction flask containing 2:1 wt/wt% solvent mixture of hexane and dodecane. The mixture was stirred while increasing the temperature to 80°C to maintain reflux. Then, a mixture of 0.2775 g AIBN, 34 g MMA, 230 µl 1-octanethiol, and 660 µl methacrylic acid was added to the flask. Nucleation commenced four to eight minutes after the addition of the monomer solution, determined as the time at which the clear solution began to turn cloudy. Rough PHSA-*g*-PMMA colloids were synthesized in the same manner as the smooth colloids, but with the addition of the crosslinker ethylene glycol dimethacrylate, EGDM, (EGDM/PHSA = 1.4 wt/wt%) at a rate of 360 µl/min after nucleation commenced. All colloids were fluorescently dyed with Nile Red to allow visualization during CLSM measurements. After two hours of reaction, the reaction flask was cooled to room temperature. Particles formed in the reaction flask were cleaned with pure hexane for a minimum of six times by centrifugation at 10,000 rpm for 15 minutes. The clean particles were stored in hexane until further use. A field emission scanning electron microscope (FEI Verios 460L) was used to image the samples, which were deposited on a silicon substrate and sputter coated with 8-9 nm of Au/Pd. The micrographs in Figure 2.3a show that the smooth colloids are of particle diameters $2a_{SEM}$ = 1.45 µm ± 4%, while the rough colloids are of effective particle diameters $2a_{eff,SEM}$ = 1.43 µm ± 8%. These particle diameters are reported for dry particles, which undergo swelling when suspended in solvents. Atomic force microscopy (AFM) (Asylum MFP-3D) was used to qualitatively illustrate the difference in surface roughness profiles (Figure 2.3b) using a silicone cantilever tip (force constant = 5 N/m, resonant frequency = 150 kHz and tip radius < 10 nm) in tapping mode.

2.2.3 Preparation of colloidal suspensions

Dense colloidal suspensions were prepared by performing a solvent transfer of the PMMA particles into squalene (viscosity η = 12 cP at 25°C). Particles are charge neutral in this solvent and exhibit hard sphere-like behavior. The solvent is refractive index-matched with the particles (refractive index $n_{\mathrm{PMMA}} = 1.49$ and $n_{\mathrm{squalene}} = 1.49$), which reduces scattering in 3D CLSM and minimizes the van der Waals attractions between the colloids. There is a density mismatch of $\Delta\rho = 0.322$ g/cm^3 between the particles and the solvent (density $\rho_{\mathrm{PMMA}} = 1.18$ g/cm^3 and $\rho_{\mathrm{squalene}} = 0.858$ g/cm^3). The density mismatch was used to generate colloidal suspensions at maximum packing by centrifuging the suspensions at high speeds until the particles completely settled to the bottom of the centrifuge tubes [56]. It should be noted that our protocol shifts the maximum random close packing (ϕ_{RCP}) to a lower shear-jammed value (ϕ_{J}), which is process- and μ_{P}-dependent [57-59]. The Péclet number for sedimentation, $Pe_g = 4\pi a^4\Delta\rho g/3k_BT$, is a dimensionless number that defines the ratio of the sedimentation rate to the rate of Brownian motion. Centrifugation was performed at $Pe_g = 1400$ to avoid crystallization of the monodisperse colloids.[60] After removal of excess solvent, the compacted samples were diluted from ϕ_{J} by gradual addition of known small volumes of squalene. Diluted suspensions were tumbled in vials at 3 rpm for a minimum of one week to achieve even re-dispersion. For smooth colloids, the volume fraction $\phi_{dilution}$ was computed from the ratio of $\phi_{dilution} = V_p/(V_p+V_s')$, where $V_s' = V_s+V'$. Here, V_P and V_S are the volume of particles and solvent at known ϕ_{J} calculated from mass balance, and V' is the additional volume of solvent added for dilution from ϕ_{J}.. This method was used to generate suspensions of smooth and rough colloids with $0.1 \leq \phi \leq \phi_{\mathrm{J}}$.

2.2.4 CLSM imaging and image processing

A high speed CLSM (Leica SP8) equipped with a resonant scanner was used to visualize the 3D microstructure of smooth and rough colloidal suspensions. The diluted suspensions were transferred to glass vials with an attached coverslip with dimensions of 40 mm × 24 mm and a thickness of 0.21 ± 0.04 mm for imaging. Images were obtained at ≥ 15 µm above the bottom cover slip to avoid wall-induced crystallization effects. The dimensions of the image volume (V_{box}) were 30.72 µm × 30.72 µm × 15 µm, with a voxel size of 0.06 µm × 0.06 µm × 0.06 µm. Imaging was performed at three independent locations within the same sample. Each image volume was captured in 8-10 s, which is much shorter than the Brownian diffusions time scales (τ_B) as defined by the Stokes-Einstein-Sutherland diffusivity ($\tau_B = 6\pi\eta a_{eff}^3/k_BT$; $\tau_{B,smooth} = 29$ s and $\tau_{B,rough} = 20$ s). This ensures that the inherent Brownian motion of these microspheres does not significantly affect centroid identification in image processing. A minimum of 3000 particles per image volume was used to generate sufficient statistics for structural characterization.

Particles positions in 3D were obtained by a standard imaging algorithm in which the brightest weight-corrected pixels correspond to particle centroids [61]. Raw images and corresponding centroid-picked images for smooth and rough particles are shown in Figure 2.4. The $g(r)$ was obtained by computing the density-normalized probability of finding particles around a reference centroid. The volume fraction was directly obtained from the images using the relation, $\phi_{CLSM} = (4/3)\pi a_{eff}^3 N_p/V_{box}$, where N_p is the total number of particles found in the image volume V_{box}. The value of ϕ_{CLSM} and $\phi_{dilution}$ are in agreement as shown in Figure 2.5a. The direct imaging method combined with a dilution factor is critical in the estimation of ϕ for rough colloids where ϕ_J is unknown, because of difficulties with sample handling near ϕ_J. This analysis showed that $\phi_J = 0.64$ for the smooth colloids, while $\phi_J = 0.56$ for the rough colloids. For a smooth hard sphere system with 4% size polydispersity, simulations show that the maximum close packing ϕ_{RCP} has been shown to lie between 0.64 and 0.66 [62-64]. Experiments on the effect of particle polydispersity and shape was characterized earlier using higher moments of $2a$, namely skewness and kurtosis, and ϕ_{RCP} was found to be in between 0.63-0.69 [65]. Due to the shear-jamming nature of the high Pe_g centrifugation method, both smooth and rough colloids jam below ϕ_{RCP}. In case of smooth PMMA particles, we do not observe a significant shift from simulated/theoretically predicted ϕ_{RCP} despite the soft repulsive nature of the grafted polymers. The contact number distribution p(z) and the mean contact number <z> were obtained from microstructural data by averaging the number of particles around a reference centroid as a function of the search distance, $r' = r/2a_{eff}$, where r' ranges from 1 to 1.1.

PMMA colloids swell in certain solvents [66] and in our samples we observe that the particle diameters increase by 1-12% when suspended in squalene. Thus, using the dry particle sizes obtained from SEM results in underestimation of the suspension volume fraction by 28% for smooth particles, and by 4% for rough particles. To obtain the swollen particle diameter of smooth and rough colloids in squalene, we obtained 2D images of the bottom-most monolayer of sediment particles in glass vials, where the z-plane is adjusted to match the centers of most of the particles. Because $\phi \sim a^3$ and therefore $\Delta\phi \sim 3\phi\Delta a$, we paid special attention to the measurement of the effective particle diameter for the rough colloids [67]. In this study, we considered the surface-to-surface distance of rough colloids, which provides a value of $2a_{eff}$ that minimizes the deviation of the surface roughness as shown in Figure 2.5b. The swollen diameters of the smooth and rough colloids were $2a_{smooth}$ = 1.61 μm ± 4% and $2a_{eff,rough}$ = 1.44 μm ± 5%. The difference in the swelling between smooth and rough colloids are likely due to the presence of crosslinker in the rough microspheres [66].

2.3 Results and Discussion

2.3.1 Radial distribution function

The suspension microstructures of smooth and rough colloids in squalene are quantified in Figure 2.6. The experimentally measured *g*(*r*) of the dense suspensions are plotted alongside predictions from the Ornstein-Zernicke integral equation of state [68]:

$$h(r) = c(r) + \rho \int c(|r - r'|\, h(r')).dr' \tag{2.2}$$

Here, $g(r) = h(r)+1$, where *h*(*r*) represents the correlation function that takes into account the direct contribution from two-body interactions and the indirect contribution from multi-body interactions. Equation (2.2) produces an analytical solution for the *g*(*r*) when the Percus-Yevick closure for hard spheres is used [69] in which $g(r) = 0$ for $r < 2a$ and $c(r) = 0$ for $r > 2a$:

$$g(r) = 1 + c(r) + \frac{4\pi}{(2\pi)^3} \int_0^1 k^2 \sin(kx) \frac{c(k)}{kx} \left[\frac{\phi \frac{6}{\pi} c(k)}{1 - \phi \frac{6}{\pi} c(k)} \right] dk \tag{2.3}$$

The excellent agreement between the theoretical and experimental *g*(*r*) in Figure 2.6 shows that both smooth and rough colloids exhibit hard sphere-like behavior. Additionally, the absence of regularly spaced, sharp peaks in the *g*(*r*) shows that the suspensions remain disordered and non-crystalline in our experimental timescales.

In Figure 2.6, there is a discrepancy in the first *g*(*r*) maxima and minima between the experimental data and theoretical predictions for both smooth and rough colloids when $\phi > 0.50$. We hypothesize that this mismatch is due to the sensitivity of the image processing algorithm to size polydispersity in suspensions at higher concentrations, which has been reported previously in literature for $\phi > 0.26$ [70]. Our experimental *g*(*r*) are similar to that obtained by Mason and coworkers, who investigated the structure of polydisperse emulsions through experiments and

Brownian Dynamics simulations [71]. To verify that the variation in our case does not undercount N_p and the mean contacts, we apply a similar concept from atomic liquids where the the total number of particles in the first coordination shell, *N*, is computed using the integral, $\int_0^{\infty} 4\pi r^2 \rho g(r) dr \approx N$ where ρ is the number density of particles. Specifically, *N* particles fill the volume around the first coordination shell as defined by the primary minimum ($r_{\min}$) of $g(r)$. Since colloids are thought to be "model atoms", *N* was conventionally used to obtain the mean contact number [72-75]. While the concept of coordination number is useful in describing the structure of dense liquid phase [76], it is not the same as the number of direct particle-particle contacts, which is required to establish the contact criterion required for mechanical stability. Nonetheless, we know that *N* from both experimental and theoretical $g(r)$ for the same ϕ should match. We use this idea to comment on the accuracy of our experimental $g(r)$. We estimate *N* by discretizing the above integral as $\sum_{r=0}^{r_{\min}} g(r_i) r_i^2 \Delta r$, where Δr is the binned intervals of the discretized $g(r)$. For a smooth suspension of $\phi = 0.57$, we obtain *N* as 10.8 and 11.9, from experimental and theoretical $g(r)$, respectively. The small differences may be due to bin-size sensitivity in discretizing the integration and approximation of the integral as $\int_0^{r_{\min}} 4\pi r^2 \rho g(r) dr = N - 1 \approx N$. We conclude that even though our image processing is sensitive to polydispersity at higher ϕ, the algorithm does not undercount N_p in the 3D image volumes.

2.3.2 Physical rationale of the contact cutoff distance and verification with simulations

We define r' as the additional length scale beyond that of the swollen particle diameter that determines contact between two particles. It is obtained by propagating the uncertainties introduced by size polydispersity, the length of the PHSA steric layer on particle surfaces, and the average length scale of the asperities present on the rough colloids. We first discuss the results obtained from using this contact criterion on dense suspensions of smooth colloids. The true swollen particle diameter is given as $2a_{true} = 2(a+l)$, where l is the length of PHSA brush. Uncertainty propagation in particle size estimation is given by $\Delta 2a_{true} = [(\Delta 2a)^2+(\Delta l)^2]^{1/2}$. Since $2a = 1.62$ µm for the smooth colloids, combining the uncertainty from particle polydispersity (± 0.06 µm) and the uncertainty from PHSA brush length measurements from the literature for 5-6 monomer units (± 6 nm) [55,77-79] yields a total uncertainty of 4%. This method suggests that a value of $r' = 1.04$ defines contact between smooth colloids. The uncertainty in $2a_{eff}$ for rough colloids includes the added length scale from the surface bumps, which is also inherent in the size polydispersity due to the method with which we obtained particle diameters. The rough colloids have a size polydispersity of ± 0.07 µm. Here, we do not use the roughness length scale or the interparticle friction for this set of particles. As in the case of smooth colloids, addition of the uncertainty from PHSA brush length yields an overall size uncertainty of 5%. This establishes the contact criterion as $r' = 1.05$ for the rough colloids.

To verify that these values of r' represent the correct contact physics found in dense colloidal suspensions, we first obtain $\langle z \rangle$ of all suspensions generated with different r' values. Then, we extrapolate $\langle z \rangle$ to ϕ_J using and empirical fit and compare the mean contact numner at the shear jammed condition with simulated $\langle z \rangle_J$ values for frictionless and frictional spheres in the absence of solvent hydrodynamics [54]. Mechanical isostaticity, which controls the jammed state at RCP, dictates that $<z>_{\mathrm{RCP}} = 6$ for smooth or frictionless particles. Our smooth particles can be assumed as frictionless because we showed earlier that the experimentally calculated ϕ_{J} and the theoretically established ϕ_{RCP} are very close to each other. The concept of isostaticity at RCP justifies extrapolation of the data for smooth colloids to ϕ_{J}, where the experimental value of $<z>_{\mathrm{J}}$ is expected to be six. The benchmarking against predicted values of $<z>_{\mathrm{J}}$ for smooth (frictionless) and rough (frictional) colloids is used to generate an independent validation of the experimental contact criterion r'.

Surface anisotropy in the form of microscale bumps is thought to cause interlocking hindrance, which is a form of geometric friction caused by the inability of rough colloids to rotate freely in the solvent. This concept is supported by our earlier experimental observations that the rotational dynamics of rough colloids was far slower than that predicted by Stokesian Dynamics simulations [40]. We used this idea to determine if the physical rationale behind the value of of r' is correct by comparing the value of $<z>_{\mathrm{J}}$ obtained with different r' for smooth and rough colloids with the results from friction-dependent simulations of monodisperse granular spheres. The computer simulations of Silbert [54] probed the packing microstructure and force chains of a 3D packing of inelastic soft spheres that was first quenched by overcompression beyond jamming point, then brought back to the point of isostaticity by expanding the box and allowing $\phi \rightarrow \phi_{\mathrm{J}}$. The protocol was repeated with the addition of a Coulomb friction criterion between spheres. Silbert described two interesting observations: first, the value of ϕ_{J} decreased from 0.64 to 0.55 when the interparticle friction μ_p increased from 0.001 to 10; second, the distribution of contact stresses depended on μ_p and the history of the packing. Furthermore, the reduction in ϕ_{J} with the increased frictional constraint between particles was accompanied by a corresponding reduction in $<z>_{\mathrm{J}}$ from six to four, which we reproduce in Figure 2.7 for comparison against experimental data. Silbert's simulations showed that the correlation between $<z>_J$ and μ_p is nonlinear: at $\mu_p < 10^{-2}$, $<z>_J$ remains close to six while at $\mu_p > 1$, $<z>_J$ saturates near a value of four. We assume that our smooth colloids behave like frictionless spheres while the rough colloids in the shear jammed condition behave like frictional spheres. Previous experimental studies have shown that changing the surface roughness of colloids caused changes in $\mu_{p.}$ We did not perform lateral force microscopy to measure the sliding friction between particles, so we do not know the exact value of μ_p for the rough particles used in this study.

2.3.3 Sensitivity analysis of contact distance criterion

Figure 2.8 demonstrates the sensitivity of $<z>$ to the choice of r'. For example, arbitrarily choosing a large value of $r' = 1.1$ means that all neighboring particles within 10% of the reference particle diameter are in contact. This contact criterion significantly overestimates the contact number at ϕ_J by generating values of $<z>_J \approx 8.0$ and $<z>_J \approx 6.4$ for smooth and rough colloids respectively. Instead, we use the estimated contact criterion of $r' = 1.04$ for smooth colloids and find that $<z>_J \approx 5.5$, much closer to the expected isostatic criterion ($z_{\mathrm{iso}} = 6$) for frictionless spheres. Using $r' = 1.06$ causes a slight overestimation of the contact number at jamming, $<z>_J \approx 6.3$. The limits of the contact criterion for the smooth colloids is therefore $1.04 < r' < 1.06$. Applying the same analysis to suspensions of rough colloids ($1.05 \leq r' \leq 1.07$) produces $4 \leq <z>_J \leq 4.8$ and validates the choice of $r' = 1.05$ from the uncertainty analysis on cutoff distance.

Figure 2.9 shows how p(z) varies with r' in suspensions of smooth ($r' = 1.04$ and 1.06) and rough ($r' = 1.05$ and 1.07) colloids. The difference in p(z) are relatively minor at small ϕ but becomes rather significant in dense suspensions with larger values of ϕ. As expected, the p(z)

plots for smooth colloids show that increasing ϕ causes <z> to shift towards higher values while the spread remains relatively constant except at $\phi = 0.20$ (Figure 2.9a and 2.9c). The inset of these figures show that <z> increases from 0 to 6 as ϕ approaches 0.64. Similarly in the case of rough colloids, <z> increases with increasing ϕ (Figure 2.9b and 2.9d). At ϕ_J, changing the contact criterion for rough colloids increases $<z>_J$ from 4 ($r' = 1.05$) to 4.9 ($r' = 1.07$). The exact isostatic condition of the particle depends on its μ_P.

The sensitivity of $<z>_J$ to r' is shown in Figure 2.10**.** Both smooth and rough colloids show a linear relation of $<z>_J$ to r' with a small slope. As r' increases from 1.04 to 1.06 for smooth colloids, $<z>_J$ increases from 5.5 ± 0.7 to 6.3 ± 0.7. Similarly, as r' increases from 1.05 to 1.07 for rough colloids, $<z>_J$ increases from 4.0 ± 0.9 to 4.9 ± 0.9. The uncertainty in $<z>_J$ values shown in Figure 2.10 are not from experimental errors but are from the error propagation estimated in the nonlinear fits that were used to extrapolate <z> at various ϕ to the shear jammed states. The contact criterion of $r' = 1.04$ as established by our method shows that $<z>_J \approx 6$ for smooth colloids to within error limits. It is possible to further narrow down the contact criterion to $r' = 1.052$, where $<z>_J = 6 \pm 0.7$, pointing to the contact criterion that is applicable to the ideal isostatic condition, where $\phi_J \approx \phi_{RCP}$ and $<z>_J \approx z_{iso}$. Furthermore, without the need to explicitly measure surface roughness or interparticle friction, the method shows that $4.0 \leq <z>_J \leq 4.9$ in the contact search window $1.05 \leq r' \leq 1.07$ for the rough colloids. Various literature studies involving theory and simulations predict a similar window of contact where $4 < z_{RCP} < 4.5$ for frictional particles at $\phi_J = 0.56$ [80-83] in support of the validity our contact criterion within the error limits. Compared to smooth colloids, we are unable to narrow down a single value of the contact distance for which we require prior knowledge of isostatic condition of the particle, which in turn depends on its μ_P. Nonetheless, we have provided a window of the contact criterion for rough hard sphere colloids where the mean number of particle-particle contacts at jamming is within error limits as predicted by theory and simulations.

2.4 Conclusions

The sensitivity analyses in Figures 2.8, 2.9, and 2.10 demonstrate that a physically relevant search distance is needed to quantify the contact microstructure of dense colloidal suspensions. Picking a value of r' that deviates by just 1% of the particle diameter results in a change in <z> by up to 10% of the true value. This effect is exacerbated in dense suspensions ($\phi > 0.50$) because of the increased number of nearest neighbors around a reference centroid. In fact, our results show that the conventional practice of using the first minimum in $g(r)$ is inappropriate because using such a large search distance drastically overestimates <z>. Rather, we recommend performing a simple uncertainty analysis that accounts for the size polydispersity, steric brush length, and surface roughness of the colloids. Summing the physical length scales with the swollen particle radius generates a search criterion which varies between $r' = 1.04$ and $r' = 1.07$ for both smooth and rough colloids. To prepare the samples in this paper, sterically stabilized PHSA-g-PMMA colloids are packed to ϕ_J using a shear jamming protocol in a high speed centrifuge at Pe >> 1, which avoids crystallization of the monodisperse particles over experimental time scales while shifting ϕ_J to values below ϕ_{RCP}.

The method we developed here can be used to find an appropriate contact search distance for spherically-symmetric particles with surface roughness, without requiring prior knowledge of ϕ_{RCP} and μ_p. History-dependent effects could be important when approaching or departing from the shear jammed point, especially for frictional particles. The established procedure could potentially be extrapolated to other types of particulate systems where electrostatic interactions play a role, or in predicting the jamming threshold for biological systems and geological soils [84,85].

Acknowledgements. The authors thank Dr. Alan Jacob, Prof. Karen Daniels, and Prof. Eric Weeks for advice and discussion. We acknowledge the Analytical Instrumentation Facility (AIF) at NC State University for SEM and AFM facilities. This work is supported in part by the National Science Foundation (NSF CBET-1804462), the American Chemical Society Petroleum Research Fund (#59208-DNI9), and North Carolina State University startup funds.

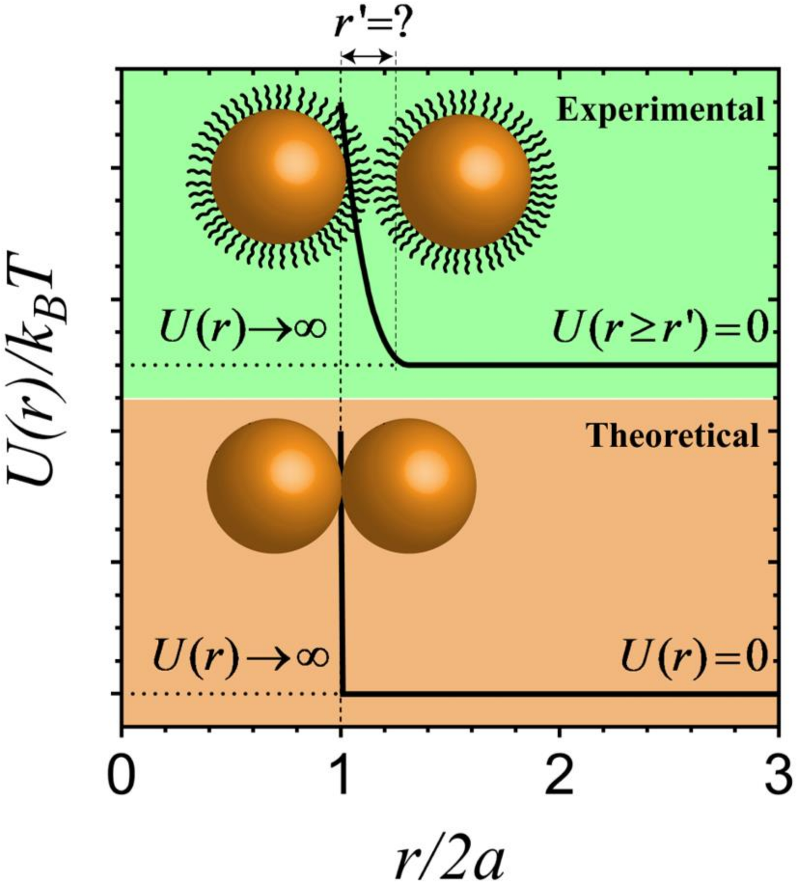

Figure 2.1 | When do experimental colloidal systems contact? Differences in the pairwise interaction potential between theoretical and experimental hard-sphere systems. The experimental system consists of poly(methyl methacrylate) colloids sterically stabilized with a thin layer of poly(12-hydroxystearic acid).

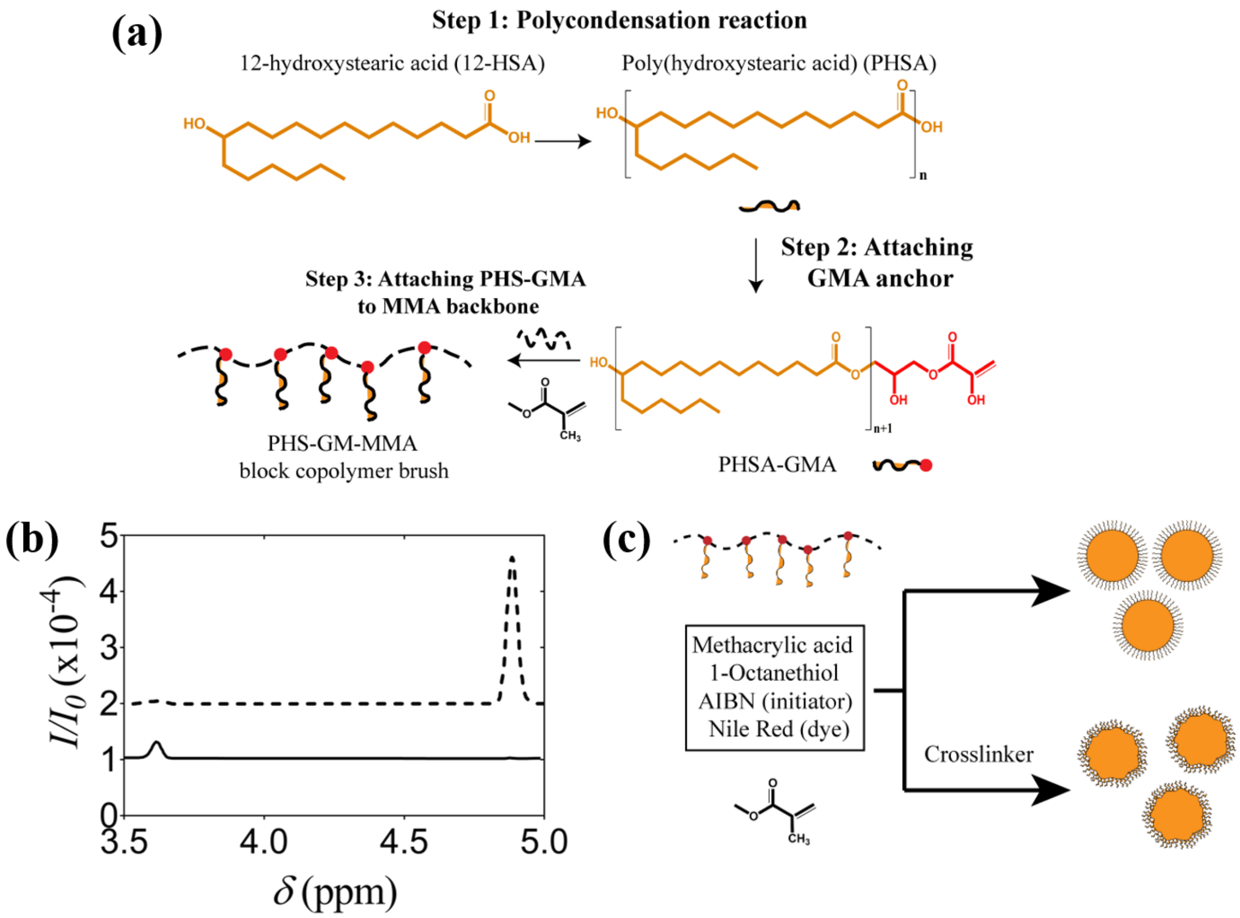

Figure 2.2 | Steric polymer brush synthesis chemistry. (a) Chemical reaction scheme for the PHSA stabilizer. (b) ^{1}H-NMR spectra for 12-HSA (bold line) and PHS-GMA (dashed line) with chemical shift as a function of normalized intensity with respect to the reference standard, d-CHCl$_3$. (c) Overview of the synthesis protocol for PHSA-g-PMMA smooth and rough colloids.

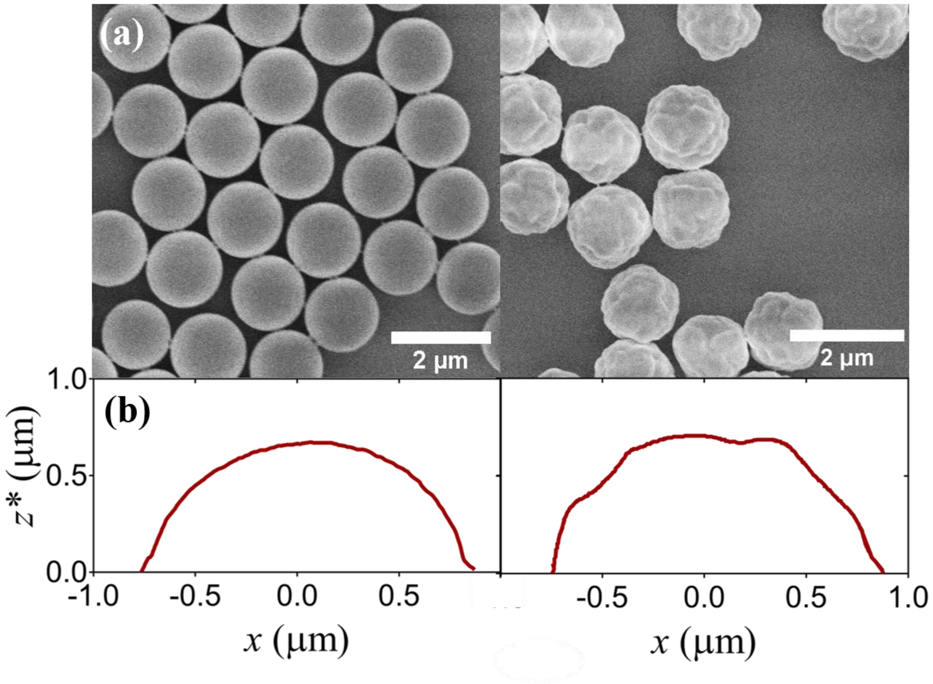

Figure 2.3 | Characterization of the colloid morphology. (a) SEM micrographs and (b) 2D AFM surface profiles for smooth (left) and rough (right) colloids. The profiles are taken at close to the center plane of the colloids. In (b), *z** refers to regions that are not limited by the AFM cantilever geometry.

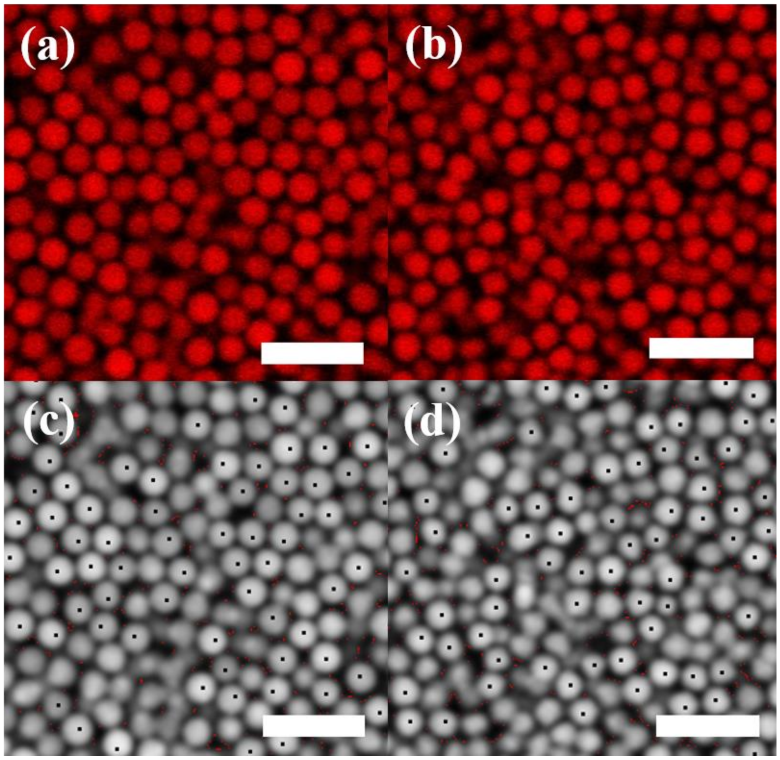

Figure 2.4 | Confocal microscopy and image-processing. (a,b) Representative raw CLSM images and (c,d) processed images where black dots indicate centroid positions in a fixed plane. (a, c) Dense suspension of smooth colloids at ϕ = 0.61, (b, d) dense suspension of rough colloids at ϕ = 0.54. Scales bars = 5 μm.

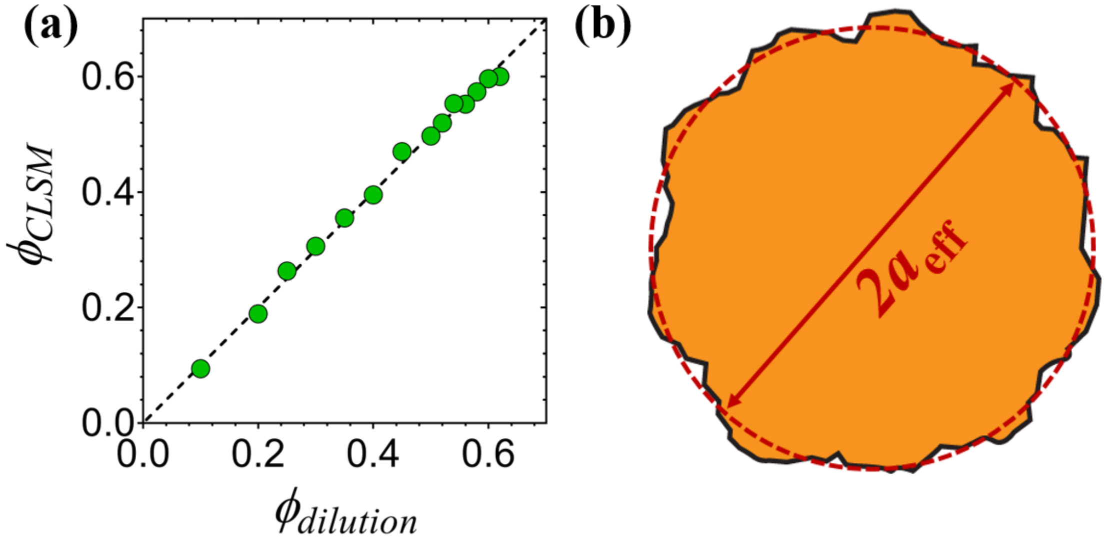

Figure 2.5 | Validation of suspension preparation methodology (a) Comparison of the colloid volume fraction using two methods: high speed centrifugation to a shear jammed packing followed by subsequent dilutions, and directly counting number of particles from CLSM. (b) Method to extract the effective diameter and volume fraction of rough colloids.

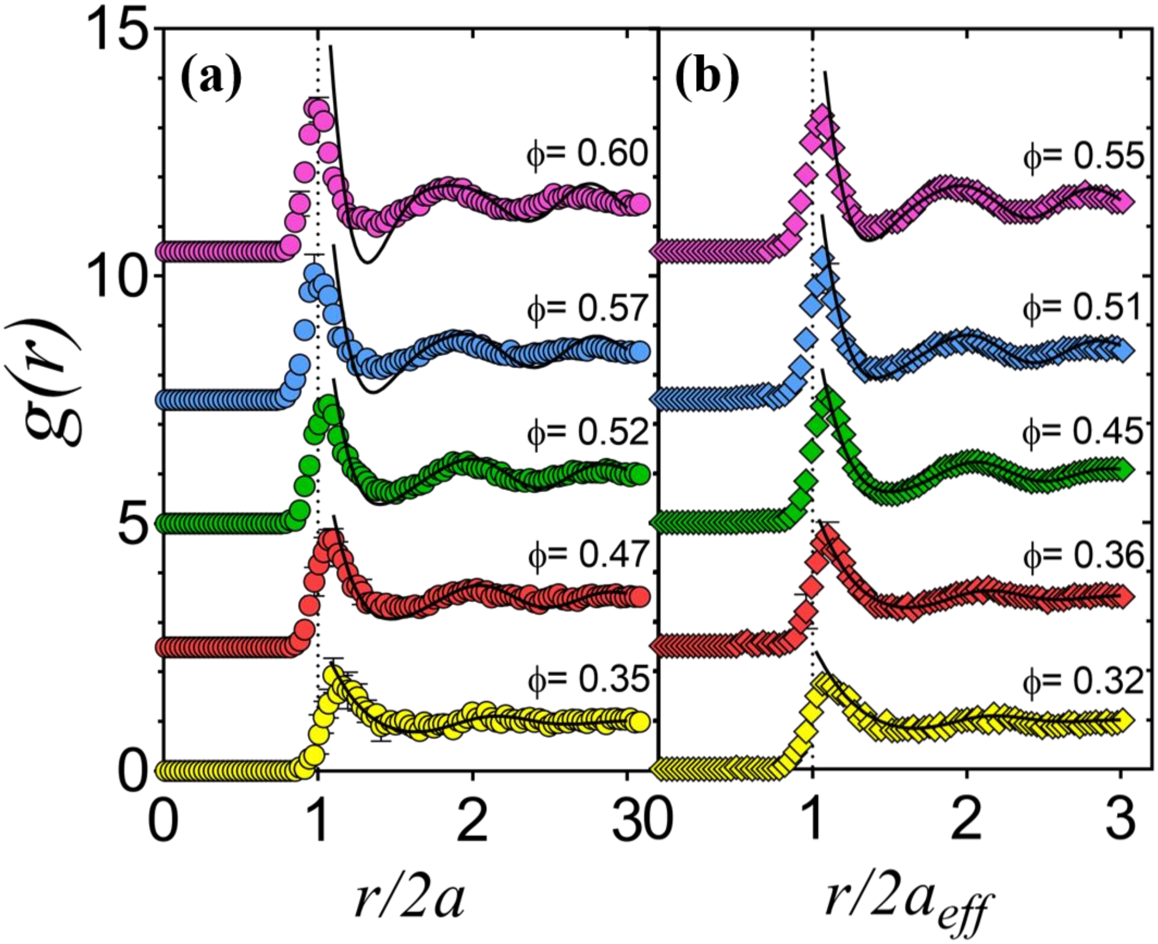

Figure 2.6 | Radial distributions show hard sphere microstructure. Radial distribution functions of (a) smooth and (b) rough colloids. Filled circles represent experimental values and solid black lines represent the theoretical fits from the Ornstein-Zernicke solutions. In (a), the *g*(*r*) data set are plotted for smooth colloids at ϕ = 0.35 (yellow), ϕ = 0.47 (red), ϕ = 0.52 (green), ϕ = 0.57 (blue), and ϕ = 0.60 (pink). In (b), the *g*(*r*) data set are plotted for rough colloids at ϕ = 0.32 (yellow), ϕ = 0.36 (red), ϕ = 0.45 (blue), ϕ = 0.51 (red), and ϕ = 0.55 (pink).

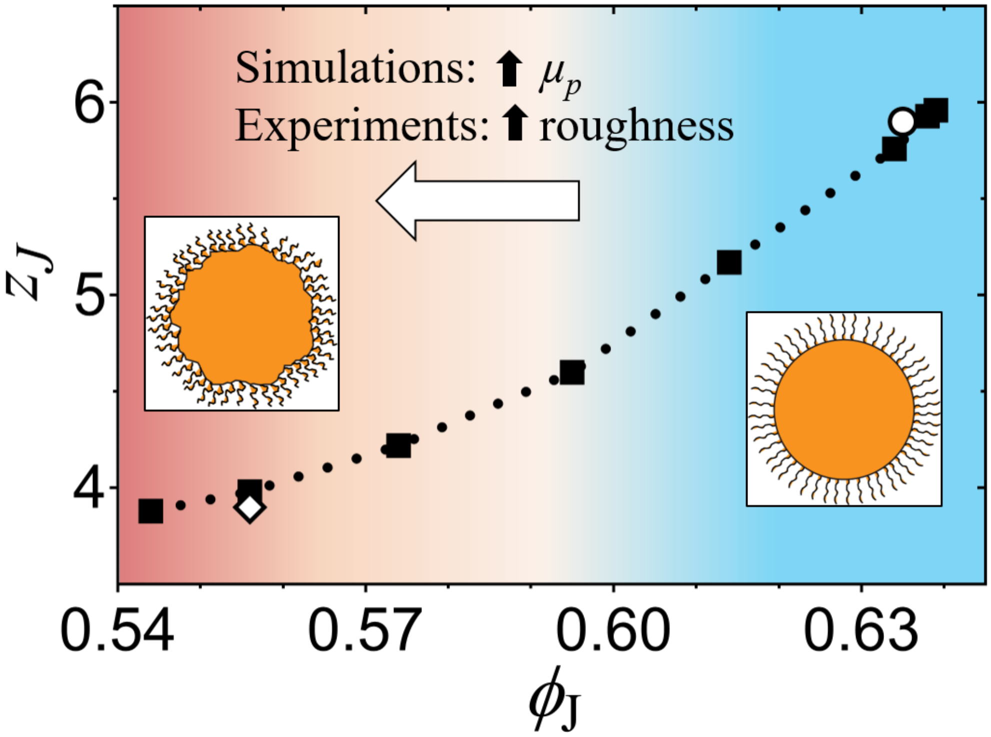

Figure 2.7 | Comparing experimental jamming contact with simulation data. The contact number at jamming plotted against the volume fraction at jamming, which is a function of the interparticle friction. Filled squares are data adapted from simulations of Silbert.[54] A dotted line is drawn to guide the eye. Open symbols represent experimental data for smooth (circle) and rough (diamond) colloids. The experimental z_J values are obtained by using r' = 1.04 for smooth colloids and r' = 1.05 for rough colloids. Color gradient indicates transition from frictionless (red) to infinite friction (blue) regime. Inset: Sketch of smooth and rough PMMA particles with PHSA brushes for illustration purposes.

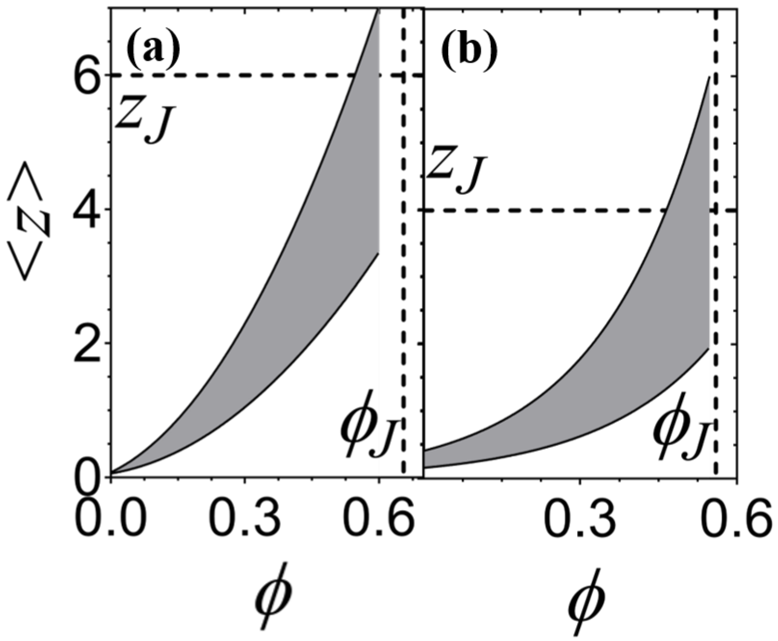

Figure 2.8 | Mean contact number as a function of contact search distances. Plot of the mean contact number as a function of ϕ for (a) smooth and (b) rough colloids. Shaded regions indicate a range of <z> values for different search distances used. The upper limit is for *r'* = 1.1 and the lower limit is for *r'* = 1.0. Dashed lines indicate predictions for isostatic packings of (a) frictionless and (b) frictional particles adapted from ref. 46. (Silbert, 2010).

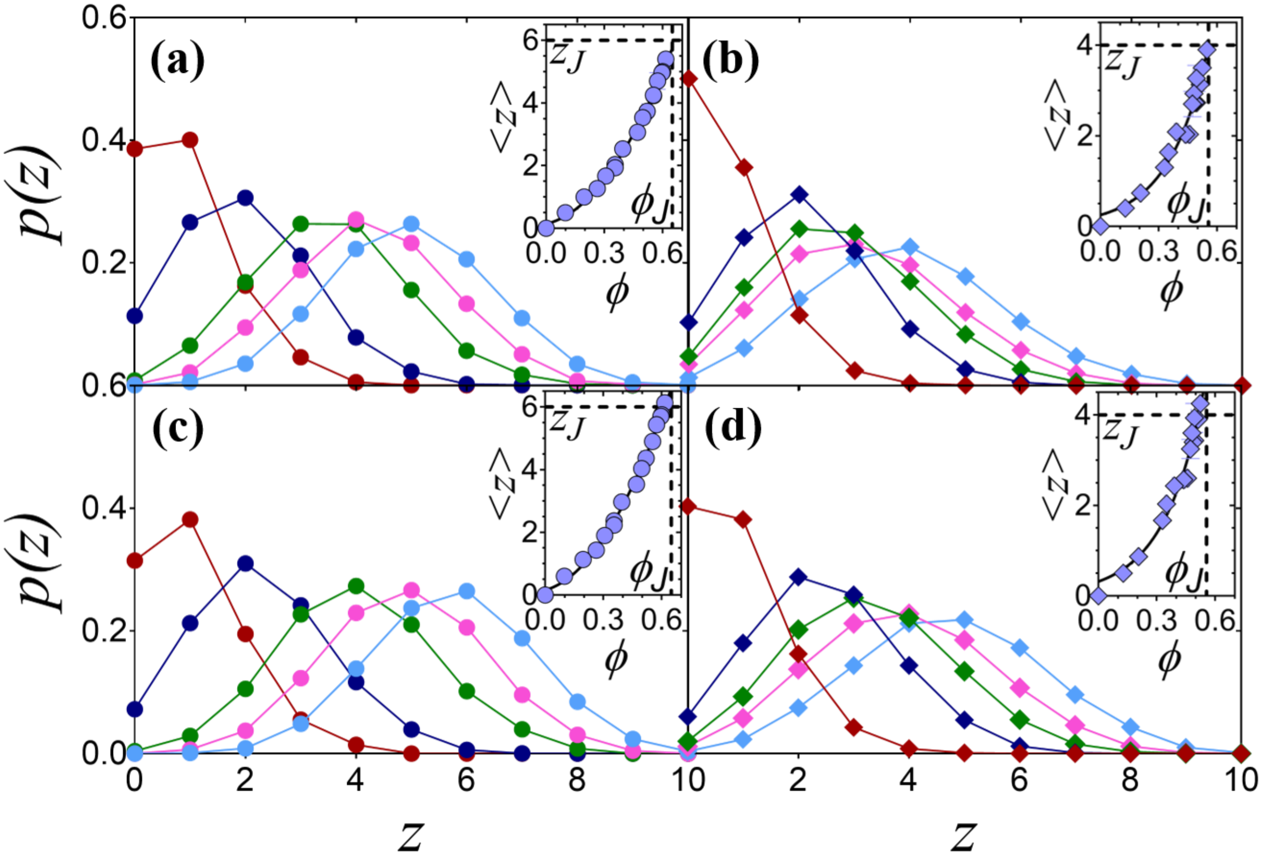

Figure 2.9 | Contact number distributions for dense suspensions. (a, c) Contact number distributions for smooth colloids obtained by setting (a) $r' = 1.04$ and (c) $r' = 1.06$. (b, d) Contact number distributions for rough colloids obtained by setting (b) $r' = 1.05$ and (d) $r' = 1.07$. For smooth colloids, the data sets consist of suspensions at $\phi = 0.20$ (red), $\phi = 0.35$ (dark blue), $\phi = 0.50$ (green), $\phi = 0.55$ (pink), and $\phi = 0.60$ (aqua). For rough colloids, the data sets consist of suspensions at $\phi = 0.20$ (red), $\phi = 0.40$ (dark blue), $\phi = 0.47$ (green), $\phi = 0.52$ (pink), and $\phi = 0.55$ (aqua). Insets: Mean contact number of smooth colloids with (a) $r' = 1.04$ and (c) $r' = 1.06$ and rough colloids with (b) $r' = 1.05$ and (d) $r' = 1.07$.

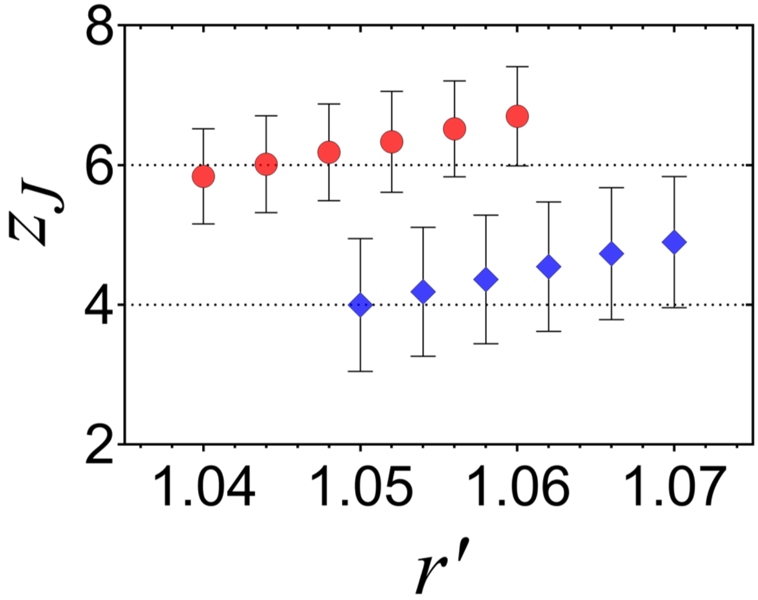

Figure 2.10 | Sensitivity analysis for contact criterion. Sensitivity analysis plot shows how z_J varies as a function of r' for smooth (red circles) and rough (blue diamonds) colloids at their respective extrapolated values of ϕ_J. Dotted lines represent isostatic conditions for frictionless ($z_J = 6$, $\mu_p = 0$) and frictional ($z_J = 4$, $\mu_p \rightarrow \infty$) particles.

References

[1] J. J. Stickel and R. L. Powell, Annual Review of Fluid Mechanics **37**, 129 (2005).

[2] M. van Hecke, Journal of Physics: Condensed Matter **22**, 033101 (2009).

[3] J.-A. Park *et al.*, Nat Mater **14**, 1040 (2015).

[4] J. M. Pastor *et al.*, Phys Rev E **92**, 062817 (2015).

[5] I. Zuriguel, A. Garcimartín, D. Maza, L. A. Pugnaloni, and J. M. Pastor, Phys Rev E **71**, 051303 (2005).

[6] A. J. Liu and S. R. Nagel, Nature **396**, 21 (1998).

[7] C. S. O'Hern, L. E. Silbert, A. J. Liu, and S. R. Nagel, Physical Review E **68**, 011306 (2003).

[8] M. E. Cates, J. P. Wittmer, J. P. Bouchaud, and P. Claudin, Physical Review Letters **81**, 1841 (1998).

[9] T. S. Majmudar and R. P. Behringer, Nature **435**, 1079 (2005).

[10] S. Henkes and B. Chakraborty, Phys Rev E **79**, 061301 (2009).

[11] J. E. Thomas, K. Ramola, A. Singh, R. Mari, J. F. Morris, and B. Chakraborty, Physical Review Letters **121**, 128002 (2018).

[12] R. Radhakrishnan, J. R. Royer, W. C. K. Poon, and J. Sun, Granular Matter **22**, 29 (2020).

[13] K. A. Whitaker, Z. Varga, L. C. Hsiao, M. J. Solomon, J. W. Swan, and E. M. Furst, Nature Communications **10**, 2237 (2019).

[14] R. N. Zia, B. J. Landrum, and W. B. Russel, Journal of Rheology **58**, 1121 (2014).

[15] S. Jamali, G. H. McKinley, and R. C. Armstrong, Phys Rev Lett **118**, 048003 (2017).

[16] A. Zaccone, H. Wu, and E. Del Gado, Phys Rev Lett **103**, 208301 (2009).

[17] L. C. Hsiao, H. Kang, K. H. Ahn, and M. J. Solomon, Soft Matter **10**, 9254 (2014).

[18] E. Moghimi, A. R. Jacob, and G. Petekidis, Soft Matter **13**, 7824 (2017).

[19] W. G. Ellenbroek, M. van Hecke, and W. van Saarloos, Phys Rev E **80**, 061307 (2009).

[20] E. Somfai, M. van Hecke, W. G. Ellenbroek, K. Shundyak, and W. van Saarloos, Phys Rev E **75**, 020301 (2007).

[21] M. Otsuki and H. Hayakawa, Phys Rev E **95**, 062902 (2017).

[22] F. Scheffold, F. Cardinaux, and T. G. Mason, Journal of Physics: Condensed Matter **25**, 502101 (2013).

[23] A. Donev, I. Cisse, D. Sachs, E. A. Variano, F. H. Stillinger, R. Connelly, S. Torquato, and P. M. Chaikin, Science **303**, 990 (2004).

[24] A. Baule and H. A. Makse, Soft Matter **10**, 4423 (2014).

[25] A. Boromand, A. Signoriello, F. Ye, C. S. O’Hern, and M. D. Shattuck, Phys Rev Lett **121**, 248003 (2018).

[26] M. Clusel, E. I. Corwin, A. O. N. Siemens, and J. Brujić, Nature **460**, 611 (2009).

[27] C. Zhang, C. B. O'Donovan, E. I. Corwin, F. Cardinaux, T. G. Mason, M. E. Möbius, and F. Scheffold, Physical Review E **91**, 032302 (2015).

[28] T. G. Mason, J. Bibette, and D. A. Weitz, Physical Review Letters **75**, 2051 (1995).

[29] T. G. Mason, M.-D. Lacasse, G. S. Grest, D. Levine, J. Bibette, and D. A. Weitz, Physical Review E **56**, 3150 (1997).

[30] J. Mewis and N. J. Wagner, *Colloidal Suspension Rheology* (Cambridge University Press, Cambridge, 2011), Cambridge Series in Chemical Engineering.

[31] J. F. Brady, Journal of Fluid Mechanics **272**, 109 (1994).

[32] R. J. Phillips, J. F. Brady, and G. Bossis, The Physics of Fluids **31**, 3473 (1988).

[33] L. C. Hsiao and S. Pradeep, Current Opinion in Colloid & Interface Science **43**, 94 (2019).

[34] M. Jerkins, M. Schröter, H. L. Swinney, T. J. Senden, M. Saadatfar, and T. Aste, Physical Review Letters **101**, 018301 (2008).

[35] R. A. Lionberger and W. B. Russel, Journal of Rheology **38**, 1885 (1994).

[36] T. Shikata and D. S. Pearson, Journal of Rheology **38**, 601 (1994).

[37] J. F. Brady, The Journal of Chemical Physics **99**, 567 (1993).

[38] B. M. Guy, M. Hermes, and W. C. K. Poon, Physical Review Letters **115**, 088304 (2015).

[39] C. P. Hsu, S. N. Ramakrishna, M. Zanini, N. D. Spencer, and L. Isa, P Natl Acad Sci USA **115**, 5117 (2018).

[40] L. C. Hsiao, I. Saha-Dalal, R. G. Larson, and M. J. Solomon, Soft Matter **13**, 9229 (2017).

[41] B. Schroyen, C.-P. Hsu, L. Isa, P. Van Puyvelde, and J. Vermant, Phys Rev Lett **122**, 218001 (2019).

[42] G. M. Conley, P. Aebischer, S. Nöjd, P. Schurtenberger, and F. Scheffold, Science Advances **3**, e1700969 (2017).

[43] L. Mohan, R. T. Bonnecaze, and M. Cloitre, Physical Review Letters **111**, 268301 (2013).

[44] Z. Zhou, J. V. Hollingsworth, S. Hong, H. Cheng, and C. C. Han, Langmuir **30**, 5739 (2014).

[45] D. Vlassopoulos and M. Cloitre, Current Opinion in Colloid & Interface Science **19**, 561 (2014).

[46] C. J. Dibble, M. Kogan, and M. J. Solomon, Phys Rev E **74** (2006).

[47] P. G. De Gennes, J. Physique Lett. **37**, 1 (1976).

[48] M. C. Jenkins, M. D. Haw, G. C. Barker, W. C. K. Poon, and S. U. Egelhaaf, Soft Matter **7**, 684 (2011).

[49] M. C. Jenkins, M. D. Haw, G. C. Barker, W. C. K. Poon, and S. U. Egelhaaf, Phys Rev Lett **107** (2011).

[50] J. D. Bernal and J. Mason, Nature **188**, 910 (1960).

[51] J. Brujić, C. Song, P. Wang, C. Briscoe, G. Marty, and H. A. Makse, Physical Review Letters **98**, 248001 (2007).

[52] L. Antl, J. W. Goodwin, R. D. Hill, R. H. Ottewill, S. M. Owens, S. Papworth, and J. A. Waters, Colloid Surface **17**, 67 (1986).

[53] L. Palangetic, K. Feldman, R. Schaller, R. Kalt, W. R. Caseri, and J. Vermant, Faraday Discuss **191**, 325 (2016).

[54] L. E. Silbert, Soft Matter **6**, 2918 (2010).

[55] B. A. D. Costello, P. F. Luckham, and T. F. Tadros, Langmuir **8**, 464 (1992).

[56] P. N. Pusey and W. Vanmegen, Nature **320**, 340 (1986).

[57] N. M. James, H. Xue, M. Goyal, and H. M. Jaeger, Soft Matter **15**, 3649 (2019).

[58] I. R. Peters, S. Majumdar, and H. M. Jaeger, Nature **532**, 214 (2016).

[59] D. Bi, J. Zhang, B. Chakraborty, and R. P. Behringer, Nature **480**, 355 (2011).

[60] G. L. Hunter and E. R. Weeks, Reports on Progress in Physics **75**, 066501 (2012).

[61] J. C. Crocker and D. G. Grier, J Colloid Interf Sci **179**, 298 (1996).

[62] R. S. Farr and R. D. Groot, The Journal of Chemical Physics **131**, 244104 (2009).

[63] S.-E. Phan, W. B. Russel, J. Zhu, and P. M. Chaikin, The Journal of Chemical Physics **108**, 9789 (1998).

[64] W. Schaertl and H. Sillescu, Journal of Statistical Physics **77**, 1007 (1994).

[65] K. W. Desmond and E. R. Weeks, Physical Review E **90**, 022204 (2014).

[66] R. P. A. Dullens, Soft Matter **2**, 805 (2006).

[67] W. C. K. Poon, E. R. Weeks, and C. P. Royall, Soft Matter **8**, 21 (2012).

[68] L. S. Ornstein and F. Zernike, P K Akad Wet-Amsterd **17**, 793 (1914).

[69] J. K. Percus and G. J. Yevick, Phys Rev **110**, 1 (1958).

[70] P. Varadan and M. J. Solomon, Langmuir **19**, 509 (2003).

[71] C. Zhang, N. Gnan, T. G. Mason, E. Zaccarelli, and F. Scheffold, Journal of Statistical Mechanics: Theory and Experiment **2016**, 094003 (2016).

[72] L. C. Hsiao, R. S. Newman, S. C. Glotzer, and M. J. Solomon, P Natl Acad Sci USA **109**, 16029 (2012).

[73] L. C. Hsiao, M. J. Solomon, K. A. Whitaker, and E. M. Furst, Journal of Rheology **58**, 1485 (2014).

[74] P. Varadan and M. J. Solomon, Journal of Rheology **47**, 943 (2003).

[75] A. I. Campbell, V. J. Anderson, J. S. van Duijneveldt, and P. Bartlett, Phys Rev Lett **94**, 208301 (2005).

[76] J.-P. Hansen and I. R. McDonald, in *Theory of Simple Liquids (Fourth Edition)*, edited by J.-P. Hansen, and I. R. McDonald (Academic Press, Oxford, 2013), pp. 13.

[77] A. Doroszkowski and R. Lambourne, Journal of Colloid and Interface Science **26**, 214 (1968).

[78] R. J. R. Cainrs, R. H. Ottewill, D. W. J. Osmond, and I. Wagstraff, Journal of Colloid and Interface Science **54**, 45 (1976).

[79] G. Bryant, S. R. Williams, L. Qian, I. K. Snook, E. Perez, and F. Pincet, Physical Review E **66**, 060501 (2002).

[80] J. I. N. Sun and S. Sundaresan, Journal of Fluid Mechanics **682**, 590 (2011).

[81] R. R. Radhakrishnan, John R.; Poon, Wilson C. K.; Sun, Jin, eprint arXiv:1904.03144 (2019).

[82] H. A. Vinutha and S. Sastry, Nature Physics **12**, 578 (2016).

[83] C. Song, P. Wang, and H. A. Makse, Nature **453**, 629 (2008).

[84] M. Delarue, J. Hartung, C. Schreck, P. Gniewek, L. Hu, S. Herminghaus, and O. Hallatschek, Nature Physics **12**, 762 (2016).

[85] B. Ferdowsi, C. P. Ortiz, and D. J. Jerolmack, P Natl Acad Sci USA **115**, 4827 (2018).

CHAPTER 3

Jamming Distance Dictates Colloidal Shear Thickening†

†Shravan Pradeep[1], Mohamad Nabizadeh[2], Alan R. Jacob[1], Safa Jamali[2], and Lilian C. Hsiao[1],

Preprint available, arXiv:2007.01825 (2021)

[1] Department of Chemical and Biomolecular Engineering, North Carolina State University,
Raleigh, North Carolina – 27695, USA

[2]Mechanical and Industrial Engineering Department, Northeastern University, Boston,
Massachusetts – 02115, USA

Abstract

We report experimental and computational observations of dynamic contact networks for colloidal suspensions undergoing shear thickening. The sterically stabilized poly(methyl methacrylate) hard colloids are spherically symmetric and possess different surface roughness. Confocal rheometry and dissipative particle dynamics simulations show that the shear thickening strength β scales exponentially with the deficit contact number z^* and the jamming distance $\Delta\phi/\phi_{\max}$. Rough colloids, which experience additional tangential and rolling constraints, require an average of 1.5 - 2 fewer particle contacts as compared to smooth colloids to generate the same β. Rough colloids with enhanced geometric friction do not experience a large change in the free volume near the jamming point, while smooth colloids must undergo significant reduction in the free volume to support an equivalent shear viscosity. The available free volume for different colloid roughness is related to the deficiency from the maximum number of nearest neighbors at jamming under shear. Our results further suggest that the force per contact is different for particles with different morphologies.

3.1 Introduction

Dense suspensions of colloidal particles with stochastic Brownian motion exhibit shear thickening under flow, a non-Newtonian behavior where the suspension viscosity η increases mildly or strongly depending on the applied shear stresses σ and particle volume fraction ϕ. The ability to design the onset of shear thickening provides a unique advantage in the reversible tuning of material mechanics, which is of great interest in fields such as soft robotics, impact and tear resistant fabrics, and liquid manufacturing [1-3]. However, the tunability in these systems currently remains at a rudimentary level of "on" or "off". For dense suspensions to truly advance technology, the level of control over the shear thickening needs to become more deliberate and refined [4,5]. In this manuscript, we show that designing shear thickening strength is possible for a broad class of colloidal suspensions through a singular parameter: the distance to jamming.

A jammed material at ϕ_J is conventionally defined as a disordered particulate system that has developed a yield stress [6]. Practically, this means that a sufficiently large, applied stress is required to generate a measurable flow rate in the densely packed material. Shear thickening shares similarities to jamming in that the particles in a flowing suspension become so impeded by nearest neighbors that they require an increasing amount of stress to continue flowing [1,7]. The microstructural origin of shear thickening was first attributed to the formation of hydroclusters in the Stokesian Dynamics simulations developed by Brady and Bossis [8], where clusters of particles oriented along the compressional axis of shear cause a modest increase in the suspension viscosity. Experiments later corroborated this observation [9], suggesting that the onset of shear-thickening can be discussed through a single dimensionless parameter, Peclet number, that represents the strength of hydrodynamic forces to thermal ones acting on colloids. The hydroclusters persist because the short-range lubrication forces, which are dissipative in nature, scale inversely as the particles' separation distance. More recently, simulations that incorporate explicit interparticle friction or particle roughness plus lubrication hydrodynamics were able to fully capture the large increase in viscosity that is characteristic of strong shear thickening [10]. An important result from these simulations is the appearance of space-spanning force chains and velocity correlations in shear thickened suspensions [11]. These force chains arise from any combination of σ- and ϕ-based constraints including hydrodynamics, repulsion, adhesion, and solid contact friction [12-14]. Above the onset stress, where the Peclet number ($Pe_{sh} = 6\pi\eta a_{eff}^3\,\dot{\gamma}\,/k_B T$) >> 1, the force networks constantly break and reform but these network structures persist throughout the flow. Beyond a critical Pe_{sh}, the force chains proliferate and grow stronger as a system approaches shear jamming, leading to stronger shear thickening [15]. Interestingly, conventional microstructural characterization techniques such as the radial distribution function [14] or scattering patterns in the velocity-gradient-vorticity planes [16] are not sensitive to differences between shear thickened states. This observation implies that the distance between particle surfaces, rather than the center-to-center distance, is related to the force chains. As $\phi \rightarrow \phi_J$ and σ increases, conservation laws state that the contact distance between particles in a constant-volume suspension must decrease, leading to a greater number of contacts, except for volume expansion at the free boundary for a few DST dominated flows. To address a lack of experimental evidence of force chains in the literature, we focus on the details of the dynamic contact networks formed by dense colloidal suspensions in shear thickening flows.

We use the mean contact number <z>, a measure for the number of contacting nearest neighbors around particles, to quantify the suspensions because of the strong correlation of <z> with bulk mechanics [17]. Near the jamming point, the contact number at jamming, z_J, and ϕ_J are inextricably linked to the interparticle friction in dense packings. For instance, application of

Maxwell's isostatic criterion to a frictionless hard sphere system at $\phi_J = 0.64$ reveals that $z_J = 6$. Incorporating an infinitely large sliding friction coefficient between colloids, $\mu_s \to \infty$, leads to $z_J \to 4$, and $\phi_J \to 0.54$ [18], while adding a rolling friction coefficient μ_r further reduces $z_J \to 2.4$, $\phi_J \to 0.36$ for $(\mu_r, \mu_s) \to \infty$ [19]. The sliding constraint μ_s is featured in several constitutive equations, particle simulations, and phenomenological models that describe shear thickening as due to particles undergoing a stress-induced lubricated-to-frictional transition beyond an onset stress σ^* [20-22]. Both μ_s and μ_r are thought to generate long-lasting force chains by reducing the rotational degree of freedom of particles in flow. Experimental measurements support this idea by demonstrating that the rotational dynamics of shape-symmetric particles with protrusions deviate significantly from simulations of hard sphere suspensions [23-25]. While the interparticle friction may not always track with surface roughness because of complex tribological factors (*e.g.*: elastohydrodynamics [26,27]), in general, rougher particles have larger values of μ_s and μ_r. In this manuscript, we focus on characterizing the contact microstructure of shear thickening suspensions comprising of smooth and rough colloids.

3.2. Materials and Methods

To investigate the role of friction on the contact microstructure of shear thickening colloidal suspensions, we use confocal rheometry experiments and dissipative particle dynamics (DPD) simulations to identify a quantitative link between the strength of thickening $\beta = \log(\Delta\eta)/\log(\Delta\sigma)$ and the distance from jamming $(\phi_{max} - \phi)/\phi_{max} = \Delta\phi/\phi_{max}$ for smooth and rough colloids. Here, ϕ_{max} refers to the maximum jamming fraction for a disordered packing, where $\phi_{max} = \phi_J$ (σ = 0 Pa) is obtained from confocal microscopy performed on colloids that have undergone unperturbed sedimentation under gravitational stress for three months. We obtain β

using the average slope at the inflection points above σ^* and before the high shear plateau. At ϕ_{max}, the suspension is considered mechanically rigid, where forces on the individual particles are fully balanced with respect to total torque and stresses such that the suspension is not flowable at or beyond this volume fraction. The value of ϕ_{max} is verified independently within an experimental uncertainty of ± 5% by fitting the relative low-shear viscosity ($\eta_{r,low\text{-}shear}$) divergence to the form $\eta_{r,low\text{-}shear} = (1 - \phi/\phi_{max})^{-2}$. The value of ϕ_{max} is a key parameter in normalizing the jamming distance because it varies for colloids with different surface morphologies.

Earlier treatise on suspension rheology have seen the prolific use of smooth hard spheres, and only recently have poly(methyl methacrylate) (PMMA) and silica colloids with controlled surface roughness become widely available [28]. We hypothesize that there is a universal correlation between $\Delta\phi/\phi_{max}$, β, and <z> for all suspensions exhibiting shear thickening. To reveal this relationship, we synthesize spherically symmetric and size-monodisperse PMMA microspheres with different levels of surface roughness [29]. These particles are sterically stabilized with poly(12-hydroxystearic acid) (PHSA) brushes of lengths 10 – 15 nm [30]. We prepare suspensions at $\phi < \phi_{max}$ by first centrifuging the stock suspension at gravitation Peclet number, $Pe_g = 1500$ ($Pe_g = 4\pi a_{eff}^4\Delta\rho g/3k_BT$), and subsequently diluting the shear jammed sediments with known volumes of solvent. We obtain ϕ by imaging the fluorescent colloids with confocal laser scanning microscopy (CLSM, Leica SP8) and processing the 3D image volumes using a brightness-weighted centroid-based algorithm [31]. We obtain particle diameters $2a$ and $2a_{eff}$, respectively, from the 2D images of the sedimented layer using confocal microscopy. For rough particles, $2a_{eff}$ is estimated as an effective particle diameter between the opposite end of surfaces that minimizes the roughness. Separately, steady shear rheological measurements are performed using a stress-controlled rheometer (TA Instruments DHR-2) fitted with a 50-mm sandblasted cone-and-plate geometry. To capture the transient contact microstructure during flow, we use a custom confocal rheometer and arrest the suspension samples at two applied stresses: one in the low-shear regime and one in the shear thickening regime.

3.3 Results

3.3.1 Steady shear rheology

Figure 3.1 shows different rheological behavior of PMMA hard colloids with two types of morphology and similar effective swollen diameters $2a_{eff}$, smooth (S, $2a$ = 1.65 μm ± 4%, Figure 3.1a) and rocky (RK, $2a_{eff}$ = 1.49 μm ± 6%, Figure 3.1b). Two other morphologies are also studied: slightly rough (SR, $2a_{eff}$ = 1.82 μm ± 5%), very rough (VR, $2a_{eff}$ = 1.47 μm ± 6%). These steady shear flow curves describe the relative suspension viscosity ($\eta_r = \eta/\eta_s$, solvent viscosity η_s = 0.012 Pa·s) as a function of scaled σ. The dotted lines represent the two stress points at which we obtain <z> values from dynamic packings: one at $\tilde{\sigma} = \tilde{\sigma}_{\beta=0} < \tilde{\sigma}^*$ and the second at $\tilde{\sigma} = \tilde{\sigma}_{\beta} > \tilde{\sigma}^*$, where the overhead ~ represents the stress values scaled with a factor of a_{eff}^3/k_BT. In our flow curves, we choose $\tilde{\sigma}_{\beta=0} \approx 200$ at the low-shear viscosity plateau and $\tilde{\sigma}_{\beta} \approx 10^4$ at the shear thickening regime for contact microstructure studies, as shown in Figure 3.1. As $\tilde{\sigma}$ increases beyond $\tilde{\sigma}^*$, the steric and lubrication layers between the colloids gives way to the solid-solid proliferation of interparticle contacts [21,32]. Moreover, experiments with rough colloids and granular materials have shown that rough particles exhibit higher β and lower $\tilde{\sigma}^*$ [33-35] at lower ϕ than smooth particles.

Regardless of the surface morphology, the suspensions transition from fully Newtonian flow at low σ and ϕ, to continuous shear thickening (CST, $\beta < 1$) at intermediate σ and ϕ, and finally to discontinuous shear thickening (DST, $\beta \geq 1$) at high σ and when ϕ is close to ϕ_{max}. There is no clear demarcation between CST and DST in many practical scenarios, but in general DST occurs when the value of $\beta \approx 1$. Suspensions also exhibit a secondary plateau at the highest values of σ, commonly observed in shear thickened states in which the particles' motion is hindered by either frictional or hydrodynamic forces [13,14,19,21,36]. The onset of DST for smooth particle suspensions occurs at $\phi = 0.55$ (Figure 3.1a), which is similar to the values reported earlier in the literature for colloids interacting with a short-range repulsive potential [37,38]. Suspensions of smooth colloids continue to exhibit DST until $\phi_{max,\mathrm{S}} = 0.64 \pm 0.01$ where the samples reach ϕ_{max} and become difficult to handle experimentally.

3.3.2 Universal correlation in shear thickening behavior

Our data show that $\Delta\phi/\phi_{max}$ predicts β for different types of colloidal suspensions containing spherically symmetric particles. Figure 3.2 shows that all colloidal suspensions obey the general scaling of the form, $\beta \sim \exp(-\Delta\phi/\phi_{max})$, where DST ($\beta \approx 1$) is present at $\Delta\phi/\phi_{max} \leq 0.1$ and CST ($\beta < 1$) is found at $\Delta\phi/\phi_{max} > 0.1$. The value of β rapidly decreases at increasing $\Delta\phi/\phi_{max}$. Additional support for this correlation comes from β and $\Delta\phi/\phi_{max}$ values extracted from a number of literature studies in which both η-σ data and ϕ_{max} are available, including: (1) smooth and rough PMMA colloids with charged interactions [33,37], (2) smooth and rough silica colloids with near-hard sphere and charge-screened interactions [34,36,39,40], (3) computer simulations that incorporate particle-level sliding [22,32] and rolling friction [19], and one in which the colloids have explicitly defined surface asperities [13]. This scaling has significant impact in the academic and industrial communities because it enables the *a priori* estimation of shear thickening strength (a non-equilibrium parameter) using the distance to jamming point (an equilibrium parameter). The remarkable match between experiments and simulations from independent research groups suggests that there exists a direct link between the dynamic shear thickening microstructure of colloids and their respective equilibrium jamming distance. This link is more clearly illustrated using the dynamic <z> values of shear thickening suspensions to understand how the contact networks are related to $\Delta\phi/\phi_{max}$.

3.3.3 Confocal rheometry experiments

To characterize the contact microstructure of dense suspensions at the large applied stresses used to induce shear thickening, we use a custom confocal rheometer setup (Figure 3.3a), where a stress-controlled rheometer (Anton Paar MCR 502 WESP) is directly coupled to a CLSM (Leica SP8) similar to an earlier set up described in the literature [41]. Steady shear is applied to suspensions of smooth and rough colloids using a 20 mm parallel-plate top geometry and a glass coverslip at the bottom with thickness 0.16 – 0.19 mm. The confocal rheometer is used to obtain 3D image volumes of dense suspensions undergoing steady shear at $\tilde{\sigma}_{\beta=0}$ and $\tilde{\sigma}_{\beta}$, as described in Figure 3.1. Each stack of size 50 μm × 50 μm × 10 μm is imaged in under 6 s and contain ~ 10^4 particles. The suspensions contain 5 wt% mixture of photopolymer and photoinitiator additives to rapidly arrest the suspensions with ultraviolet (UV) light within 1 s. To obtain the sheared microstructure, we hold the suspensions at constant stresses, at values marked in Figure 3.1, for 150 s and shine UV light (λ_{exc} = 405 nm) for 10 s immediately after the stress drops to zero, thus locking in the sheared suspension microstructure. We perform three independent experiments and obtain image stacks from three different points in each sheared sample. All image stacks are imaged at least 15 μm above the coverslip to avoid wall effects.

3.3.4 Dissipative Particle Dynamic (DPD) simulations

The images obtained from the confocal rheometer experiments are supported using dissipative particle dynamics (DPD) simulations of bidisperse suspensions (a and $1.1a$ in an equal volume ratio with total number of particles $N = 1000$) containing smooth and rough colloids closely representing the experimental system. The particle roughness is modeled by distributing asperities of lengthscale $0.1a$ on the surface of the smooth base spheres, using a scheme similar to simulations in [13,14]. The solvent is modeled through explicit soft particles and interact through conservative, dissipative, and random Brownian forces. We have shown previously that this modified DPD scheme recovers a full representation of hydrodynamics in the system, similar to a fully resolved Stokesian Dynamics formalism. To compare the data from simulations and experiments, we use the suspension systems with smooth and rough particles in simulations match the ϕ_{max} to suspensions with S and RK systems from the experiments, respectively. The goal is to link β to <z> to capture the contact networks responsible for the shear thickening phenomena.

Defining interparticle contact during shear thickening requires the use of two different contact criteria at $\sigma < \sigma^*$ and at $\sigma \geq \sigma^*$, because the particles undergo a transition from lubricated to frictional flow and the soft PHSA brush becomes compressed by the large applied stresses [33]. At $\sigma < \sigma^*$, two particles are defined to be in hydrodynamic contact if the interparticle separation is equal or less than the uncertainties that include the PHSA brush length, size polydispersity, and surface roughness [29]. At $\sigma \geq \sigma^*$, a frictional contact is defined by the average center-to-center distance between particles, $2a_{eff}$ as shown in Figure 3.3b. In DPD simulations, interparticle contacts are defined similarly for all particles and their interactions with other asperities and base particles. Experimental results are in excellent agreement with the contact microstructure obtained from DPD simulations for smooth and rough particles: the <z> values obtained from DPD simulations fall within the error limits of the <z> values obtained from our experimental packings, as shown in Figure 3.4a.

3.3.5 Visualizing contact networks

Visual Molecular Dynamics (VMD) renderings of the dynamic packings, at $\tilde{\sigma}_\beta$, from the experiments and simulations for suspensions containing smooth and rough particles at $\Delta\phi/\phi_{max}$ = 0.08 and $\beta \approx 0.85$ are shown in Figure 3.3c-d. The renderings show the presence of space-spanning contact networks in both experiments and simulations of shear thickening flows and provide a statistical view of how smooth and rough pack differently in non-equilibrium shear thickening flows. Particles are concentrated in the compressive flow axis, in agreement with previous neutron scattering studies on shear thickening suspensions [16]. The observed contact networks are also qualitatively similar to the percolations in strained systems of 2D photoelastic disks [42,43]. A first step towards constructing a statistical mean-field description parameter of the contact microstructure formed in such networks would be possible by evaluating the relationship between the dynamic contact number at $\tilde{\sigma}_\beta$,$<z>_\beta$, and β for suspensions at various ϕ.

Figure 3.4a shows the dynamic contact number, $<z>_\beta$, as a function of $\Delta\phi/\phi_{max}$ for sheared suspensions of smooth and rough colloids. The dashed lines in Figure 3.4a indicate that the smooth colloids, on average, requires an additional of 1.5 – 2 contacts to maintain the same β as compared to the rough colloids. This could be a consequence of a larger change in free volume for smooth particles in shear flow. In other words, smooth colloids must become more compacted by the applied stress before $<z>_\beta$ reaches the jammed state, in which the entire suspension becomes mechanically rigid and therefore no longer flowable. For rough colloids, geometric hindrance and an effective rolling friction reduces the change in free volume such that $<z>_\beta$ does not need to be as large to cause jamming. The difference in available free volume for different types of colloid roughness is related to the deficiency from the maximum number of nearest neighbors at jamming under shear. The value of $<z>_\beta$ is a function of $\tilde{\sigma}_\beta$ because the external deformation imparts an additional non-equilibrium free energy that must be minimized for steady flow [44]. To normalize the spatial effect of interparticle contacts that stem from free volume differences, we define a parameter z^* that captures the scaled contact deficit, where $z^* = (z_{J,\beta} - <z>_\beta)/z_{J,\beta}$. Here, $z_{J,\beta}$ is the maximum possible contacts available at $\phi_{J,\beta}$, which is defined as the divergence of the viscosity at $\tilde{\sigma}_\beta$ and indicate the maximum flowable volume fraction at $\tilde{\sigma}_\beta$.

3.3.6 Contact deficiency at local jamming

To estimate the shear-induced jamming point $\phi_{J,\beta}$ for suspensions of smooth and rough colloids, we invoke an argument that relates the divergence of η_r to $(\phi_J - \phi)$ at a given σ, where $\phi_J = \phi_J(\sigma)$. Specifically, the low-shear and high-shear viscosities are expected to diverge at ϕ_{max} and a σ dependent ϕ_J, respectively, with an exponent of -2 [45]. By extension, this suggests that η_r at intermediate σ should also diverge to a corresponding stress-dependent quasi-jamming point, $\phi_{J,\beta} = \phi_{J,\beta}(\tilde{\sigma}_\beta)$ with the same exponent of -2. The inset in Figure 3.4b. shows the scaling of the form $\eta_r \sim (\phi_{J,\beta}-\phi)^{-2}$ where $\phi_{J,\beta} = 0.61$ and 0.51 for smooth and rough colloids, respectively. The value of $z_{J,\beta}$ is then obtained by extrapolating $<z>_\beta$ at various ϕ to the respective quasi-jamming points $\phi_{J,\beta}$, where $z_{J,\beta}$ as 4.95 ± 0.02 and 3.25 ± 0.01 for smooth and rough colloids. Figure 3.4b shows that the dynamic contact scaling takes the form $z^* \sim (\Delta\phi/\phi_{max})^\alpha$ with $\alpha = 0.98 \pm 0.01$. A similar scaling ($\alpha = 1.08$) had been observed in 2D simulations of soft frictionless particles that are repulsive [46]. The observed power-law correlation in Figure 3.4b is statistically significant with a normalized chi-squared parameter $\bar{\chi}_0^2 = 6.33$.

3.4. Discussions

Normalizing the contact number deficit in this manner collapses the data for all particle roughness and support our argument that the contact number at shear-induced jamming is a measure of the free volume available for particles with specific morphologies, or interparticle friction, to rearrange in a way to allow the suspension to flow at steady state. In Figure 3.1**,** following the dashed lines corresponding to $\tilde{\sigma}_\beta$ vertically, increase in ϕ is associated with an increase in β as more contacts are made. Corresponding values of $\Delta\phi/\phi_{max}$ and z^* decreases forming more space-spanning contacts and force networks. For a given shear thickening σ, for each particle system, there exists a ϕ_J and corresponding z_J beyond which there is no steady state flow. Thus, smooth and rough colloids with similar $2a_{eff}$ are characterized with different $\phi_{J,\beta}$ and $z_{J,\beta}$ at the same applied $\tilde{\sigma}_\beta$. In a constant volume rheological experiment restricted by the dimensions of experimental and simulation setup, the free volume available to rearrange under shear is greater for smooth colloids than that of the rough colloids, because smooth colloids can rotate freely with little hydrodynamic resistance. There are more spatial constraints imposed by the restricted rotational degree of freedom of rough colloids, and this is in turn captured by the deficiency of nearest neighbors to the shear-jamming contact number, $z_{J,\beta}$. The universality in Figure 3.4b shows that this physical mechanism for shear thickening holds for all types of suspensions and thus the parameter z^*, which is a contact network parameter that captures the distance to $z_{J,\beta}$, can be used as the manifestation of the modes of particle motion under shear.

The dynamic contact scaling $z^* \sim \Delta\phi/\phi_{max}$ (Figure 3.4b) and the static packing correlation $\beta \sim \exp(-\Delta\phi/\phi_{max})$ (Figure 3.2) can be combined to relate the sheared contact microstructure and the shear thickening strength as $\beta \sim \exp(-z^*)$. This key relation implies that the onset of shear thickening occurs when a minimally rigid network is formed, and the strength of the shear thickening depends on the way in which σ pushes particles to their dynamic jamming contacts. The power-law correlation in Figure 3.4b is likely related to the force per contact of these suspensions under shear. The results suggest that at a given β, because $\langle z \rangle$ is different for suspensions of particles with different asperities, the force carried by each contact is different for particles of different morphologies.

Force networks in jammed granular particles interacting through hard-sphere potential are described by two quantities: the particle positions and the contact networks [47]. Earlier work on compressed hydrogel beads found that the average macroscopic force, F, scales with average dynamic contacts as $F \sim \langle z \rangle$ [48]. To obtain same change in suspension stress (or β), rough particles suspensions required, on average, fewer contacts compared to suspensions with smoother particles. In other words, for the same F in our systems, $F/\langle z \rangle$ for rough particle suspensions must be greater than that of smooth counterpart. We indirectly capture the force per contact through parameter z^*, which factors in the contact deficit for various type of particle suspensions. Note that the contact networks found in this work would likely have different morphologies and properties from the force chains observed in previous studies [11].

3.5 Conclusions

As a suspension shear thickens, clusters and percolated networks of particle contacts break and reform, but our study has shown that a mean-field description using dynamic $\langle z \rangle$ can connect β and $\Delta\phi/\phi_{max}$. The dynamic contact scaling may break down at ϕ values close to ϕ_{max} ($\Delta\phi/\phi_{max} \leq 10^{-2}$) due to pronounced flow instabilities such as localized stress fluctuations, periodic density fluctuations in flow direction, large transient clusters in compressive direction, and stress bands along the dilatational direction [49-51]. The increase in uncertainty in z^* close to the jamming point could be due to these flow instabilities. Nonetheless, our study shows that the scaled jamming distance is a strong predictor for the shear thickening behavior of a broad class of suspensions.

Because force networks are likely coupled to the contact network and particle positions, future studies that analyze the transient network anisotropy could provide new insight as to how different types of frictionless and frictional particles carry load in flowing systems. Athermal suspensions [52] and shape-anisotropic colloids [53] have not been tested in this study, and it would be interesting to see if the proposed scaling between β, $\Delta\phi/\phi_{max}$, and z^* hold for these materials.

Acknowledgements. We thank John Brady, Ronald Larson, Jeffrey Morris, and Abhinendra Singh for discussions. This work is supported in part by the National Science Foundation (NSF CBET-1804462), the American Chemical Society Petroleum Research Fund (ACS-PRF #59208-DNI9), and North Carolina State University start-up funds.

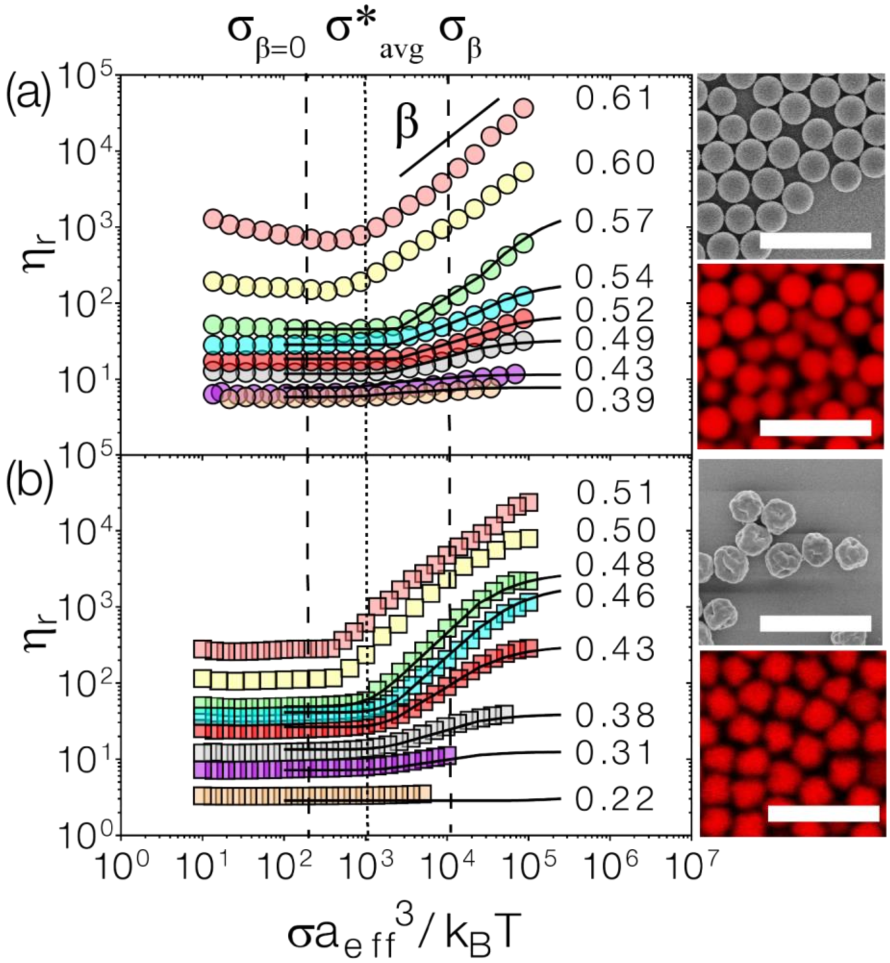

Figure 3.1 | Flow curves for dense suspensions. Experimental rheology for suspensions of (a) smooth and (b) rough colloids. Flow curves represent η_r plotted against σ scaled by the effective particle radii and temperature. Numerical values next to each curve indicate respective ϕ (filled). Solids lines are fit with Wyart-Cates mathematical model. Vertical dashed lines represent stresses below and above the onset stress (vertical dotted line) where we obtain the average contact number. Representative scanning electron micrographs and confocal micrographs of colloids are shown to the right side of respective flow curves. Scale = 5 µm.

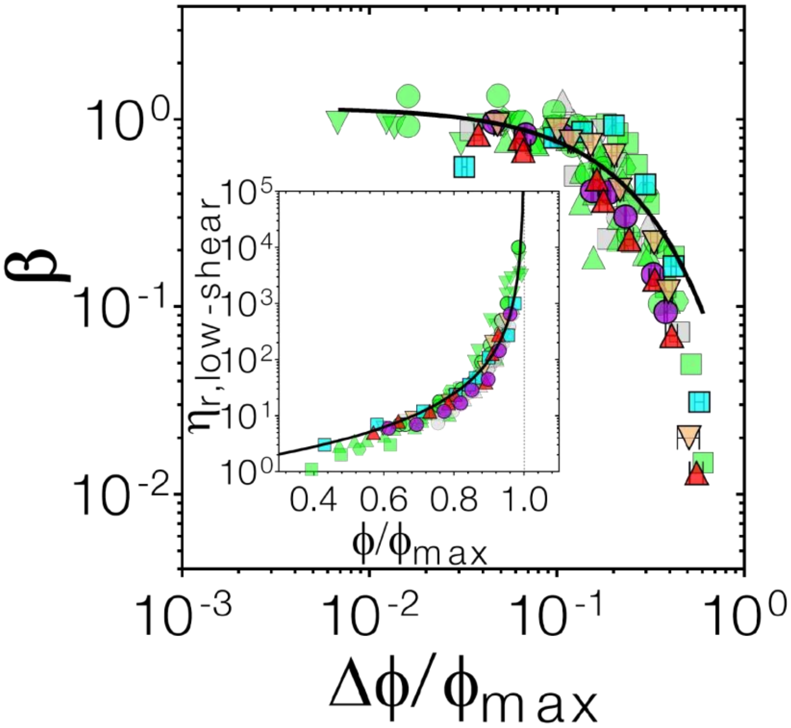

Figure 3.2 | Shear thickening strength as a function of jamming distance. Data from this work are shown for S (magenta circles), SR (red upper triangles), VR (coral lower triangles), and RK (cyan squares) colloids. Solid line indicates an emperical fit of the form: $\beta = \beta_0 \exp\left(\Delta\phi/\phi_{\max} k\right)$ with β_0 = 1.61±0.05 and k = -4.18±0.32. Literature values from experimental colloidal studies are indicated by green symbols: smooth PMMA (circle) [37], rough PMMA (upper triangle) [33], smooth silica (square [40] and (hexagon) [36]), and rough silica (lower triangle [39] and diamond [34]). Literature values from simulations are indicated by grey symbols: colloids with surface asperities interacting via lubrication (square) [11], spheres with sliding friction (upper triangle) [22], spheres with sliding and rolling friction (circle) [19], and colloids interacting via sliding friction (lower triangle) [32]. Inset shows the fitting to the form: $\eta_r = (1-\phi/\phi_{\max})^{-2}$ normalized for each particle $\phi_{\max}$ values. Solid line represents the universal low-shear viscosity divergence.

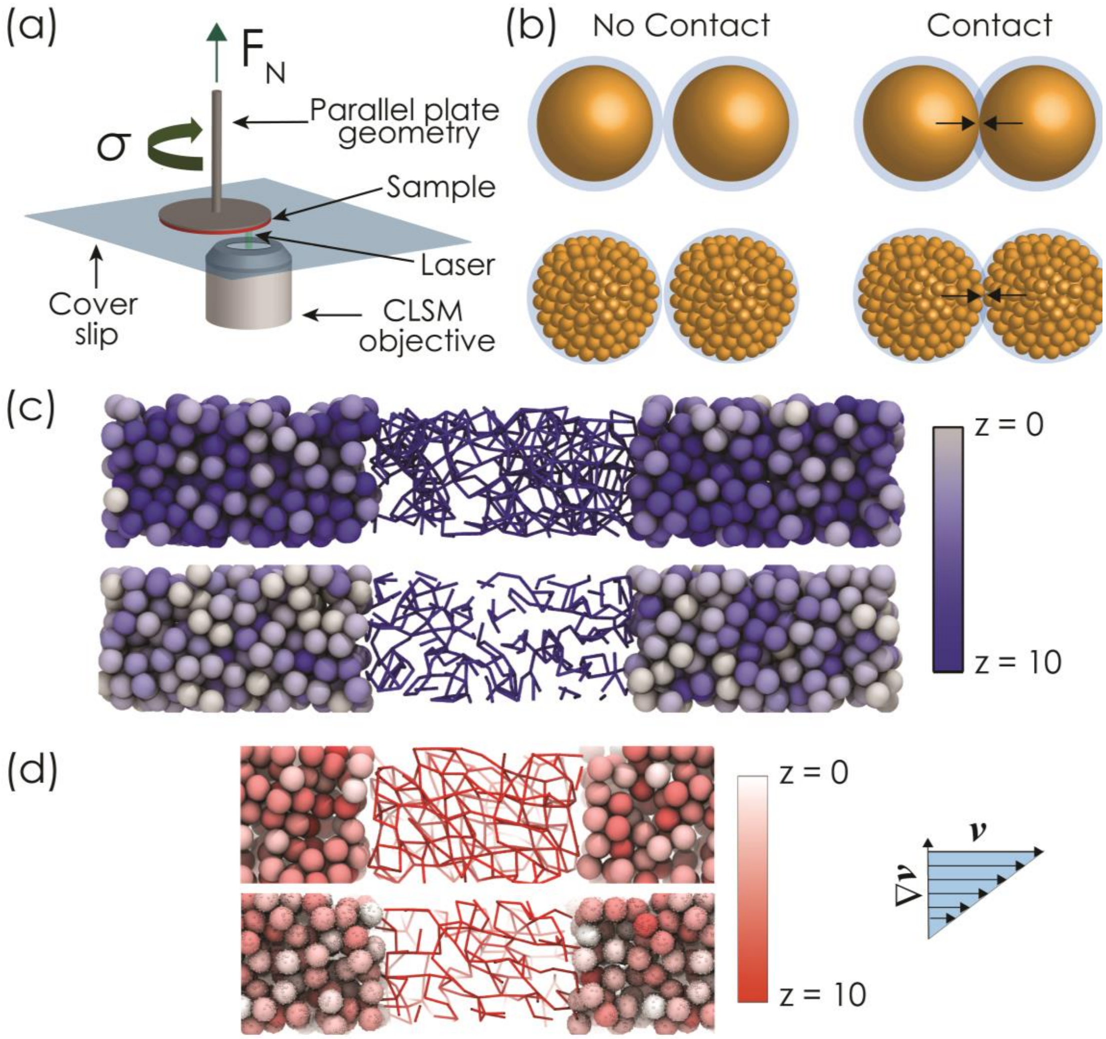

Figure 3.3 | Confocal rheometry and force network visualization. (a) Confocal rheometer setup for imaging shear-induced contact networks during the flow measurements. (b) Contact criterion for interparticle contact in smooth (top row) and rough (bottom row) colloids. The light blue circle represents additional experimental length scales. (c,d) Contact networks of shear thickening suspensions at $\Delta\phi/\phi_{max} = 0.075$ and $\beta = 0.85$ as shown in VMD reconstructions of the (c) experimental microstructures and (d) snapshots from simulations. For (c) and (d), the top panel are for the suspensions with smooth particles and the bottom panels are for rough colloidal suspensions. Side insets show color panel for the respective contact numbers of the particles shown in (c,d).

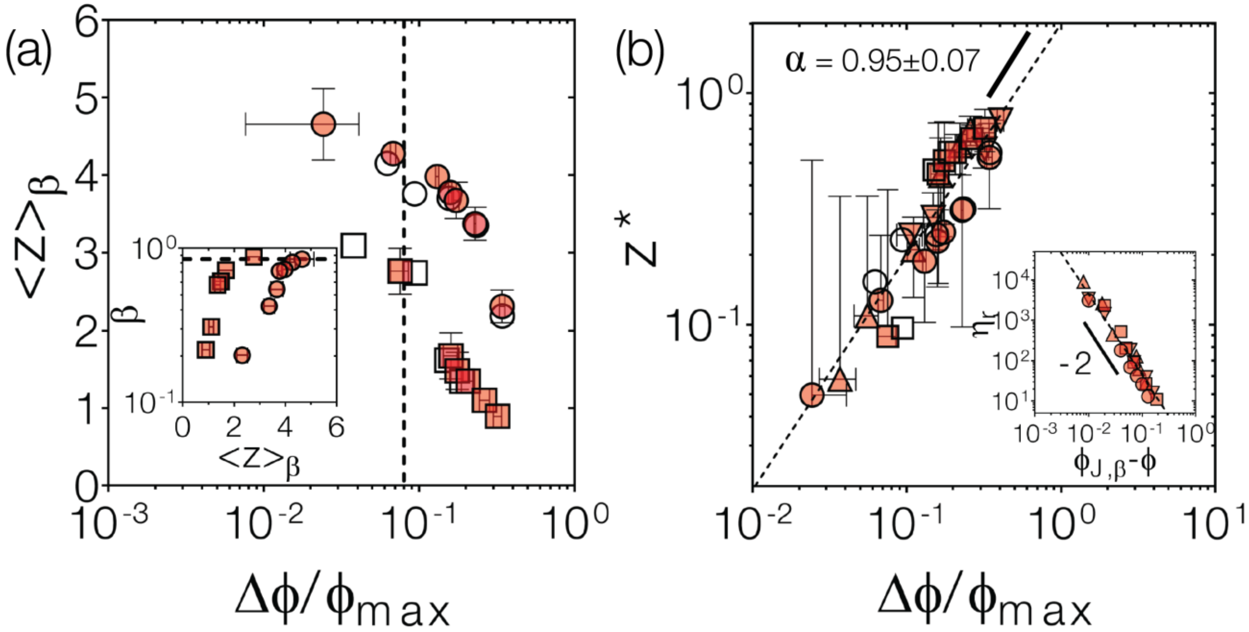

Figure 3.4. Dynamic contact microstructure in shear thickening suspensions. (a) The change in $<z>_\beta$ of smooth (circles) and rough (squares) colloids from experiments (filled) and simulations (unfilled) as a function of $\Delta\phi/\phi_{\mathrm{max}}$. Inset shows the β as a function of $<z>_\beta$. Dashed lines in the main figure and the inset corresponds to the suspensions at $\Delta\phi/\phi_{\mathrm{max}} \approx 0.075$ and $\beta \approx 0.85$ (b) The scaling $z^* \sim (\Delta\phi/\phi_{\mathrm{max}})^\alpha$. Dashed line indicates the power law fit. Inset shows the scaling relation between the relative viscosity and unscaled jamming distance to test the fit, $\eta_r \sim (\phi_J\text{-}\phi)^{-2}$. Two additional types of rough particles: SR (upper triangles) and VR (lower triangles) are included here.

References

[1] E. Blanco, D. J. M. Hodgson, M. Hermes, R. Besseling, G. L. Hunter, P. M. Chaikin, M. E. Cates, I. Van Damme, and W. C. K. Poon, Proceedings of the National Academy of Sciences **116**, 10303 (2019).

[2] E. Brown, N. Rodenberg, J. Amend, A. Mozeika, E. Steltz, M. R. Zakin, H. Lipson, and H. M. Jaeger, Proceedings of the National Academy of Sciences **107**, 18809 (2010).

[3] Y. S. Lee, E. D. Wetzel, and N. J. Wagner, Journal of Materials Science **38**, 2825 (2003).

[4] Y. Madraki, G. Ovarlez, and S. Hormozi, Physical Review Letters **121**, 108001 (2018).

[5] N. Y. C. Lin, C. Ness, M. E. Cates, J. Sun, and I. Cohen, Proceedings of the National Academy of Sciences **113**, 10774 (2016).

[6] C. S. O’Hern, L. E. Silbert, A. J. Liu, and S. R. Nagel, Physical Review E **68**, 011306 (2003).

[7] I. R. Peters, S. Majumdar, and H. M. Jaeger, Nature **532**, 214 (2016).

[8] J. F. Brady and G. Bossis, Annual Review of Fluid Mechanics **20**, 111 (1988).

[9] J. Bender and N. J. Wagner, Journal of Rheology **40**, 899 (1996).

[10] J. F. Morris, Physical Review Fluids **3**, 110508 (2018).

[11] J. E. Thomas, K. Ramola, A. Singh, R. Mari, J. F. Morris, and B. Chakraborty, Physical Review Letters **121**, 128002 (2018).

[12] E. Brown and H. M. Jaeger, Reports on Progress in Physics **77**, 046602 (2014).

[13] S. Jamali and J. F. Brady, Physical Review Letters **123**, 138002 (2019).

[14] M. Wang, S. Jamali, and J. F. Brady, Journal of Rheology **64**, 379 (2020).

[15] R. J. E. Andrade, A. R. Jacob, F. J. Galindo-Rosales, L. Campo-Deaño, Q. Huang, O. Hassager, and G. Petekidis, Journal of Rheology **64**, 1179 (2020).

[16] A. K. Gurnon and N. J. Wagner, Journal of Fluid Mechanics **769**, 242 (2015).

[17] E. Somfai, M. van Hecke, W. G. Ellenbroek, K. Shundyak, and W. van Saarloos, Physical Review E **75**, 020301 (2007).

[18] L. E. Silbert, Soft Matter **6**, 2918 (2010).

[19] A. Singh, C. Ness, R. Seto, J. J. de Pablo, and H. M. Jaeger, Physical Review Letters **124**, 248005 (2020).

[20] M. Wyart and M. E. Cates, Physical Review Letters **112**, 098302 (2014).

[21] R. Seto, R. Mari, J. F. Morris, and M. M. Denn, Physical Review Letters **111**, 218301 (2013).

[22] A. Singh, R. Mari, M. M. Denn, and J. F. Morris, Journal of Rheology **62**, 457 (2018).

[23] L. C. Hsiao, I. Saha-Dalal, R. G. Larson, and M. J. Solomon, Soft Matter **13**, 9229 (2017).

[24] S. Jiang, J. Yan, J. K. Whitmer, S. M. Anthony, E. Luijten, and S. Granick, Physical Review Letters **112**, 218301 (2014).

[25] K. V. Edmond, M. T. Elsesser, G. L. Hunter, D. J. Pine, and E. R. Weeks, Proceedings of the National Academy of Sciences **109**, 17891 (2012).

[26] Y. Peng, C. M. Serfass, C. N. Hill, and L. C. Hsiao, Experimental Mechanics (2021).

[27] Y. Peng, C. M. Serfass, A. Kawazoe, Y. Shao, K. Gutierrez, C. N. Hill, V. J. Santos, Y. Visell, and L. C. Hsiao, Nature Materials (2021).

[28] L. C. Hsiao and S. Pradeep, Current Opinion in Colloid & Interface Science **43**, 94 (2019).

[29] S. Pradeep and L. C. Hsiao, Soft Matter **16**, 4980 (2020).

[30] M. T. Elsesser and A. D. Hollingsworth, Langmuir **26**, 17989 (2010).

[31] J. C. Crocker and D. G. Grier, Journal of Colloid and Interface Science **179**, 298 (1996).

[32] R. Mari, R. Seto, J. F. Morris, and M. M. Denn, Proceedings of the National Academy of Sciences **112**, 15326 (2015).

[33] L. C. Hsiao, S. Jamali, E. Glynos, P. F. Green, R. G. Larson, and M. J. Solomon, Physical Review Letters **119**, 158001 (2017).

[34] D. Lootens, H. van Damme, Y. Hémar, and P. Hébraud, Physical Review Letters **95**, 268302 (2005).

[35] C.-P. Hsu, S. N. Ramakrishna, M. Zanini, N. D. Spencer, and L. Isa, Proceedings of the National Academy of Sciences **115**, 5117 (2018).

[36] C. D. Cwalina and N. J. Wagner, Journal of Rheology **58**, 949 (2014).

[37] B. M. Guy, M. Hermes, and W. C. K. Poon, Physical Review Letters **115**, 088304 (2015).

[38] O. Sedes, A. Singh, and J. F. Morris, Journal of Rheology **64**, 309 (2020).

[39] C. P. Hsu, S. N. Ramakrishna, M. Zanini, N. D. Spencer, and L. Isa, Proceedings of the National Academy of Sciences of the United States of America **115**, 5117 (2018).

[40] J. R. Royer, D. L. Blair, and S. D. Hudson, Physical Review Letters **116**, 188301 (2016).

[41] S. K. Dutta, A. Mbi, R. C. Arevalo, and D. L. Blair, Review of Scientific Instruments **84**, 063702 (2013).

[42] D. Bi, J. Zhang, B. Chakraborty, and R. P. Behringer, Nature **480**, 355 (2011).

[43] T. S. Majmudar and R. P. Behringer, Nature **435**, 1079 (2005).

[44] V. Kobelev and K. S. Schweizer, Physical Review E **71**, 021401 (2005).

[45] M. Wang and J. F. Brady, Physical Review Letters **115**, 158301 (2015).

[46] M. Maiti, H. A. Vinutha, S. Sastry, and C. Heussinger, The Journal of Chemical Physics **143**, 144502 (2015).

[47] R. P. Behringer and B. Chakraborty, Reports on Progress in Physics **82**, 012601 (2018).

[48] N. Brodu, J. A. Dijksman, and R. P. Behringer, Nature Communications **6**, 6361 (2015).

[49] G. Ovarlez, A. Vu Nguyen Le, W. J. Smit, A. Fall, R. Mari, G. Chatté, and A. Colin, Science Advances **6**, eaay5589 (2020).

[50] S. Saw, M. Grob, A. Zippelius, and C. Heussinger, Physical Review E **101**, 012602 (2020).

[51] V. Rathee, D. L. Blair, and J. S. Urbach, Proceedings of the National Academy of Sciences **114**, 8740 (2017).

[52] A. Fall, N. Huang, F. Bertrand, G. Ovarlez, and D. Bonn, Physical Review Letters **100**, 018301 (2008).

[53] L. Palangetic, K. Feldman, R. Schaller, R. Kalt, W. R. Caseri, and J. Vermant, Faraday Discussions **191**, 325 (2016).

CHAPTER 4

Linear viscoelasticity in dense suspensions of smooth and rough colloids

Shravan Pradeep, Alan Wessel, and Lilian C Hsiao

Department of Chemical and Biomolecular Engineering, North Carolina State University,

Raleigh, NC 27695, USA

Abstract

In dense suspensions that comprise of colloids which interact via a hard sphere potential, the viscoelastic components of the stress response are determined by the excluded volume effects and the hydrodynamics. The near-equilibrium structure of suspensions with smooth and rough colloids is probed to decouple the effect of surface roughness-induced effects on the elastic and the viscous moduli. Changes in the scaled moduli on suspensions containing smooth and rough poly(methylmethacrylate) colloids are studied as a function of the distance to the maximum packing or the jamming distance. At $\phi > 0.50$ the frequency-sweep rheometry show that smooth particle suspensions exhibit a scaled modulus ~10 Pa while rough particle suspensions exhibit a modulus ~ 10^5 Pa. We generate a master Maxwell curve by performing frequency-ϕ superposition for our colloidal suspensions. Furthermore, we capture the effect of surface roughness on local microstructure response through a functional form of jamming distance.

4.1. Introduction

The rheological properties of colloidal suspensions are a consequence of complex interplay between the Brownian and hydrodynamic forces between particles in the system. In colloidal suspensions where particles interact through near hard sphere potential the rheological properties are dictated by the excluded volume effects, which is a function of the suspension volume fraction (ϕ) and the hydrodynamic contribution from the suspended solvent [1]. Even in a fluid state (at $\phi < 0.40$), such suspensions are characterized by a shear modulus due to the transient contacts or bonds formed as a consequence of the close proximity of particles and the Brownian fluctuations in the suspension system [2]. As the suspension ϕ increases, the environment around particles become crowded, arresting the Brownian motion resulting in contribution to the dynamics and rheological properties from additional parameters such as particle geometry. Understanding the effect of crowding-induced parameters to predict the suspension elasticity is important in fields ranging from detecting cancer cell dynamics [3] to predicting geological phenomena in advance [4].

Stokes-Einstein-Sutherland diffusivity predicts the diffusion coefficient (D_0) in dilute suspensions ($\phi < 0.05$) as $D_0 = k_BT/6\pi\eta a$, where k_BT is the thermal energy, a is the particle radius, and η is the suspended solvent viscosity. As ϕ increases, the dynamics in concentrated colloidal suspensions are characterized by two relaxation modes: short time and long time. The former is governed by the hydrodynamic interactions while the latter is a consequence of cage rearrangement mechanism at longer timescales. Short time relaxation in colloidal dynamics is characterized by short time translational (D_s^t) and rotational diffusion coefficients (D_s^r). Stokesian Dynamic simulations, incorporating hydrodynamic interactions, and experiments on smooth colloidal particles concluded that both D_s^t and D_s^r remain uncoupled up to $\phi \leq 0.50$ [5,6]. At $\phi > 0.50$, experiments on suspensions containing smooth colloidal particles are able to decouple D_s^t and D_s^r using estimations of mean-square displacement (MSD) and mean-square angular displacement (MSAD), respectively [5].

Long time relaxation in colloidal dynamics is characterized by the respective diffusion coefficients for translational (D_∞^t) and rotational (D_∞^r) modes. The long-time diffusivity parameters characterizes the ability of a particle to escape out of the cage formed by its own neighbors as the colloids experience crowding with increasing ϕ. Through scaling arguments, simulations were able to predict D_∞^t as a product of D_s^t and the effect of change in microstructure due to long-time diffusion, up to $\phi \leq 0.50$ [7]. For smooth spheres, $D_\infty^t \approx D_\infty^r$ due to minimal effect of hydrodynamics on rotational motion. The effect may not be same in the spherically symmetric colloids with surface roughness because in dense suspensions with geometric asperities create hydrodynamic resistance for free rotation. The slowdown of the short-time rotational diffusion coefficients in suspensions of rough colloids of poly(methyl methacrylate) (PMMA) colloids in index and density matched solvent mixture at $\phi \geq 0.35$ was reported by Hsiao et al. [8]. Since the suspension elasticity is inextricably linked to the dynamics [9], linear viscoelasticity measurements of suspensions containing smooth and rough colloids may decouple the effects of roughness on dynamics and thus the rheological properties.

Recent studies with experimental systems with rough colloids have shown to modify shear thickening behavior [10,11], form low-dimensional fractals and suppress crystallization [12]. The surface asperities in rough colloids exhibit different lubrication interaction due to additional tangential interaction component [10,13]. Total suspension stress is characterized by additive contributions from suspending fluid and colloidal particle. The particle contributions come from hydrodynamics and interparticle stresses. In dense suspensions, the rough particles modify the near-field hydrodynamic interactions and thus exhibit different cage dynamics at high ϕ values compared to suspensions with smooth colloids. Thus, it is important to understand the effects of surface roughness as suspension ϕ on the dynamics and elasticity of the suspensions.

In this work, we investigate the effects of surface roughness on the linear viscoelastic properties of dense colloidal suspensions. Simulations in the high frequency regime suggests that colloidal particles with surface modification can decouple the effects from lubrication “contacts” that reduce the particle mobility and the diffusional boundary layer formed in pure hard sphere interactions [14]. Using sterically stabilized PMMA smooth and rough colloids suspended in index matched solvent squalene, that exhibit hard sphere interactions, we decouple the sole contribution of the constitutive particle roughness to suspension elasticity. We use the small amplitude oscillatory measurements to perturb the near-equilibrium microstructures of suspensions containing smooth and rough colloids at various ϕ values.

4.2. Materials and Methods

4.2.1 Colloidal Synthesis and Characterization

We use in-house synthesized poly(hydroxystearic acid)-*grafted*-poly(methylmethacyrylate) (PHSA-*g*-PMMA) colloids for our linear viscoelastic studies reported here. Smooth PHSA-*g*-PMMA microspheres were synthesized using dispersion polymerization of PHSA-gycidyl methacrylate-methyl methacrylate (PHSA-GMA-MMA) co-block polymer with 2-azobisisobutyronitrile (AIBN) as the free radical initiator and MMA as the monomer. We add fluorescent molecule, Nile Red, to visualize the suspension samples using confocal microscopy. Additionally, the rough colloids are synthesized by adding crosslinker, ethylene glycol dimethacrylate (EGDMA), during the dispersion polymerization reaction. Our earlier study indicates that the steric polymer brush (PHSA) is of 10-15 nm in length [15]. The synthesized particles are stored in stock solution and is further solvent transferred to an index-matching solvent squalene ($n_{\mathrm{sq}} = n_{\mathrm{PMMA}} = 1.49$). Index matching serves two purposes: (a) minimizes the van der Waals attraction between the microspheres thus by ensuring hard sphere interactions and (b) reduces the background scattering during fluorescent imaging.

Since the particle swell in solvent squalene, we estimate the particle diameter from confocal images. Due to swelling issues, we do not estimate the roughness via atomic force microscopy (AFM) since the 3D structure does not reflect in the suspension squalene. Instead, we estimate a 2D circularity parameter (ψ) and average them for 100 independent 2D images from confocal microscopy for each particle type. The parameter ψ is defined as $\psi = 4A_p / P_p^2$ where Ap is the maximum 2D area of the particle and Pp is the perimeter corresponding to Ap. We obtain ψ for smooth and rough particles as 0.99±0.01 and 0.87±0.03. Effective particle diameter for rough particle is then calculated using the expression $a_{eff} = \sqrt{A_p / \pi}$. In this study we use smooth particles of $2a = 1.50$ µm ± 4% and rough particles of $2a_{eff} = 1.55$ µm ± 5%. Scanning electron micrographs of the particles are provided in Fig. 1.

Squalene and PMMA particles are not density matched ($\Delta\rho \approx 0.322$ kg/m^3) and this enables centrifugation of suspensions to form random packing. Centrifugation at 1500g eliminates crystallization and for smooth particles suspensions we have shown that PHSA-*g*-PMMA are nearly frictionless and where they pack maximum ≈ 0.64 [15]. We dilute the suspensions from the centrifuged sediment to required ϕ. We image the quiescent suspensions under confocal microscope, and we estimate the diluted ϕ using the formula, $\phi = \dfrac{4/3\pi a_{eff}{}^3 N_p}{V_{box}}$, where N_p is the number of particle centroids obtained via image-processing of a 3D box of volume V_{box} [16]. A similar procedure is adopted for rough particle suspensions.

4.2.2 Rheological Measurements

We perform all our experiments on a stress-controlled rheometer (TA Instruments, DHR-2) using a 50mm serrated cone and plate geometry. We perform strain sweep experiments by varying γ from 0.01% to 100%, holding the frequency at 1 rad/s. The frequency sweep experiments are conducted in the linear viscoelastic regime after identifying the linear regime in each case of smooth and rough colloidal suspensions.

After loading and prior to every experiment set, all the suspensions are conditioned at room temperature for 60 s to remove any prior shear-induced microstructural changes. Suspensions of smooth and rough particles are prone to shear thickening readily during the protocol of lowering the top geometry. To avoid such issues, for geometry heights < 1cm, we lower the top geometry 10 μm per step while monitoring the normal force at the same time.

4.3 Results and Discussions

4.3.1. Linear viscoelastic measurements

The linear regimes for the suspensions of both smooth and rough particles are identified by performing strain amplitude sweeps at an oscillation frequency at a constant amplitude of 1 rad/s. The strain sweep experiments were performed at a frequency of 1 rad/s on suspensions of ϕ ranging from 0.45 – 0.62 in the case of smooth particle suspensions and 0.45 – 0.56 in the case of rough particle suspensions. The results for the dependence of viscous ($G'(\omega)$) and elastic moduli ($G''(\omega)$) as a function of applied strain for suspensions of smooth and rough particles are shown in Fig. 2(a) and 2(b), respectively. In both the cases, we observe that *G'(ω)* and *G''(ω)* values remain independent of the applied strains at low to moderate values. For smooth colloidal suspensions, the highest possible value of strain at the onset of nonlinearity reduces with increasing ϕ, which corroborates earlier result [17]. In contrast, this distinction is not clear in suspensions with rough colloids. One plausible explanation is the similar scale of local dissipation at $\phi > 0.53$ for rough due to the rotational constraints exhibited by the rough particles in the suspension.

At low strains, suspensions exhibit elastic behavior and at higher strains the response is dominated by viscous dissipation. We observe that, in general, for $\phi \leq 0.50$, the *G'(ω)* values are lower than the *G''(ω)* values. This result parallels the data reported earlier in the literature for silica colloids dispersed in ethylene glycol [17]. In smooth colloidal suspensions, for $\phi \leq 0.50$, the dissipation is primarily viscous in nature and similar trend is observed in suspensions containing rough colloids. By contrast smooth particle suspensions at $\phi > 0.57$ is predominantly elastic and the result is qualitatively similar in rough colloidal systems. Quantitatively, the elastic response of rough particle suspensions is observed to be 10^3 times that observed in the suspensions containing smooth colloids. In both types of suspensions, we identify the strain value, where suspensions lie in their respective linear regime, to be at $\gamma \approx 0.5$ %.

The frequency dependence of the viscoelastic moduli on the suspensions of smooth and rough particles are shown in Figure 4.3 and Figure 4.4, respectively. To compare the results between two types of particle suspensions, both axes are normalized. The frequency is non-dimensionalized using the oscillatory shear Peclet number (Pe_ω) defined as $Pe_\omega = a_{eff}{}^2\dot{\gamma}/D_0$ where a_{eff} is the effective particle radius, $\dot{\gamma}$ is the shear rate ($\dot{\gamma} = \omega/2\pi$) and D_0 is the short-time diffusion coefficient which is ϕ-independent. The value of D_0 is obtained using the expression $D_0 = k_BT/6\pi\eta_s a_{eff}$, where η_s is the solvent viscosity (0.012 Pa.s) and other terms are defined earlier in the paragraph. The moduli, *G'(ω)* and *G''(ω)* scales with the thermal energy in the suspension system set by k_BT and a_{eff}.

The change in *G'(ω)* and *G''(ω)* on the applied frequency in smooth colloidal suspensions is shown in Figure 4.3(a) and 4.3(b), respectively. At ϕ = 0.45 and 0.50 and $Pe_\omega \geq 10^3$, the suspensions behave as model Maxwell fluids with $G' \sim \omega^2$ and $G'' \sim \omega$. For $\phi \geq 0.58$ the suspensions display *G'(ω) > G''(ω)* at lower *ω*. At moderate *ω*, there is a high frequency crossover point beyond which both *G'(ω)* and *G''(ω)* rise sharply. The frequency dependence of *G'(ω)* and *G''(ω)* on suspensions of rough colloidal suspensions is shown in Figure 4.4(a) and 4.4(b), respectively. Similar Maxwellian scaling, as reported earlier in smooth colloidal suspensions, is observed in rough particle systems at ϕ = 0.45 and 0.50. The most interesting observation is the increase in *G'(ω)* and *G''(ω)* at $\phi \geq 0.54$. The *G'(ω)* value is frequency independent, reminiscent of a high-frequency plateau modulus observed in compressed emulsions [18], and the magnitude is ~10^3 higher than that reported for smooth particle suspensions. We observe the order of magnitude increase in *G''(ω)* is same as that of the *G'(ω)*. In contrast to smooth particle suspensions, *G''(ω)* in suspensions containing rough colloids exhibit a reproducible minimum and then slowly increases. This behavior of dramatic jump in *G'(ω)* and *G''(ω)* is a novel observation in colloidal rheology behavior in the linear regime.

4.3.2 Viscoelastic spectrum for colloidal suspensions

To further understand the unusual observation in the frequency dependence of *G'(ω)* and *G''(ω)* on the type of particle suspension and decouple the effect of surface roughness on linear viscoelastic properties, we construct a master viscoelastic spectrum combining our data of smooth and rough colloidal suspensions. The method employed here is the time-ϕ superposition principle where the curves obtained earlier in Figure 4.3 and 4.4 are shifted with respect to time (Pe_ω) in the x-axis and moduli (function of ϕ in the y-axis. The shift factors are denoted as α and β in x- and y-axis, respectively. The method employed here assumes that the time- and ϕ-dependence are equivalent for viscoelastic materials and thus the shift factors simultaneously shift $G'(\omega)$ and $G''(\omega)$, irrespective of particle type, for a given ϕ.

The viscoelastic spectrum for a range of colloidal suspensions is shown in Figure 4.5. For convenience, we divide the spectrum into two halves. The first regime is $10^2 < \alpha.Pe_\omega < 10^5$ and the second regime is for $\alpha.Pe_\omega > 10^5$. The first regime comprises of lower frequencies where the moduli for our smooth and rough particle suspensions, for $\phi \leq 0.50$, fit the scaling for a viscoelastic fluid. We take smooth suspensions at $\phi = 0.50$ as our reference and the viscoelastic curves suspensions at ϕ values of 0.45 and 0.50 are shifted accordingly. For small amplitude oscillatory experiments, the frequency dependencies of the viscoelastic shear moduli (G' and G'') are modelled as:

$$G'(\omega) = G\frac{(\omega\tau_{rel})^2}{1+(\omega\tau_{rel})^2} \text{........................(1)}$$

$$G''(\omega) = G\frac{\omega\tau_{rel}}{1+(\omega\tau_{rel})^2} \text{.......................(2)}$$

Here, G is the relaxation modulus (Pa) and τ_{rel} is the timescale of relaxation (s) which is determined as the inverse of the low crossover frequency. The frequency-dependent viscoelastic moduli of smooth and rough particle suspensions fall on the same curve as the shifted Maxwell model curve. At low frequencies, both rough and smooth colloidal suspensions show expected terminal region scaling with $G' \sim \omega^2$ and $G'' \sim \omega$. This result amplifies our earlier observation that there is little to no difference in the viscoelastic behavior between suspensions of smooth and rough particles at $\phi \leq 0.50$.

The second regime consists of moderate and high frequency behavior, which are not described in the Maxwell fluid formalism. In general, this regime is characterized with higher elastic component, which changes at very high frequencies. We observe that with suitable shift factors the viscoelastic behavior of dense suspensions that comprise of rough and smooth colloids forms a master curve as shown in Figure 4.5. Since no continuous data from low-frequency to medium-frequency regime was available, the reference for the second regime started where the data matched with the high-frequency Maxwell model regime. This may introduce error in shift factor α of magnitude ±2, which is much smaller considering the orders of magnitude of α in the spectrum.

4.3.3 Decoupling the effects of geometric frustration in the linear viscoelastic regime

Further analysis of the shift factors is necessary to understand the effect of surface roughness on the viscoelastic properties on the dense colloidal suspensions. We plot the shift factors α and β as a function of ϕ, as shown in Figure 4.6a and 4.6b, respectively. The data show that for $\phi \leq 0.50$ the shift factors for both type of suspensions are similar in magnitude and they are around unity. This might be an artefact of choosing the reference as smooth suspension at ϕ = 0.50. For $\phi > 0.50$, the shift factors vary in magnitude between suspensions of smooth and rough colloids. To further understand the effect of the shift factors we investigate the effect of the ratio of the shift factors α/β with the suspension ϕ.

The variation of shift factor ratio, α/β with respect to ϕ is shown in Figure 4.7(a). At $\phi \leq$ 0.50, α/β is in the order of 1 but at higher ϕ values the ratio is the order of $\sim 10^6$. This behavior is seen in both smooth and rough particle suspensions. We extend the recent work in exploring jamming distance as a design parameter in suspension flow to investigate this behavior. Figure

4.7(b) shows α/β as a function of the distance from jamming ($\Delta\phi/\phi_{max}$) which is defined as (ϕ_{max} - ϕ)/ϕ_{max} where ϕ_{max} is the maximum flowable ϕ before shear jamming. In our suspension systems we estimate ϕ_{max} through unperturbed sedimentation for a period of two months under gravitational stress. We estimate the ϕ_{max} for our smooth particle suspension as $\approx$ 0.64 and rough particle suspension as $\approx$ 0.57.

In Figure 4.7, we observe that the smooth and rough particle suspensions show similar behavior of α/β which is independent of $\Delta\phi/\phi_{max}$. The discontinuity is observed around $\Delta\phi/\phi_{max} \approx 0.1$. For smooth colloidal suspension, this corresponds to $\phi \approx 0.58$. Scattering experiments with same particle system have shown that the glass transition volume fraction (ϕ_g) occurs between 0.574 and 0.581 [19]. Since the linear viscoelastic behavior is a function of small perturbations, we believe that the discontinuity observed in α/β and $\Delta\phi/\phi_{max}$ is a manifestation of the inherent phase behavior, with respect to the suspension crowding with increasing ϕ and the associated dynamic arrest related the suspension ϕ_g, of the colloidal system. This allows us to comment on a ϕ_g estimate for the rough particle system. Similar calculations estimate $\phi_g \approx 0.51$. In Figure 4.7, we do not have any concrete evidence for ϕ_g value for rough particle system other than the preliminary estimation. The gravitational Peclet number ($Pe_g = 4\pi a_{eff}^4 \Delta\rho g/3k_BT$, where $\Delta\rho$ is the density difference between colloid and the suspension, and g is the acceleration due to gravity) $Pe_g > 1$ for our particle system in squalene precludes us from performing dynamics on quiescent suspension and estimate the mean-square displacement at high ϕ values since the particle settle before reaching the α-relaxation timescales around ϕ_g.

Analogous with time-temperature superposition principle in polymer melts, the horizontal shift factor (α) corresponds to the shear rate dependent diffusion coefficient i.e. the larger the α value, the easier it is to jump from a localized cage [20]. For $\phi \leq 0.50$, there are no caging effects as the system is still ergodic in nature. At the same Pe_ω and at respective $\phi > \phi_g$, $\alpha_{\mathrm{smooth}} > \alpha_{\mathrm{rough}}$ indicates that the shear-induced jump from a cage is easier for a smooth particle compared to its rough counterpart. Lower hydrodynamic resistance and negligible rotational constraints enable smooth particles to escape local cages at shorter time scales than the rough particles. The vertical factor β is associated with the intra-cage displacement prior to cage release [20]. A larger β is indicative of a greater amount of intra-cage free volume available and therefore more efficient particle rearrangements. Lower α and β factors for rough particle suspensions than smooth ones at same ϕ values suggest that the effective free volume available for motion in rough particle suspensions is severely restricted causing the jump in elastic modulus.

4.3.4 Effective suspension temperature and associated moduli scaling

For an atomic liquid, the storage modulus (same as G') scales with an effective system temperature (T_{eff}) and effective particle radii (a_{eff}) as $G' \sim T_{eff}/a_{eff}$. In colloidal systems, the T_{eff} term is given by the Brownian energy scale, k_BT. As suspension ϕ increases, particles experience the near-field and far-field hydrodynamics in addition to the caging effects and close to ϕ_g and beyond long-time diffusivity is inhibited and particle remain trapped in transient cages [21]. This is manifested as a jump in viscosity in atomic liquids [22] and the presence of a yield stress in dense colloidal suspensions [23]. In our case, Brownian timescale is same order as the sedimentation timescale (Pe_g in the order of 10^0), the effects become more pronounced. We study the effect of G' as a function of distance to jamming for three different Pe_ω values: 10, 10^2, and 10^3, as shown in Figure 4.8. As observed before, the overall behavior is divided into two regimes at $\Delta\phi/\phi_{max} \approx 0.1$. At $\Delta\phi/\phi_{max} < 0.1$ iso-Peclet data shows a scaling of -1 where as $\Delta\phi/\phi_{max} > 0.1$ does not show any scaling. The data at $\Delta\phi/\phi_{max} < 0.1$ is a consequence of the reduction in effective temperature of the suspension system above ϕ_g.

A scaling of -1 between $G'a_{eff}/k_BT$ and $\Delta\phi/\phi_{max}$ means that the effective system temperature or the reduced thermal energy scales as $k_BT/(\Delta\phi/\phi_{max})$. This means that in linear viscoelastic measurements, the suspension elasticity and the associated dynamics becomes important $\Delta\phi/\phi_{max} < 0.1$. Figure 4.8 shows that, for $\Delta\phi/\phi_{max} < 0.1$, this holds true for both the suspension types and at Pe_ω values spanning three orders of magnitude. The reduced thermal energy due at $\phi > \phi_g$ is a direct effect of the cease in Brownian motion and local transient cage formation. This means that when $\Delta\phi/\phi_{max} > 0$, $G'a_{eff}/k_BT$ should be independent of $\Delta\phi/\phi_{max}$ but we observe this only at $Pe_\omega = 10^3$. The viscous moduli being dominating at $\phi \leq 0.50$ might be a reason why we do not observe any correlation of elastic moduli with respect to jamming distance. Additionally, we observe the discontinuity in elastic moduli in rough particle suspensions compared to smooth particle suspensions at $\Delta\phi/\phi_{max} > 0.1$. Similar discontinuity in shear modulus was observed in simulations of frictional grains at low strain amplitudes under oscillatory shear protocol [24].

These results show that the geometric frustration induced by the surface roughness further reduces ϕ_g in suspensions with rough particles. The results point to a new scaling of the viscoelastic moduli between ϕ_g and ϕ_{max} by taking into account the reduced thermal energy, $k_BT\ (\Delta\phi/\phi_{max})^{-1}$. Physically, the result captures the drastic reduction in suspension dynamics at $\phi > \phi_g$ by rescaling the thermal energy by a factor of $(\Delta\phi/\phi_{max})^{-1}$.

4.4 Conclusions

We investigated the effect of surface roughness on the linear viscoelastic rheology of dense colloidal suspensions. Suspensions of rough colloids exhibit viscoelastic moduli, $G'(\omega)$ and

$G''(\omega)$, orders of magnitude higher than the suspensions of smooth colloidal particles. The microstructural explanation for this phenomenon is that the surface anisotropy constraints the rotational motion in rough colloids, modifies the near-field hydrodynamics, and reduces the effective free volume available in the suspension, particularly close to jamming at $\Delta\phi/\phi_{max} < 0.1$. We quantify this reduction in free volume through the shift factors α and β used in frequency-ϕ superposition. Furthermore, the scaling of elastic moduli over three orders of Pe_ω proves that, for $\Delta\phi/\phi_{max} < 0.1$, the elastic modulus should be scaled with a factor that takes into account the reduction in thermal energy of suspensions.

Earlier work indicates that slow clusters contribute to the bulk elasticity in dense colloidal glasses [25]. Visualizing single particle dynamics using a confocal rheometer may point to similar correlated clusters in rough suspensions that form percolations with minimum contacts that impart bulk elasticity orders of magnitude higher than smooth colloidal suspensions. This would enable understanding phenomena that require low perturbation to respond, especially in cases of geological flow phenomena where the frictional materials that inherently creep exhibit glassy behavior [4].

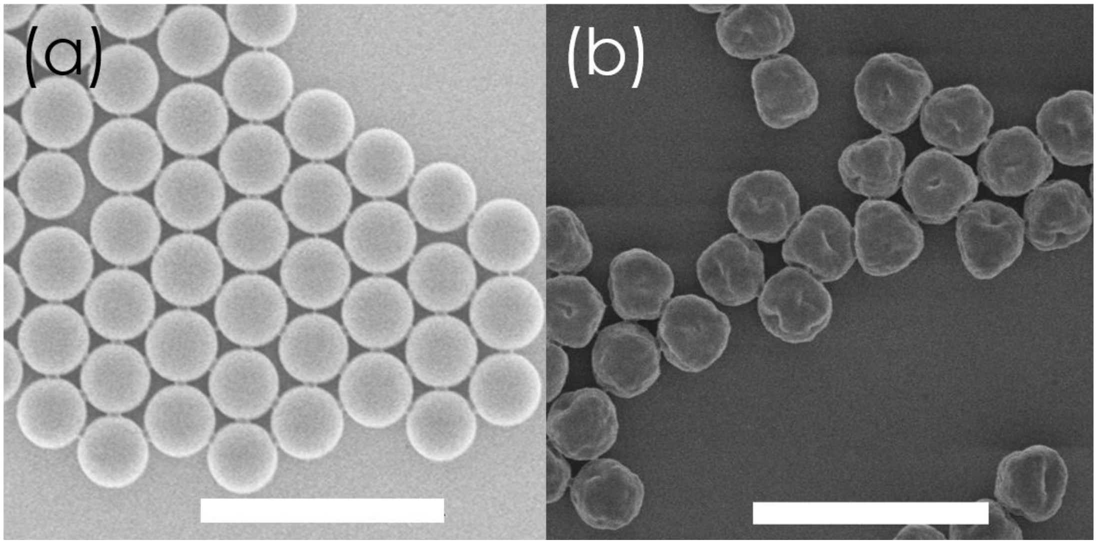

Figure 4.1 | Particle images. Scanning electron micrographs of (a) smooth and (b) rough particles. Scale = 5 μm.

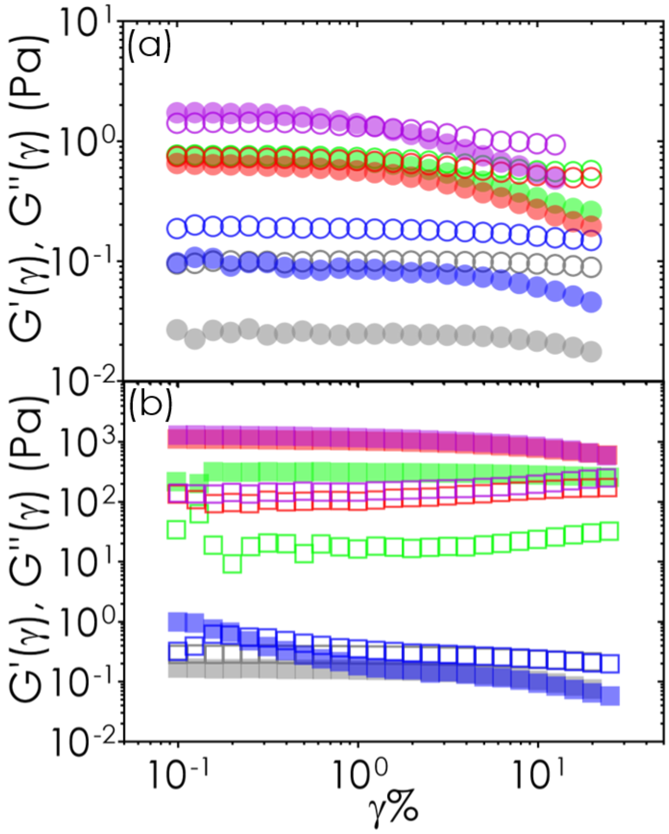

Figure 4.2 | Estimating the linear regime. The elastic (*G'*, filled) and viscous (*G''*, unfilled) moduli of suspensions containing (a) smooth and (b) rough particles as a function of applied strain. The experiments are performed at a constant frequency of 1 rad/s. (a) In smooth particle suspensions, the ϕ values are 0.62 (pink), 0.59 (red), 0.58 (green), 0.50 (blue), and 0.45 (grey). (b) The data set are plotted for rough colloidal suspensions of ϕ values: 0.56 (pink), 0.55 (red), 0.54 (green), 0.50 (blue), and 0.45 (grey).

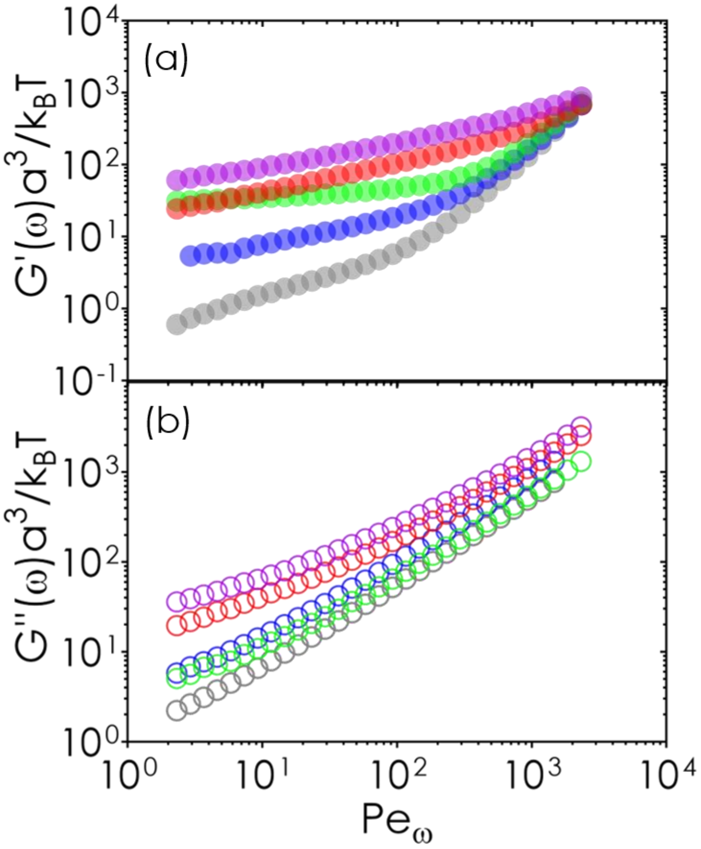

Figure 4.3 | Viscoelastic moduli in suspensions of smooth colloids. The dependence of (a) elastic (*G'*, filled) and (b) viscous (*G''*, unfilled) for suspensions of smooth colloids on applied frequency. The x-axis is normalized by the applied oscillatory shear, particle radius, and thermal energy. The y-axis is normalized by particle radius and thermal energy. The All experiments are performed in the linear regime at strain ~ 0.05%. The suspension ϕ values are 0.62 (pink), 0.59 (red), 0.58 (green), 0.50 (blue), and 0.45 (grey).

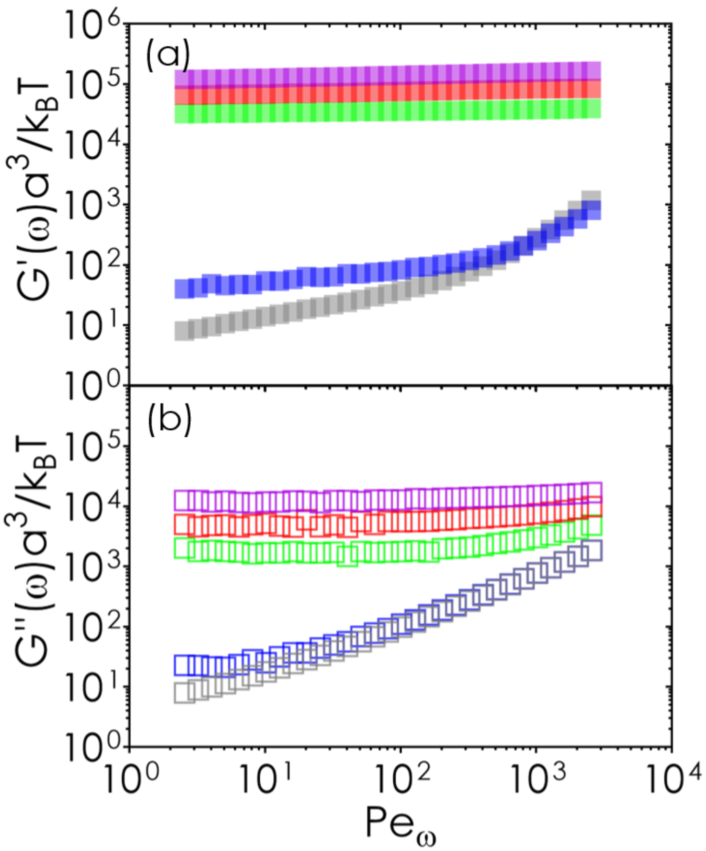

Figure 4.4 | Viscoelastic moduli for suspensions of rough particles. The dependence of (a) elastic (*G'*, filled) and (b) viscous (*G''*, unfilled) for suspensions of rough colloids on applied frequency. The x-axis is normalized by the applied oscillatory shear, particle radius, and thermal energy, and the y-axis is normalized by particle radius and thermal energy. The All experiments are performed in the linear regime at strain ~ 0.05%. The suspension ϕ values are 0.56 (pink), 0.55 (red), 0.54 (green), 0.50 (blue), and 0.45 (grey).

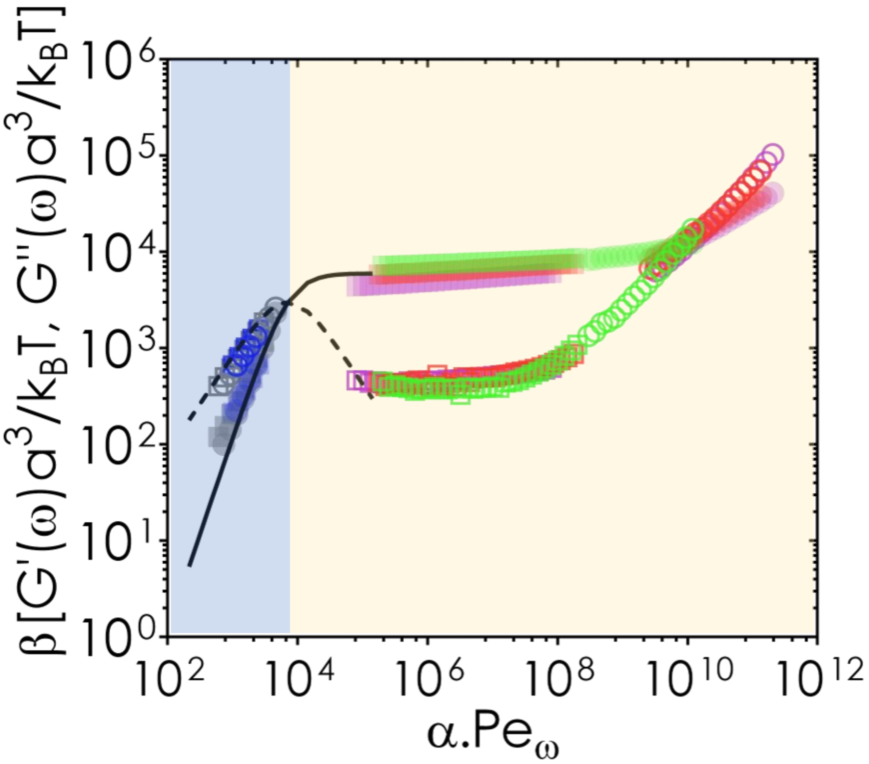

Figure 4.5 | Viscoelastic spectrum for suspensions from time-concentration superposition. The master viscoelastic spectrum (elastic, filled and viscous, unfilled) for suspensions of smooth (circles) and rough (square) colloids. The x-axis is normalized frequency shifted by a factor α and the y-axis is normalized shear moduli shifted by a factor β. The dark line indicates the Maxwell model fit at lower frequencies. The smooth colloidal suspension ϕ values are 0.62 (pink), 0.59 (red), 0.58 (green), 0.50 (blue), and 0.45 (grey). The rough particle suspension ϕ values are 0.56 (pink), 0.55 (red), 0.54 (green), 0.50 (blue), and 0.45 (grey).

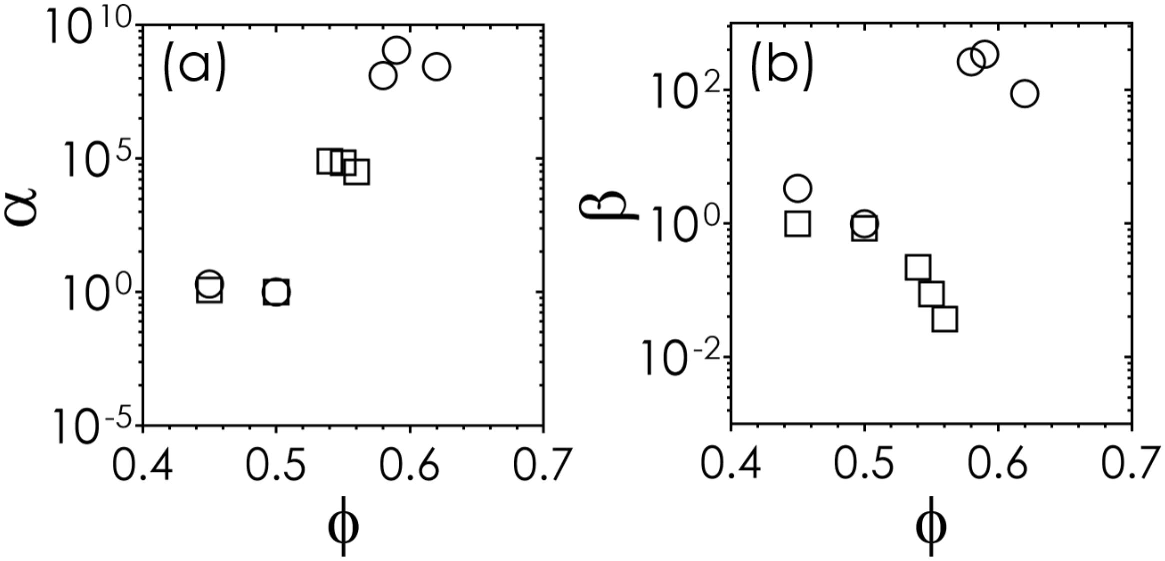

Figure 4.6 | Shift factor variation with concentration. The shift factors (a) α and (b) β plotted against the volume fraction ϕ for suspensions of smooth (circles) and rough (square) colloids.

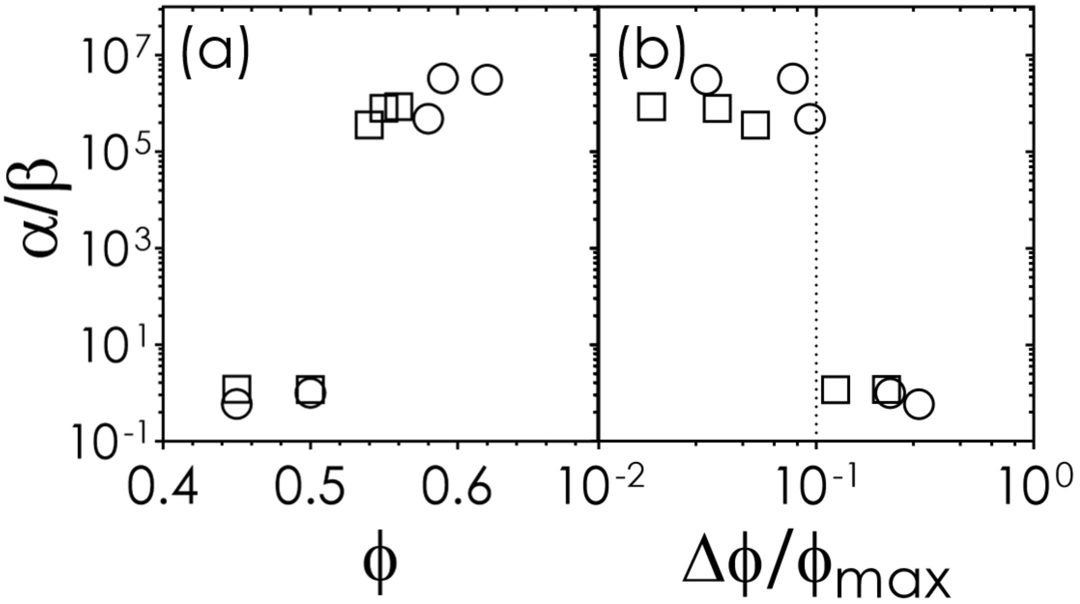

Figure 4.7 | Change in the shift factor ratio with suspension concentration. The ratio of shift factors α/β as a function of (a) ϕ and (b) distance from maximum packing for suspensions of smooth (circles) and rough (square) colloids. The dashed lines in (b) denotes jamming distance of 0.1 as a guide to the reader’s eyes.

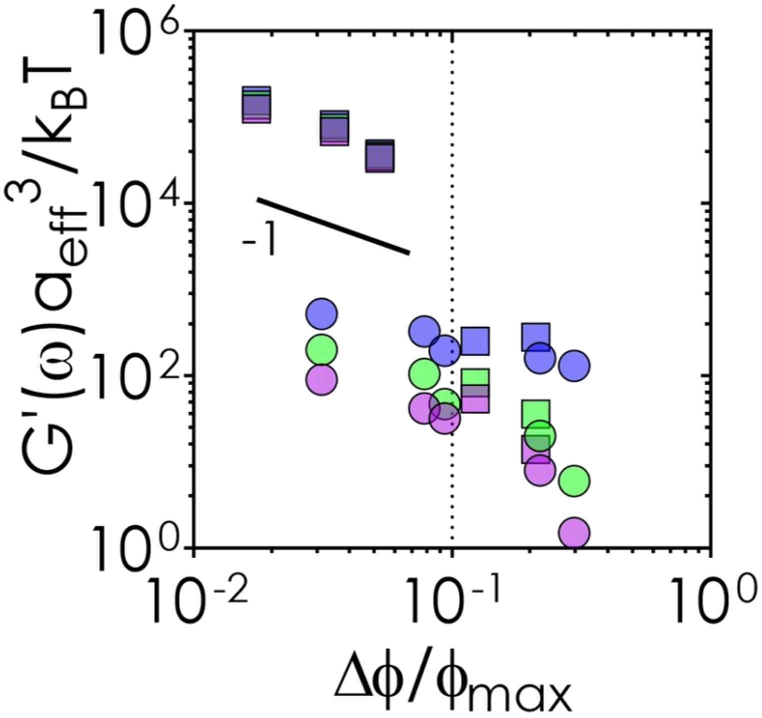

Figure 4.8 | Effective suspension temperature close to jamming point. The dependence of elastic modulus scaled with respect to effective particle radii and temperature on jamming distance for suspensions of smooth (circles) and rough (square) colloids. The colors indicate G' values at various Peclet (Pe_ω) values: $Pe_\omega = 10$ (pink), $Pe_\omega = 10^2$ (green), and $Pe_\omega = 10^3$ (blue). The horizontal dashed line indicates a jamming distance of 0.1.

References

[1] B. Schroyen, C.-P. Hsu, L. Isa, P. Van Puyvelde, and J. Vermant, Physical Review Letters **122**, 218001 (2019).

[2] W. B. Russel, D. A. Saville, and W. R. Schowalter, *Colloidal Dispersions* (Cambridge University Press, Cambridge, 1989), Cambridge Monographs on Mechanics.

[3] D. Bi, X. Yang, M. C. Marchetti, and M. L. Manning, Physical Review X **6**, 021011 (2016).

[4] B. Ferdowsi, C. P. Ortiz, and D. J. Jerolmack, Proceedings of the National Academy of Sciences **115**, 4827 (2018).

[5] K. V. Edmond, M. T. Elsesser, G. L. Hunter, D. J. Pine, and E. R. Weeks, Proceedings of the National Academy of Sciences **109**, 17891 (2012).

[6] R. J. Phillips, J. F. Brady, and G. Bossis, The Physics of Fluids **31**, 3462 (1988).

[7] J. F. Brady, Journal of Fluid Mechanics **272**, 109 (1994).

[8] L. C. Hsiao, I. Saha-Dalal, R. G. Larson, and M. J. Solomon, Soft Matter **13**, 9229 (2017).

[9] T. G. Mason and D. A. Weitz, Physical Review Letters **74**, 1250 (1995).

[10] L. C. Hsiao, S. Jamali, E. Glynos, P. F. Green, R. G. Larson, and M. J. Solomon, Physical Review Letters **119**, 158001 (2017).

[11] C.-P. Hsu, S. N. Ramakrishna, M. Zanini, N. D. Spencer, and L. Isa, Proceedings of the National Academy of Sciences **115**, 5117 (2018).

[12] R. Rice, R. Roth, and C. P. Royall, Soft Matter **8**, 1163 (2012).

[13] S. Jamali and J. F. Brady, Physical Review Letters **123**, 138002 (2019).

[14] R. A. Lionberger and W. B. Russel, Journal of Rheology **38**, 1885 (1994).

[15] S. Pradeep and L. C. Hsiao, Soft Matter **16**, 4980 (2020).

[16] J. C. Crocker and D. G. Grier, Journal of Colloid and Interface Science **179**, 298 (1996).

[17] T. G. Mason and D. A. Weitz, Physical Review Letters **75**, 2770 (1995).

[18] T. G. Mason, J. Bibette, and D. A. Weitz, Physical Review Letters **75**, 2051 (1995).

[19] W. van Megen and S. M. Underwood, Nature **362**, 616 (1993).

[20] A. R. Jacob, A. S. Poulos, S. Kim, J. Vermant, and G. Petekidis, Physical Review Letters **115**, 218301 (2015).

[21] E. R. Weeks and D. A. Weitz, Physical Review Letters **89**, 095704 (2002).

[22] A. Ikeda, L. Berthier, and P. Sollich, Soft Matter **9**, 7669 (2013).

[23] M. Dinkgreve, M. A. J. Michels, T. G. Mason, and D. Bonn, Physical Review Letters **121**, 228001 (2018).

[24] M. Otsuki and H. Hayakawa, Physical Review E **95**, 062902 (2017).

[25] J. C. Conrad, P. P. Dhillon, E. R. Weeks, D. R. Reichman, and D. A. Weitz, Physical Review Letters **97**, 265701 (2006).

CHAPTER 5

Summary and Future Work

5.1 Concluding remarks

The objective of this dissertation was to study the microstructural difference in dense suspensions comprising of smooth and rough colloids with respect to their packing and flow behavior. We achieved this by probing the contact microstructure of model smooth and rough PHSA-g-PMMA suspensions that interact through near hard-sphere interactions. The dissertation focused on linking the microscale behavior to the bulk packing and rheological. The colloidal particle synthesis protocol was optimized in the lab to produce near monodisperse smooth and rough particles. Rough particles were spherically symmetric but exhibited surface anisotropy through varying lengthscales and frequencies of raspberry-shaped structuress. This enabled us to decouple the effects that stem from the restricted rotational (and associated translational) motion of the rough colloids in dense suspensions compared to their smooth counterparts. We used confocal microscope, stress-controlled rheometer, and an in-house assembled confocal rheometer to study these effects.

Earlier linear viscoelasticity studies have shown that colloidal suspensions exhibit stress-bearing properties, even at near-equilibrium conditions. In Chapter 2, we defined a “contact” criterion for quiescent colloidal suspensions to explain the modulus in equilibrium non-flowing colloidal suspensions. We attribute this behavior to the transient Brownian clusters formed in these suspensions owing to their thermal energy scale, k_BT. We defined a “contact” lengthscale for the colloidal particles in these suspensions using arguments from jamming of frictional granular materials. Using 3D confocal microscopy and image processing routines, the average nearest neighbor number, at various lengthscales up to 10% of the average particle diameter, was extrapolated to respective isostatic conditions of the suspensions. The optimized contact criterion was found to include lengthscales involving average particle diameter, steric polymer brushes, roughness scale, and associated polydispersity.

Chapter 3 was focused on designing shear thickening suspensions using a single parameter, the jamming distance. Using suspensions of colloids that exhibited varying surface roughness, we produced steady shear flow curves and observed that there is a universal behavior in the shear thickening strength (defined by the rate of increase of suspension viscosity with increasing applied stress) in these suspensions and their respective jamming distance. We assembled a confocal rheometer in-house and arrested the suspension during shear thickening stress to study the 3D contact microstructure. We found that the "contact" lengthscale obtained from our earlier analysis of quiescent suspensions did not explain the physics behind shear thickening mechanics. At high stresses, colloidal particles in shear thickening suspensions make closer "contacts" than when they are at quiescent states due to the lubrication to frictional transition i.e., high stresses push particles together squeezing the steric brushes and forming lock-and-key structures between rough asperities. To take this into account, we redefined the "contact" lengthscale to the average particle diameter and were able to capture the underlying physics in universal shear thickening behavior of dense colloidal suspensions. Using the redefined frictional "contacts", we estimated the scaled contact deficiency of each suspension type to its respective jamming point. The scaled contact deficit explains a normalized spatial variable that take to account the differences in free volume available for different types of particles under shear. Thus, using arrested 3D contact microstructure we explained the universal correlation between shear thickening strength and jamming distance.

Results from the abovementioned works suggested that the contact microstructure of suspensions with smooth colloids are different from rough colloids, in their quiescent state. This comes from the fact that the isostatic condition, which dictates minimum neighbors for mechanical stability, for the rough particle suspension is lower than suspensions with smooth colloids. Thus, the Brownian suspension stress and associated hydrodynamics differ between these suspensions, especially close to their respective jamming points. We probe this difference using linear viscoelastic experiments which focuses on distorting near-equilibrium microstructures. In linear regime, our small amplitude oscillatory experiments revealed the viscoelastic moduli of rough particle suspensions is 10^3 times higher than that of the smooth colloidal suspensions for the particle same concentration. We owe this difference to the restricted rotational motion of the rough colloids below the jamming distance of 0.1 where we suspect that the cage rearrangement dynamics was not possible in our experimental window. Additionally, we found that rescaling the moduli by the jamming distance at jamming distance values less than 0.1 takes to account the reduced Brownian energy due to suspension vitrification.

5.2 Future work

There is still a significant gap in understanding the effect of surface roughness on dynamics, phase behavior, and viscoelastic properties. Probing real-time microstructure in the suspension is an important step to understand the underlying physics for effective suspension design for desired applications. Experiments exploring fragility of rough glasses, creep studies, depleted gel microstructures etc. will reveal unexplored physics in these systems.

5.2.1 Contact networks in shear thickening

Recently there has been a great interest in understanding the networks formed during shear thickening mechanism [1]. Scattering experiments were able to decouple the effects of surface contact friction by analyzing the change in microstructure anisotropy in the shear plane [2]. During shear thickening, networks break and reform continuously. Our arrested suspension microstructures capture a statistical ensemble of such contact networks formed. Using particle positions obtained using our image-processing algorithms, structural signatures related to shear thickening suspensions can be further probed.

5.2.2 Phase-behavior of rough colloidal suspensions

We have observed that surface roughness modifies the the scaling of contact deficient with respect to the jamming distance. Surface roughness was also shown to suppress crystallization in dense suspensions [3]. Whether rough particle suspensions that interact *via* pure hard-sphere potential ever crystallize? Further studies of the rough particle systems characterizing the change in bond order parameters with time is required to answer few of these questions [4]. Can we say that the suspension preparation protocol decides random close packing in rough particle suspensions? The maximum packing formed by the suspensions of smooth and rough particles can be probed using contact fabrics [5]. What happens if the suspensions are electrostatically stabilized? Will the effects of surface roughness get masked? Many unanswered questions remain with respect to the phase behavior of rough colloidal suspensions. Spherically symmetric but surface anisotropic colloidal particles, that interact via hard sphere potential, form a model experimental colloidal system to investigate the emerging interest in amorphous system behavior, which is currently limited to computer simulations [6].

References

[1] M. Gameiro, A. Singh, L. Kondic, K. Mischaikow, and J. F. Morris, Physical Review Fluids **5**, 034307 (2020).

[2] Yu-FanLee, YiminLuo, TianyiBai, C. Velez, S. C. Brown, and N. J. Wagner, Physics of Fluids **33**, 033316 (2021).

[3] R. Rice, R. Roth, and C. P. Royall, Soft Matter **8**, 1163 (2012).

[4] D. Ganapathi, D. Chakrabarti, A. K. Sood, and R. Ganapathy, Nature Physics **17**, 114 (2021).

[5] J. Liu, W. Zhou, G. Ma, S. Yang, and X. Chang, Powder Technology **366**, 747 (2020).

[6] J. N. Nampoothiri, Y. Wang, K. Ramola, J. Zhang, S. Bhattacharjee, and B. Chakraborty, Physical Review Letters **125**, 118002 (2020).

APPENDIX

Supplementary Information for Chapter 3 “Jamming distance dictates colloidal shear thickening.”

A.1 Flow fit curves from mean-field theory

Predictions of the suspension viscosity from the Wyart-Cates (WC) theory [1] are fitted to the experimental data as solid lines in Fig. 1. The original WC model attributes shear thickening to a change in the contact microstructure. First, in the low-σ regime, hard spheres are frictionless and display a viscosity divergence at $\phi_{max} \approx 0.64$, so long as the particles remain separated in flow. An increasing subpopulation of particles then undergo a lubricated-to-contact transition at $\sigma \geq \sigma^*$, where the fraction of contacting particles is modeled by the sigmoidal form $f(\sigma) = \exp[-(\sigma^*/\sigma)^\gamma]$ and γ is between 0.5 and 1.0 [2,3]. Finally, in the high-σ regime, most of the particles interact through frictional mechanics and the suspension diverges in viscosity at $\phi_{J,f} \approx 0.58$, where the subscript denotes the frictional shear-jammed state. Under shear, these packings become more frictional and jam at even lower volume fractions ($\phi_{max,\mu} < \phi_{max}$, where μ is the interparticle friction coefficient). A spherically symmetric colloid with anisotropic surface morphology imparts different values of ϕ_{max} and $\phi_{J,f}$ as opposed to a smooth, frictionless hard sphere. From the perspective of the WC model, dense suspensions shear thicken because of a transition between a packing with viscosity that diverges at ϕ_0 to a new packing that diverges at ϕ_m. The WC model generates flow curves through the following empirical relations:

$$\sigma = \lambda\left(\phi_J\left(f\right) - \phi\right)^{-2}\dot{\gamma} \tag{A.1}$$

$$\phi_J\left(f\right) = \phi_{\max}(1 - f) + \phi_{J,f}\, f \tag{A.2}$$

The values for ϕ_{max} are 0.64 and 0.54 for smooth and rough particles, respectively. These values are obtained independently from the low-shear viscosity divergence and sedimentation experiments performed over three months. The estimated values for $\phi_{J,f}$ are obtained using a similar viscosity divergence method but at the shear-thickening plateau ($\sigma >> \sigma^*$). Since we are unable to observe this plateau using our experimental setup, for smooth colloids, we assumed $\phi_{J,f} = 0.58$

following the original model. Our system gives the high-shear viscosity divergence at $\phi_{J,f} = 0.49$. The values of f are varied from 0 to 1 as described by sigmoidal model above. The value of λ in the above equation is an empirical fitting parameter which we assume to be unity. The WC model does not fit the experimental flow curves at $\phi > \phi_{J,f}$ because it predicts S-shaped flow curves ($\beta > 1$), which we do not observe in experimental systems. This is likely due to the overdamped motion of the colloids used in this study, which precludes the presence of inertial flows even at the highest applied shear stresses.

A.2 Estimating jamming points (ϕ_{max}) for colloidal suspensions

Superimposing our experimental values of ϕ_{max} and the corresponding $<z>$ onto the simulation data of Singh *et al.* [4] suggests that our rough colloids can be modeled as particles with significant sliding constraints, quantified using μ_s and μ_r values (Figure A.2).

.

A.3 Sample immobilization and visualization with confocal microscopy

Rheology is performed using a 20 mm parallel-plate geometry and cover slip with thickness #1.5. Suspension samples are incorporated with 5 wt% photocrosslinker mixture (2 wt% photoinitiator phosphine oxide, 8 wt% photopolymer trimethylolpropane triacrylate-TMPTA, and solvent diisooctyl phthalate). Good agreement in the radial distribution function, $g(r)$, for suspension with and without the photocrosslinker (Figure A.3(a)) shows that suspension doped with photocrosslinker mixture retain their hard sphere behavior. We estimate the mean-squared displacement $<\Delta r^2(t)>$ of a representative photopolymerized suspension. As shown in Figure A.3(b), the noise floor is estimated to be 0.0012 μm^2 which is $\approx$ 0.1% of $(2a)^2$. This shows that the vibrations of the confocal rheometer is not significant enough to affect the particle centroid identification in the photopolymerized sample and the <z> obtained from image processing routine. Sample z-projections of the dynamic microstructure in suspensions of smooth and rough colloids is shown in Figure A.4. Centroid identification from similar arrested 3D image stacks enable us generate the respective dynamic contact networks by defining the contact criterion as $2a_{eff}$.

A.4. Details of the DPD simulations

Simulations are done *via* the HOOMD-Blue simulation toolkit where the roughness of different particles is modeled by randomly placing asperities with their centers located on the periphery of the base particle. The base particles are modeled as near hard spheres covered by these smaller patchy asperities, and in our setting we choose the asperity radius to be $0.1a$, where a is the radii of the base particles [5]. The main simulations are based upon a core-modified Dissipative Particle Dynamics (DPD) algorithm [6,7], previously shown to preserve the essential hydrodynamics in dense suspension systems. Over the past two decades, there has been a plethora of research topics that employ DPD as the primary simulation tool [8-10]. DPD is a discrete fluid model, where all particles including the background fluid particles are modeled explicitly and through pairwise interactions. We write the equations of motion for DPD as:

$$m_i \frac{dv_i}{dt} = \sum_{i,i\neq j}^{N_p} \left(F_{ij}^{\ C} + F_{ij}^{\ D} + F_{ij}^{\ R} + F_{ij}^{\ R'} + F_{ij}^{\ H} \right) \tag{A.3}$$

$$\omega_{ij} = (1 - r_{ij} / r_c) \tag{A.4}$$

$$F_{ij}^{\ R} = \sigma_{ij}\omega_{ij}(r_{ij})\Theta_{ij}\Delta t^{-0.5} e_{ij} \tag{A.5}$$

$$F_{ij}^{\ D} = \gamma_{ij}\omega_{ij}^{\ 2}(r_{ij})(v_{ij}.e_{ij})e_{ij} \tag{A.6}$$

$$F_{ij}^{\ C} = \alpha_{ij}\omega_{ij}(r_{ij})e_{ij} \tag{A.7}$$

$$F_{ij}^{R'} = F_0^{R'} e_{ij} \tag{A.8}$$

$$F_{ij}^{H} = \mu_{ij}(v_{ij}.e_{ij})e_{ij} \tag{A.9}$$

The solvent particles in DPD are modeled as soft particles and interact through the first three terms on the RHS of Eq. 3. In equation F_{ij}^{C}, F_{ij}^{D} and F_{ij}^{R} are the pairwise conservative, dissipative, random forces, respectively. Random and dissipative forces together form the canonical ensemble and satisfy the fluctuation-dissipation requirements [11,12]. The random force introduces thermal fluctuations via a random function, Θ_{ij}. This heat is dissipated by the dissipative force acting against the relative motion of particles $v_{ij} = v_i - v_j$ and γ_{ij} is the strength of dissipation, which is coupled with the thermal noise, σ_{ij}. Together these parameters define the dimensionless temperature as $k_B T = \sigma_{ij}^2 / \gamma_{ij}$ and e_{ij} is the unit vector. Conservative force, defines the chemical identity of a particle based on its chemical potential/solubility in the system, through a parameter, α_{ij}. $F_0^{R'}$ is the repulsive force that prevents the colloidal particles to overlap where $F_0^{R'}$ is the repulsion constant and $F_0^{R'} = 500 k_B T / a$ is used for the base-base interactions. Finally, F_H^{ij} is the short-range lubrication force that dissipates the motion of particles through a pair drag term, $\mu_{ij} = 3\pi\mu_0 a_1 a_2 / 2h_{ij}$ based on normal squeezing mode of lubrication. This force enables us to capture the short-range hydrodynamics between the particles, where a_1 and a_2 are the radii of the interacting colloids and μ_0 is the viscosity of the suspending fluid, and h_{ij} is the surface-surface distance between two interacting colloids. Melrose and Ball [13] have shown previously that the tangential mode of lubrication scaling as $\sim \log(1/h_{ij})$ can be ignored compared to the normal mode of lubrication where stresses scale inversely with the separation distance between the particles.

Thus, in this platform, we only consider this normal model of lubrication, squeeze mode, and the tangential motion and hindrance to it naturally comes from the normal interactions between the asperities. We have shown previously that this scheme recovers the same hydrodynamics as a fully resolved Stokesian Dynamics with a complete solution of hydrodynamics for the asperities [14,15]. The hydrodynamic interactions are solved on the asperity-asperity and base-base interactions and not on the asperity-base interaction, because the lubrication forces of high particle size ratio are much weaker than the same size ones [15].

A.5 Statistical testing

Statistical significance of the contact scaling model fit, $\Delta z \sim \Delta\phi^{0.95\pm0.07}$, is conducted using reduced chi-squared parameter ($\bar{\chi}_0{}^2$) defined as:

$$\bar{\chi}_0{}^2 = \frac{1}{N}\sum_{i=1}^{N}\frac{\left(y_i - f(x_i)\right)^2}{\sigma_i^2} \tag{A.10}$$

Here, y_i denotes the experimental data, $f(x_i)$ corresponds to the linear fit model, and σ_i is the standard deviation of the respective y_i values. For Fig. 4b, the number of data points is N = 32 and we obtain a $\tilde{\chi}_0{}^2$ value of 2.12, with the corresponding P value less than 0.005 which indicates that the agreement between experimental observations and corresponding power-law is statistically significant. The error bars in Fig. 4b become increasingly large near jamming, because of the magnified relative uncertainty with respect to $\phi_{J,\beta}$ and $z_{J,\beta}$.

A.6. Contact criterion model for shear thickening suspensions

A prevailing theory that explains shear thickening mechanics is the transition of particle interaction form a lubrication to a frictional flow above the onset stress, σ*, although the origins of this friction are not well understood. The mean-field theoretical description of shear thickening proposed in the WC model suggests that as the suspension shear thickens, due to the increasingly constrained nature of the particles, the maximum possible flowable suspension ϕ_J decreases as a function of σ. As σ increases, the force chains increases in strength transmitting stress between particles thus by increasing the number of transient contacts between them. To capture this physics, we provide two distance-based criteria in order to define "contact" in experimental colloidal systems where Brownian motion and hydrodynamics are present, one for Newtonian flows ($\sigma < \sigma^*$) and one for shear thickening flows ($\sigma > \sigma^*$).

The rationale for using two different contact criteria in our experimental study is that in quiescent and low-stress flows, colloids make transient interparticle contact due to the hydrodynamics induced by Brownian motion, and the suspension supports a macroscopic stress even when no space-spanning force chains are formed. Colloids used in experimental systems are further subject to factors such as steric brush layer, electrostatics, and solvent lubrication film. When the suspensions undergo shear thickening at high stresses, the colloids are pushed by the external flow into near vicinity of one another. The steric layer brush and even the particle itself may become compressed if the local shear stresses are larger than the yield stress of the material.

We define a stress-dependent contact length scale where the average contact number $<z>$ can be computed through a mean-field description using function $\mathbb{F}$. Additional testing is required to understand the function form of $\mathbb{F}$ and thus in our contact model validation we approximate $\mathbb{F} \approx f$, where f is the fraction of colloidal particles that are in frictional contact at a given shear thickening stress, as given in equation (A.2). The nearest neighbor contact is estimated as weighted-average value of the hydrodynamic and frictional contacts as:

$$< z >=< z >_h (1-\mathbb{F})+ < z >_f \mathbb{F} \tag{A.11}$$

Here, <z>$_h$ is the hydrodynamic contact which is obtained at low-shear viscosity $\tilde{\sigma}_{\beta=0}$ using a contact criterion that incorporates length scales associated with surface roughness, steric polymer brush, and associated polydispersities (Δ) [16], while <z>$_f$ is obtained at $\phi_{J,f}$ with contact criterion set as the average particle diameter. Here, $\mathbb{F}$ is an increasing function of the applied stress σ and $\mathbb{F} \in [0,1]$. In our model, we define the contact criterion (r') as: $r' = r/2a_{eff}$ where $r = r(\mathbb{F})$ and $2a_{eff}$ is the effective average particle diameter. The σ-dependent contact length scale r is defined as:

$$r = 2(r_{\text{surface roughness}} + r_{\text{steric brush}}) + \Delta, \text{ when } \sigma < \sigma^* \ (\mathbb{F} = 0) \tag{A.12}$$

$$r = 2a_{eff}, \text{ when } \sigma > \sigma^* \ (0 < \mathbb{F} \leq 1) \tag{A.13}$$

To test the validity of the model and the contact microstructure data used in our studies, we estimate <z>$_f$ in equation S11 using our <z> available at $\tilde{\sigma}_\beta$ for our suspensions. Using the experimental parameters available for the two sets of particles (S- and RK-type) from Supplemental Table 1 and using equation S2, we estimate f = 0.5 and 0.6 for suspensions of S and RK particles at $\tilde{\sigma}_\beta$, respectively. Using equation S11, and the experimental data available (Supplemental Table 1) estimate <z>$_f$ as 3.89 and 2.83 for the suspensions of smooth and rough particles, respectively. Earlier simulations with frictional granular materials have shown a decrease in <z> from 6 to 4 by increasing the interparticle friction (μ_p) from 0 to ∞.

Thus estimation of <z> using our σ-dependent contact length scale suggests that we capture the change from a lubricated state ($\sigma < \sigma^*$, $\phi_{max} \approx 0.64$, and <z>$_{max} \approx 6.0$) to a frictional state ($\sigma > \sigma^*$, $\phi_{J,f} \approx 0.58$, and <z>$_f \approx 3.89$) as the suspension shear thickens. Similarly for suspensions of rough particles, our model captures the transition in the contact microstructure transition the lubricated state below σ^*, where $\phi_{max} \approx 0.54$, and $<z>_{max} \approx 3.88$, to its shear thickening frictional state above σ^*, where $\phi_{J,f} \approx 0.49$, and $<z>_{max} \approx 2.83$).

Table A.1 Input parameters for the contact model

Parameter	Smooth (S)	Rough (RK)
ϕ_{max}	0.64	0.54
$<z>_{max}$	6.01	3.88
$\phi_{J,\beta}$	0.61	0.51
$<z>_{J,\beta}$	4.95	3.25
$\phi_{J,f}$	0.58	0.49

A.7 Change in suspension contact microstructure with shear thickening

The probability distributions of the dynamic contact microstructure, p(z), obtained from both experiments and simulations at $\tilde{\sigma}_\beta$ are shown in Figure A.5. There are two important observations here: (a) the average contact number generally increases with increasing ϕ, which is observed for suspensions of both smooth and rough colloids, and (b) the presence of percentage of particles with zero contacts also increases with increasing ϕ. Figure A.5(a-b) shows that suspensions with smooth colloids have less than 1% of zero contacts at $\Delta\phi/\phi_{\max} \leq 0.23$ ($\phi \geq 0.42$). On the contrary, 5-20% of the rough particles have zero contacts at $\Delta\phi/\phi_{\max} \leq 0.17$ ($\phi \geq 0.45$). This trend is captured by both experiments and simulations which strengthens our comment that the force transmitted per contact is likely higher in suspensions with rough particles than with smooth colloids.

The frictional contacts (when contact criterion is set to $2a_{eff}$) for suspensions containing both smooth (S) and rough (RK) colloids proliferate with increasing applied stress when the suspensions transition from a low-shear viscosity ($\sigma_{\beta=0}$) to a shear thickening regime (σ_β) , as shown in Figure A.6. This transition is accompanied by changes in microstructural anisotropy as particles align along the compressive axis of flow (Figure A.4). Here we quantify the change in $<z>$ alone. The change in probability distributions of frictional $<z>$ for suspensions of both smooth and rough particles between experiments and simulations qualitatively matches with the increasing trend. In both the cases there is an increase in frictional contacts with increasing applied σ. Smooth colloids loses particles of $<z> \approx 2$ and gain particles with $<z> \approx 4$ to 5. On the other hand, rough particles loosed at most one contact and gain $<z> \approx 2$ to 4. Discrepancies between experiments and simulation may arise from factors such as size polydispersity, surface roughness variability, and the errors associated with the correct centroid determination from image-processing routines.

A.8. Axial forces in shear thickening suspensions

The surface tension of the suspension is important in the computation of the first normal stresses (N_1) using a cone-and-plate geometry. Although surface tension effects are usually negligible with standard fluids, dilatant suspensions may contain particles jammed at the surface, which alter the meniscus curvature and significantly decrease N_1 [17]. Since the shape of the meniscus was not monitored in this study, we report only the axial force output from the steady shear measurements in Figure A.7. The data show that the competing effects of dilatancy and surface tension are especially apparent for VR and RK colloids at the highest volume fractions ($\phi \geq 0.46$).

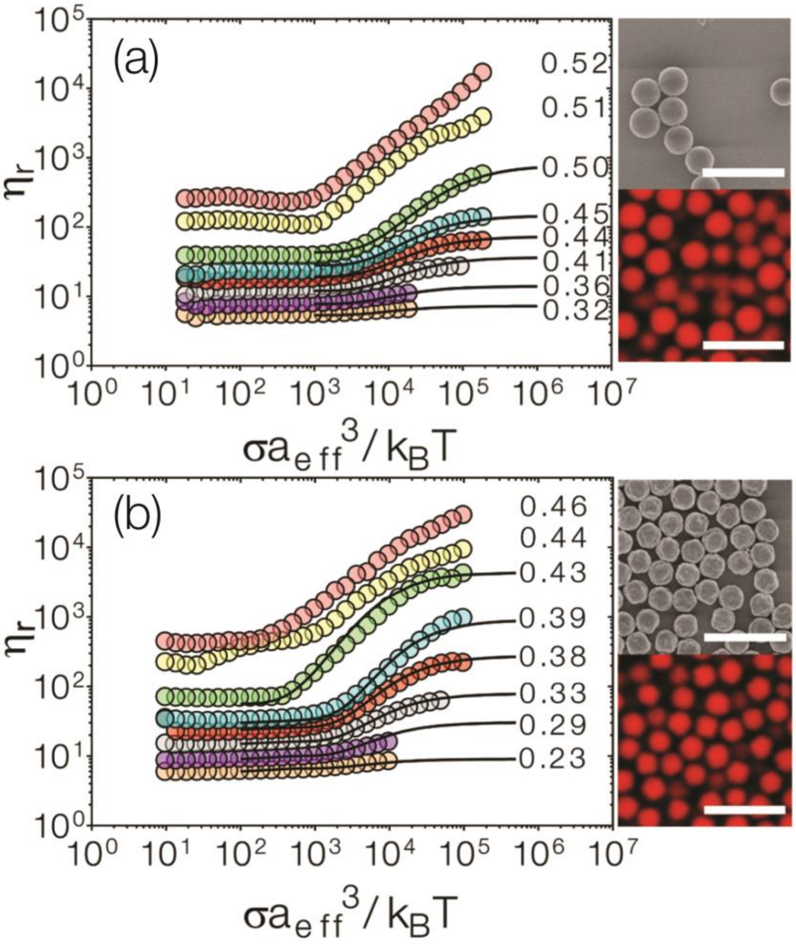

Figure A.1 | Viscosity-stress curves for suspensions of (a) SR and (b) VR colloids. Solid lines are fits with the Wyart-Cates model. The numbers on the side of each curve represent the average estimated ϕ of the respective suspension. Inset: Representative scanning electron micrographs and confocal laser scanning micrographs of colloids. Scale bars = 5 μm.

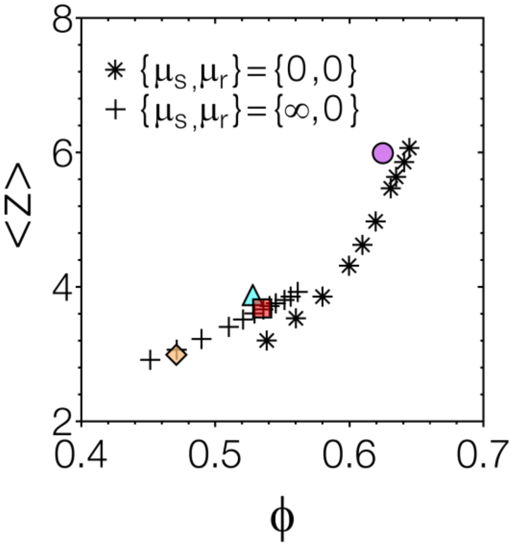

Figure A.2 | Experimental contact number <z> for different suspensions plotted against ϕ. Data are shown for S (magenta circles), SR (orange diamonds), VR (coral squares), and RK colloids (cyan triangles). Simulation data from particles interacting via short-range hydrodynamics, repulsion, and sliding/rolling friction are overlaid in the plot (μ_s = sliding friction, μ_r = rolling friction).

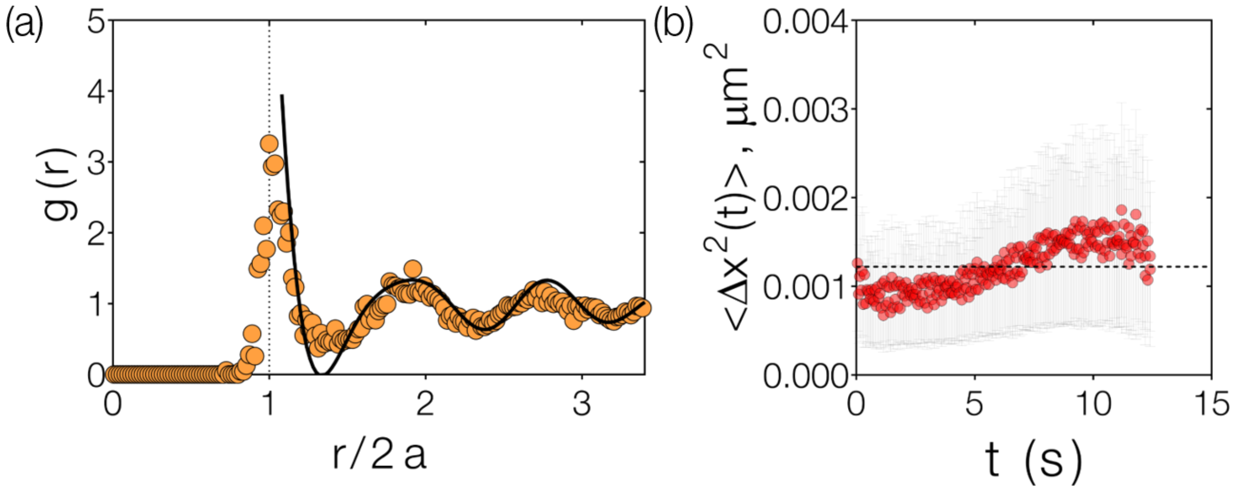

Figure A.3 | (a) The filled circles represent the radial distribution of the smooth colloidal suspension at $\phi = 0.56$. The dark line corresponds to the radial distribution function from classical fluid theory with Percus-Yevick closure that mimics hard-sphere microstructure. The matching of peaks in experimental and theoretical radial distributions show that suspensions retain overall hard-sphere like behavior. (b) Mean-squared displacement of a photopolymerized sample to indicate the noise floor of the confocal rheometer setup.

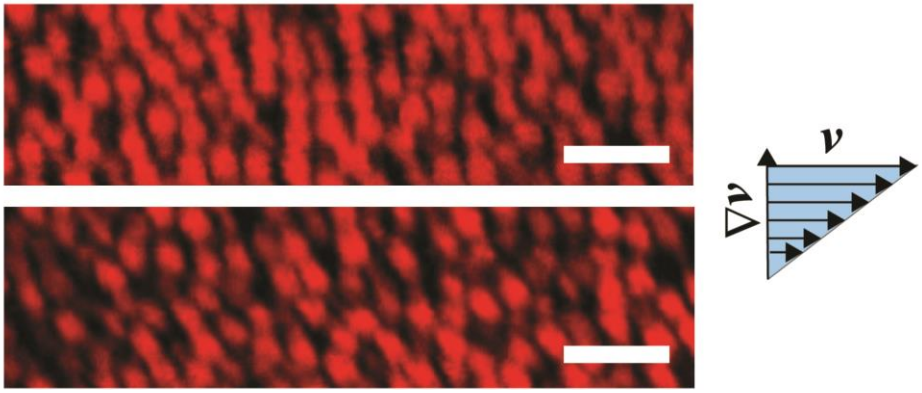

Figure A.4 | The z projection of the arrested dynamic microstructure in suspensions of (a) smooth and (b) rough colloids at $\Delta\phi/\phi_{max} \approx 0.08$ and $\beta \approx 0.95$. Shear direction is shown in the inset and the contact networks are aligned in the compressive axis of the shear. Scale = 5 µm.

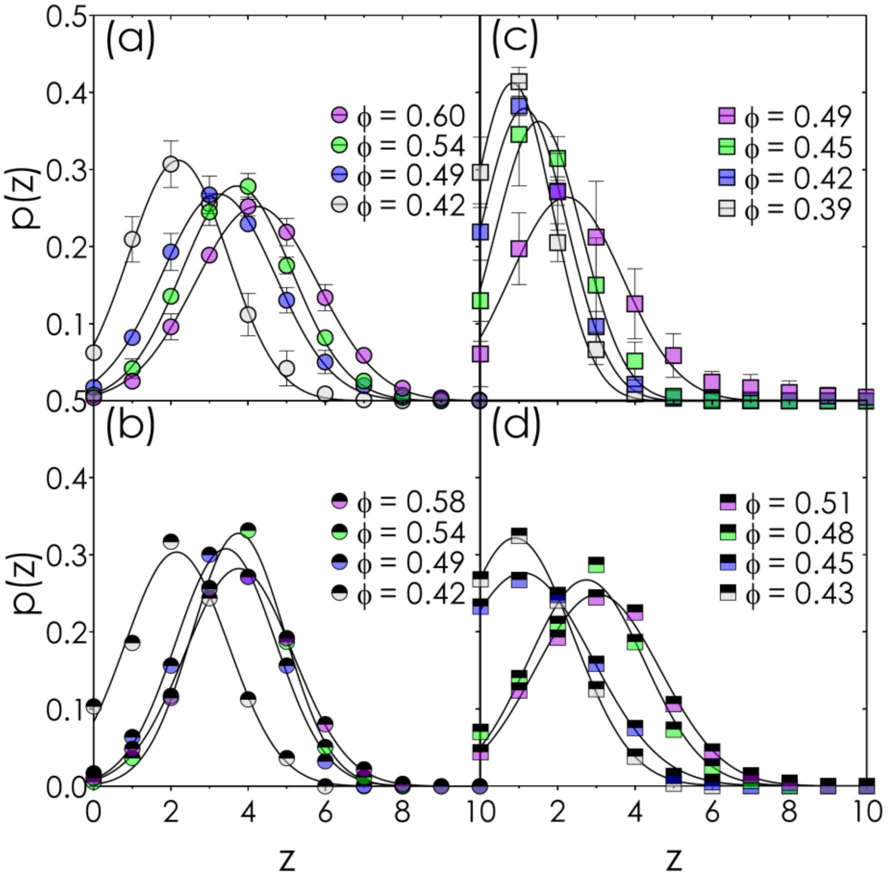

Figure A.5 | The dynamic contact number distribution (at shear thickening state, $\tilde{\sigma}_{\beta} \approx 10^4$, for suspensions of (a, b) smooth and (c, d) rough colloids in (a, c) experiments and (b, d) simulations.

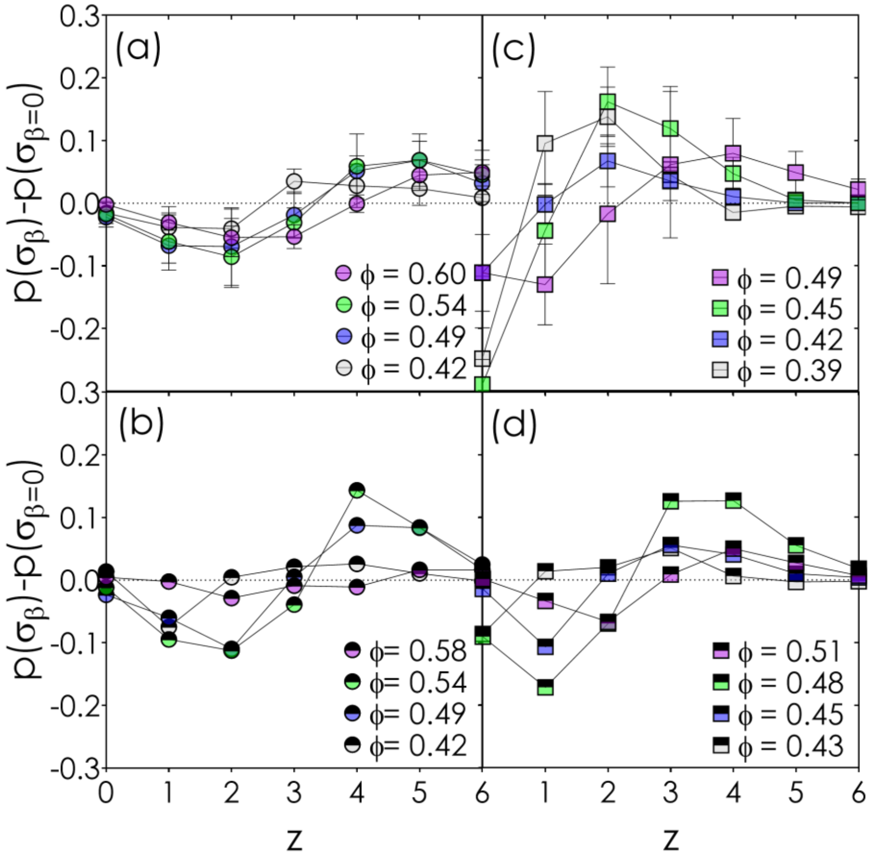

Figure A.6 | The change in stress-dependent contact distribution for suspensions of (a, b) smooth and (c, d) rough colloids in (a, c) experiments and (b, d) simulations.

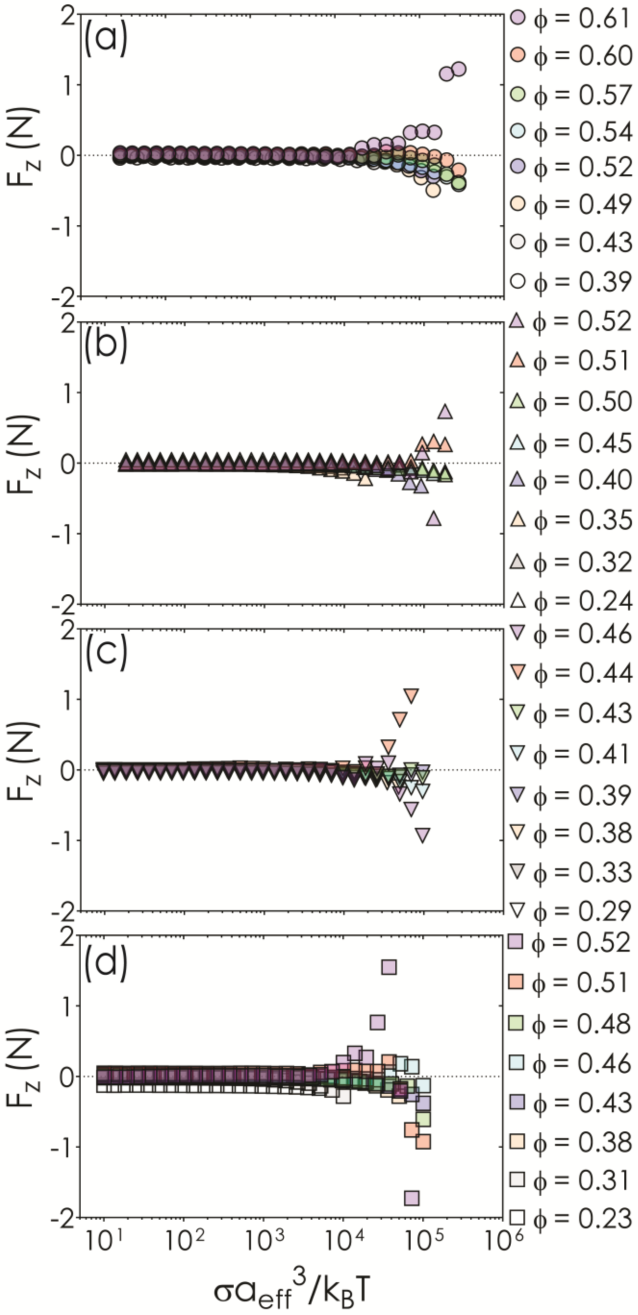

Figure A.7 | Axial force measurements for all colloidal suspensions tested in this study: (a) S, (b) SR, (c) VR, and (d) RK as a function of shear stress and ϕ.

References:

[1] M. Wyart and M. E. Cates, Physical Review Letters **112**, 098302 (2014).

[2] B. M. Guy, J. A. Richards, D. J. M. Hodgson, E. Blanco, and W. C. K. Poon, Physical Review Letters **121**, 128001 (2018).

[3] B. M. Guy, C. Ness, M. Hermes, L. J. Sawiak, J. Sun, and W. C. K. Poon, Soft Matter **16**, 229 (2020).

[4] A. Singh, C. Ness, R. Seto, J. J. de Pablo, and H. M. Jaeger, Physical Review Letters **124**, 248005 (2020).

[5] J. A. Anderson, J. Glaser, and S. C. Glotzer, Computational Materials Science **173**, 109363 (2020).

[6] A. Boromand, S. Jamali, B. Grove, and J. M. Maia, Journal of Rheology **62**, 905 (2018).

[7] S. Jamali, A. Boromand, N. Wagner, and J. Maia, Journal of Rheology **59**, 1377 (2015).

[8] P. Español, Physical Review E **52**, 1734 (1995).

[9] R. D. Groot and P. B. Warren, The Journal of Chemical Physics **107**, 4423 (1997).

[10] D. A. Fedosov, W. Pan, B. Caswell, G. Gompper, and G. E. Karniadakis, Proceedings of the National Academy of Sciences **108**, 11772 (2011).

[11] R. Kubo, Reports on Progress in Physics **29**, 255 (1966).

[12] A. Boromand, S. Jamali, and J. M. Maia, Computer Physics Communications **196**, 149 (2015).

[13] J. R. Melrose and R. C. Ball, EPL (Europhysics Letters) **32**, 535 (1995).

[14] M. Wang, S. Jamali, and J. F. Brady, Journal of Rheology **64**, 379 (2020).

[15] S. Jamali and J. F. Brady, Physical Review Letters **123**, 138002 (2019).

[16] S. Pradeep and L. C. Hsiao, Soft Matter **16**, 4980 (2020).

[17] E. Brown and H. M. Jaeger, Reports on Progress in Physics **77**, 046602 (2014).